Università di Genova

Department of Earth, Environment and Life Sciences (DISTAV)

Ph.D. course in

SCIENCES AND TECHNOLOGY FOR THE EARTH AND ENVIRONMENT

(STAT)

Curriculum: EARTH SCIENCES

XXXIV course

Use of microseismic data to monitor significant sea wave heights in support of marine weather forecasting and coastal protection

Utilizzo dei dati microsismici per il monitoraggio dell'altezza significativa delle onde del mare a supporto delle previsioni meteo-marine e a tutela della costa

Candidate: *DR.SSA LAURA CUTRONEO*

Coordinators: *PROF. MARCO CAPELLO*

PROF. GABRIELE FERRETTI

Index

Other published papers during the *Ph.D.*

1. Consani S., Ianni M.C., **Cutroneo L.**, Dinelli E., Carbone C., Capello M. (2019). Environmental implications of metal mobility in marine sediments receiving input from a torrent affected by mine discharge. Marine Pollution Bulletin 139: 221–230. https://doi.org/10.1016/j.marpolbul.2018.12.050
2. Reboa A., Mandich A., **Cutroneo L.**, Carbone C., Malatesta A., Capello M. (2019). Baseline evaluation of metal contamination in teleost fishes of the Gulf of Tigullio (north-western Italy): Histopathology and chemical analysis. Marine Pollution Bulletin 141: 16–23. https://doi.org/10.1016/j.marpolbul.2019.02.024
3. Cecchi G., Vagge G., **Cutroneo L.**, Greco G., Di Piazza S., Faga M., Zotti M., Capello M. (2019). Fungi as potential tool for polluted port sediment remediation. Environmental Science and Pollution Research 26: 35602-35609. https://doi.org/10.1007/s11356-019-04844-5
4. Greco G., Di Piazza S., Cecchi G., **Cutroneo L.**, Capello M., Zotti M. (2019). Mycoremediation of oily slime containing a polycyclic aromatic hydrocarbon mixture. Waste and Biomass Valorization 10: 3821-3831. https://doi.org/10.1007/s12649-019-00802-x
5. Cecchi G., **Cutroneo L.**, Di Piazza S., Vagge G., Capello M., Zotti M. (2019). From waste to resource: mycoremediation of contaminated marine sediments in the SEDITERRA Project. Journal of Soils and Sediments 20: 2653-2663. https://doi.org/10.1007/s11368-019-02527-9
6. Putzu S., Enrile F., Besio G., Cucco A., **Cutroneo L.**, Capello M., Stocchino A. (2019). A Reasoned Comparison between Two Hydrodynamic Models: Delft3D-Flow and ROMS (Regional Oceanic Modelling System). Journal of Marine Science and Engineering 7: 464. https://doi.org/10.3390/jmse7120464
7. **Cutroneo L.**, Reboa A., Besio G., Borgogno F., Canesi L., Canuto S., Dara M., Enrile F., Forioso I., Greco G., Lenolbe V., Malatesta A., Mounier S., Petrillo M., Rovetta R., Stocchino A., Tesan J., Vagge G., Capello M. (2020). Correction to: Microplastics in seawater: sampling strategies, laboratory methodologies, and identification techniques applied to port environment. Environmental Science and Pollution Research 27(16): 20571. https://doi.org/10.1007/s11356-020-08704-5
8. **Cutroneo L.**, Cincinelli A., Chelazzi D., Fortunati A., Reboa A., Spadoni S., Vena E., Capello M. (2020). Baseline characterisation of microlitter in the sediment of torrents and the sea bottom in the Gulf of Tigullio (NW Italy). Regional Studies in Marine Science 35: 101-119. https://doi.org/10.1016/j.rsma.2020.101119
9. Consani S., **Cutroneo L.**, Carbone C., Capello. M. (2020). Baseline of distribution and origin of Rare Earth Elements in marine sediment of the coastal area of the Eastern Gulf of Tigullio (Ligurian Sea, North-West Italy). Marine Pollution Bulletin 155: 111145. https://doi.org/10.1016/j.marpolbul.2020.111145
10. **Cutroneo L.**, Carbone C., Consani S., Capello M. (2020). Sediment distribution on the continental shelf in relation to stream inputs and contamination: hydrodynamic, chemical, mineralogical, and sedimentological characteristics (Ligurian Sea, Italy). Environmental Science and Pollution Research 27: 43755–43768. https://doi.org/10.1007/s11356-020-10259-4
11. Greco G., **Cutroneo L.**, Di Piazza S., Capello M., Zotti M. (2020). Trapping of marine-derived fungi on wooden baits to select species potentially usable in mycoremediation. Italian Journal of Mycology 49: 101-115. https://doi.org/10.6092/issn.2531-7342/10769
12. De Leo A., **Cutroneo L.**, Sous D., Stocchino A., (2021). Settling velocity of microplastics exposed to wave action. Journal of Marine Science and Engineering 9: 142. https://doi.org/10.3390/jmse9020142
13. Aguglia A., Giacomini G., Montagna E., Amerio A., Escelsior A., Capello M., **Cutroneo L.**, Ferretti G., Scafidi D., Costanza A., Serafini G., Amore M. (2021). Meteorological variables and suicidal behavior: air pollution and apparent temperature are associated with high-lethality suicide attempts and

male gender. Frontiers in Psychiatry 12: 653390. https://doi.org/10.3389/fpsyt.2021.653390

14. Cecchi G., **Cutroneo L.**, Di Piazza S., Capello M., Zotti M. (2021). Culturable marine fungi from six different Port sediments involved in the SEDITERRA Project. Journal of Soils and Sediments 21: 1563–1573. https://doi.org/10.1007/s11368-021-02884-4
15. Giacomini G., Aguglia A., Amerio A., Escelsior A., Capello M., **Cutroneo L.**, Ferretti G., Scafidi D., Serafini G., Amore M. (2021). The Need for Collective Awareness of Attempted Suicide Rates in a Warming Climate. The Case of the City of Genoa, Italy. Crisis https://doi.org/10.1027/0227-5910/a000763
16. **Cutroneo L.**, Reboa A., Geneselli I., Capello M. (2021). Baseline Considerations on salts used for density separation in the extraction of microplastics from sediments. Marine Pollution Bulletin 166: 112216. https://doi.org/10.1016/j.marpolbul.2021.112216
17. **Cutroneo L.**, Ferretti G., Barani S., Scafidi D., De Leo F., Besio G., Capello M. (2021). Near Real-Time Monitoring of Significant Sea Wave Height through Microseism Recordings: Analysis of an Exceptional Sea Storm Event. Journal of Marine Science and Engineering 9: 319. https://doi.org/10.3390/jmse9030319
18. Tesán Onrubia J.A., Djaoudi K., Borgogno F., Canuto S., Angeletti B., Besio G., Capello M., **Cutroneo L.**, Stocchino A., Mounier S., Lenoble V. (2021). Quantification of microplastics in North-Western Mediterranean harbors: seasonality and biofilm-related metallic contaminants. Journal of Marine Science and Engineering 9: 337. https://doi.org/10.3390/jmse9030337
19. Cecchi G., **Cutroneo L.**, Di Piazza S., Besio G., Capello M., Zotti M. (2021). Port Sediments: Problem or Resource? A Review Concerning the Treatment and Decontamination. Microorganisms 9(6): 1279. https://doi.org/10.3390/microorganisms9061279
20. Consani S., **Cutroneo L.** (2021). Baseline on Rare Earth Elements in the marine sediments of a Mediterranean commercial port as environmental tracers and their relationships with inorganic contaminants. Marine Pollution Bulletin 173: 112961. https://doi.org/10.1016/j.marpolbul.2021.112961

Summary

The focus of the *Ph.D.* project was the implementation of a network for monitoring significant sea wave heights (H_s) along the Ligurian coasts (north-western Mediterranean Sea), in order to provide near-real time data to weather forecasters and sea users (vessel captains, pilots, Coast Guard, Port Authorities and yachtsmen). The project was divided into a part dedicated to the use of microseismic data, interfaced with data derived from modelling hindcasts and from the wave buoy of Capo Mele, for the determination of H_s, and a part dedicated to the Interreg Italy-France Maritime 2014-2020 SINAPSI "Assistance to navigation for safe access to ports" Project, which involves the installation of instruments for measuring weather and sea parameters along the coasts of the Ligurian Sea.

The first phase of the *Ph.D.* project involved the study and updating of a mathematical procedure for the estimation of H_s from the microseismic data recorded by the network of seismic stations along the Ligurian arch. The procedure exploited the existing relationship between sea wave heights and microseismic signal and included the use of hindcast data to calibration steps and data from the Capo Mele wave buoy to verify the reliability of the estimated H_s data. In October 2018, an extreme sea storm hit the Ligurian coast with waves characterised by H_s greater than 6 m; these wave heights were not matched by an equivalent energy in the microseismic signal, which therefore led to an underestimation of the H_s estimated by the procedure. It was therefore necessary to investigate the extreme event of 2018, which led to the evidence of a lack in the energy of the microseismic signal and the need for a data compensation, which was possible thanks to the use of weather data (wind speed and atmospheric pressure) that were included in an additional element to the estimation procedure. The second phase of the *Ph.D.* project therefore involved verifying the reliability of the data estimated by the procedure, which led to the evidence of a generic underestimation of H_s. This led to the study of a first modification of the procedure and to the consequent monitoring of its validity on a large time scale. The monitoring of the reliability of the estimated data will be continued after the end of the *Ph.D.*, as well as the updating/refinement of the procedure.

The *Ph.D.* project involved the participation in the SINAPSI Project, which started in April 2019, in all its components, from the management to the implementation of the monitoring network, also including the communication and dissemination of the project activities to the stakeholders.

The *Ph.D.* has achieved the improvement of the H_s estimation procedure. The research activities will continue beyond the *Ph.D.* natural end to implement the results with data from a radar antenna system that will be installed in the Genoa area in the framework of the SINAPSI Project.

Keywords: microseism; significant sea wave height; coastal protection; extreme events; real-time monitoring; SINAPSI project.

Riassunto

Il progetto di Dottorato è stato principalmente focalizzato sull'implementazione di una rete di monitoraggio dell'altezza significativa dell'onda marina (H_s) lungo le coste del Mar Ligure (Mar Mediterraneo nord-occidentale), per la fornitura di dati in tempo quasi-reale ai meteo-previsori e a tutti gli utilizzatori del mare (Comandanti, Piloti, Capitanerie, Autorità Portuali e diportisti). Il progetto si è suddiviso in una parte dedicata all'utilizzo dei dati microsismici, interfacciati a dati derivati da *hindcast* modellistici e dalla boa ondametrica di Capo Mele, per la determinazione dell'H_s, e in una parte dedicata al progetto Interreg Italia-Francia Marittimo 2014-2020 SINAPSI "asSIstenza alla Navigazione per l'Accesso ai Porti in SIcurezza" che prevede l'installazione di strumenti di misura dei parametri meteo-marini lungo le coste del Mar Ligure.

La prima fase del Dottorato ha previsto lo studio e l'aggiornamento di una procedura matematica di stima dell'H_s a partire dai dati microsismici registrati dalla rete di stazioni sismiche presenti lungo l'arco ligure. La procedura ha sfruttato la relazione esistente tra altezza dell'onda marina e segnale microsismico, e ha previsto l'utilizzo dei dati degli *hindcast* modellistici per la calibrazione, e i dati della boa ondametrica di Capo Mele per la verifica dell'attendibilità del dato fornito. A ottobre 2018 una mareggiata di carattere estremo ha colpito le coste liguri con onde caratterizzate da H_s superiore a 6 m; a queste altezze d'onda non è corrisposta una equivalente energia nel segnale microsismico, che quindi ha portato ad una sottostima dell'H_s stimato dalla procedura. È stato quindi necessario un approfondimento relativo all'evento estremo del 2018, che ha portato all'evidenza di una mancanza dal punto di vista dell'energia del microsisma e al bisogno di una compensazione del dato che è stato possibile grazie all'utilizzo di dati meteorologici (velocità del vento e pressione atmosferica) che sono stati inseriti in un elemento aggiuntivo alla procedura. La seconda fase del Dottorato ha previsto quindi la verifica dell'attendibilità del dato fornito dalla procedura che ha portato all'evidenza di una generica sottostima di H_s. Questo ha comportato lo studio di una prima modifica della procedura e al conseguente monitoraggio su ampia scala temporale della sua validità. Il monitoraggio dell'attendibilità del dato fornito sarà portato avanti anche dopo il termine del Dottorato, così come l'aggiornamento/miglioramento della procedura.

Il progetto di Dottorato ha previsto la partecipazione al progetto SINAPSI, iniziato ad aprile 2019, in tutte le sue componenti, dalla gestione all'attuazione della rete di monitoraggio, comprendendo anche l'attività di comunicazione e divulgazione delle attività di progetto agli stakeholders.

Il Dottorato ha raggiunto un miglioramento dell'affidabilità della procedura di monitoraggio dell'H_s. Le attività di ricerca continueranno oltre il termine naturale del Dottorato per implementare i risultati con i dati dei radar costieri che verranno installati nell'ambito del Progetto SINAPSI nell'area di Genova.

Parole chiave: microsismi; altezza significativa dell'onda marina; protezione della costa; eventi estremi; monitoraggio in real-time; Progetto SINAPSI.

1 Aim of *Ph.D.* thesis

The project envisages the monitoring and forecasting of the sea wave height in the Ligurian Sea (north-western Mediterranean Sea) for coastal defence and navigation safety. The general objective of the project is to set up a near real-time monitoring network of the sea state (significant sea wave height) through the analysis, integration and interpolation of data deriving from different measurement systems: microseismic data detected by the seismographic network present on the Alpine and Apennine arch of the Ligurian Region (network operated by the Department of Earth, Environment and Life Sciences - DISTAV of the University of Genoa, Italy); significant sea wave height data over a long period (hindcast) deriving from the application of wave models forced by weather conditions to the Ligurian basin (hindcast generated by model application by the Department of Civil, Chemical and Environmental Engineering - DICCA of the University of Genoa, Italy). These systems were progressively interfaced with each other in order to progressively test and validate the reliability of the significant sea wave height data obtained by the estimation procedure. The data reliability was verified thanks to the comparison with data recorded by the wave buoys present in the Ligurian basin, until the final overall network is reached. The aim of this network is to provide stakeholders (sea users such as vessel captains and yachtsmen) and weather forecasters with accurate and widely distributed data on significant sea wave heights in the Ligurian Sea, with particular attention to the area off the Port of Genoa.

2 Thesis outlines

The *Ph.D.* thesis was carried out in the framework of the collaboration between the research groups of the Physical Oceanography and Seismology of the DISTAV and the research group of Coastal Engineering (MeteOcean) of the DICCA of the University of Genoa. The *Ph.D.* thesis was also developed in synergy with the Italy-France Interreg Maritime 2014-2020 SINAPSI “Assistance to navigation for safe access to ports” Project. The SINAPSI project started in April 2019 and will end in October 2022 and aims to deploy instruments and systems to monitor marine conditions (currents and waves) in ports and in sea areas facing them, along the coastline between Toulon (France) and Piombino (Italy) in the Ligurian Sea.

The topic under research is presented with the current limitations on wave monitoring and predictions arising from the most common methods used and the advantages resulting from the use of microseismic networks for monitoring sea wave heights. (Chapter 3)

The study area is the Ligurian Sea and an overview of the wave characteristics of the Ligurian basin is presented. (Chapter 4)

The *Ph.D.* project concept was to consider the relationship between microseisms and sea waves and the possibility of using the microseismic signal to determine the significant height of the sea wave. (Chapter 5)

The starting point of the *Ph.D.* thesis was the mathematical procedure created by Ferretti et al. (2018) for the transformation of the microseismic signal, recorded by seismographs along the Ligurian arch, into data of the significant sea wave height. This study involved the correlation of the microseismic signal with the significant wave height data coming from the engineering hindcast and the verification of the reliability of the data obtained thanks to the comparison with the data measured by the wave buoy at Capo Mele (Imperia, western Ligurian Sea). (Chapter 6)

On the occasion of the strong storm (Adrian Storm) that hit Liguria on 29 October 2018, despite the extreme characteristics of the sea storm (maximum wave height 9.6 m and peak period 11.7 s measured by the Capo Mele buoy) which was defined by the weather-predictors as an "oceanic storm" and which caused numerous and extensive damages to coastal infrastructures, the microseisms associated with the sea waves did not show

equivalent energy, and consequently the estimation model significantly underestimated the sea wave height. Therefore, the *Ph.D.* project focused on the Adrian Storm, considering both the weather and sea characteristics that generated it and that made it extreme for the Ligurian climate. The characteristics of this storm were then compared to those of other recent strong sea storm that have affected the Ligurian coast, to understand which weather parameter was the most influential and which could be included in the estimation model to avoid possible future underestimates of sea wave height in cases of extreme sea storms. (Chapter 7)

Given the significant underestimation of the sea wave height due to the lack of energy peak in the microseism occurred during the Adrian Storm, the reliability of data obtained from the mathematical procedure defined in Ferretti et al. (2018) was monitored over a long period to highlight any other significant differences between the measured and estimated sea wave height or criticalities in the reliability of the model. A monitoring procedure was defined and a first amendment to the mathematical procedure has been proposed. (Chapter 8)

The need for real-time data on currents and waves has also been addressed by the European SINAPSI Project, which involved different partners for the installation of instruments and measurement systems at various sites along the coast of the Ligurian Sea. The *Ph.D.* project followed the SINAPSI Project from the first writing phases until the 30th month of activities, with the management of the project, the exchanges with the different partners, the necessary studies for the choice of the best instruments and the best installation positions in the different port of the project, and the dissemination activities. Future developments of the SINAPSI Project include the installation of a radar antenna system to monitor the sea state in the central part of the Ligurian Sea. The data that will be recorded by the radar system will also be used to implement the sea wave height estimation procedure with microseism data in future research development. (Chapter 9)

3 Introduction

Monitoring of the sea has become increasingly fundamental to improve knowledge of physical, geological, biological and chemical processes in the marine environment, also from the point of view of climate change. In particular, the study of wave characteristics (period, wavelength and significant height) is essential for the design and conservation of coastal and offshore infrastructures. Monitoring and even predicting the height of sea waves is therefore crucial for maritime economic activities such as transport and marine risk assessment (Cousins et al., 2014; Von Storch et al., 2015). The prediction of sea waves is also of considerable importance for the safety of navigation (Niclasen et al., 2010). Since wave characteristics depend on weather conditions, and, in especially on wind direction and velocity, and since without knowing the initial weather condition it is not possible to predict future wave development, experimental data are fundamental for the initialisation of numerical forecasting models and become particularly important near the coast, where the relationship between wind and waves is influenced by the local conformation of the seabed and coast and the presence of infrastructures. Therefore, experimental data are essential in wave forecasting in basins such as the Mediterranean Sea, where specific problems are encountered due to the complexity of the orography, which in turn implies strong local weather characteristics, and the complex bathymetry and limited extent of the fetch.

It is therefore necessary to analyse long-term time series for climatological studies and to find real-time data to achieve high levels of forecasting accuracy (Novak, 2015). In order to obtain long time series, observation networks consisting of different interconnected systems become essential to cover as large an area as possible. For weather forecasting worldwide, the Global Observing System (GOS) is composed by a multitude of individual surface- and space-based observing systems owned and operated by a plethora of national and international agencies with different funding lines, allegiances, overall priorities and management processes (https://public.wmo.int/en/programmes/global-observing-system). The GOS is constituted by different technologies, such as remote sensing, weather stations, RADAR, LIDAR, radiosondes, radiometers, ocean

data buoys and diffuse observational networks (Fig. 3.1). At the oceanographic level, the main global network for oceanographic observations is the Global Ocean Observing System (GOOS; https://www.goosocean.org/) focused on building a system to support climate science and be the observational backbone for operational forecast systems.

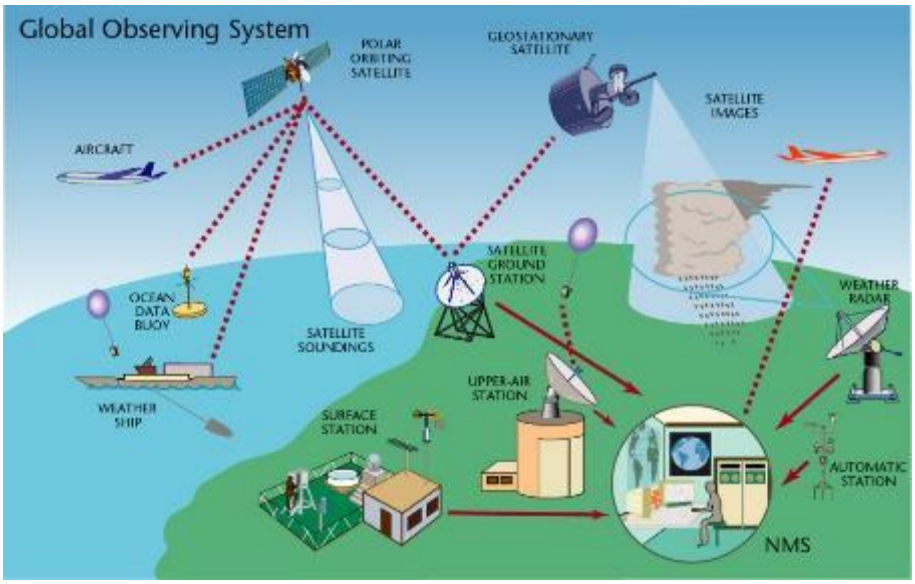

Fig. 3.1. The modern observing network (Global Observing System, GOS) for collecting data for weather forecasts (www.wmo.int).

In the case of wave prediction, however, the possibility of acquiring real time data and over sufficiently large areas is generally reduced and relies mainly on remote sensing, by satellite-based instruments, such as altimeters. However, many satellite data are not always available near the coast and under an overcast sky, as is typically the case during extreme precipitation (Pensieri et al., 2018). Data deriving from other monitoring system, such wave buoy, are generally used to independently check the quality of modelled wave parameters. This is because buoys and similar systems provide wave data at single point or limited area and do not guarantee a constant supply of data. Wave buoys are floating devices anchored to the seabed, moving with the sea waves, and measuring this movement through sensors such as accelerometers and tilt sensors (Zhu et al., 2016). Their low use is because their installation, maintenance and management at sea are historically difficult. In addition, the continuous acquisition of buoy data is often subjected to problems in the radio transmission of the signal between the buoy and the shore station, and also to system malfunctions in general (e.g., buoy unmooring, breakdown of radio transmission/reception equipment, breakdown of storage media, breakdown/malfunctioning of power systems, scheduled maintenance operations, etc.) that generate data loss and fragmentation of the dataset (Fig. 3.2; O'Connor et al., 2013; Samiksha et al., 2015). Data disruption has a negative effect not only on programs that require real-time information [such as Physical Oceanography Real Time System ("PORTS") of the National Oceanic and Atmospheric Administration's (NOAA), that provides data including sea wave height, for navigation], but also on the statistical analysis of the data and thus, for example, the estimation of average sea wave height and extreme conditions needed for sediment transport studies, structure design and other applications (Londhe and Panchang, 2007). Finally, the wave buoy provides punctual data of wave characteristics (Eulerian measurements), which are therefore representative of a relatively small area, and this constitutes a limitation especially in sea basins characterised by a complex morphology, as in the case of the Ligurian Sea.

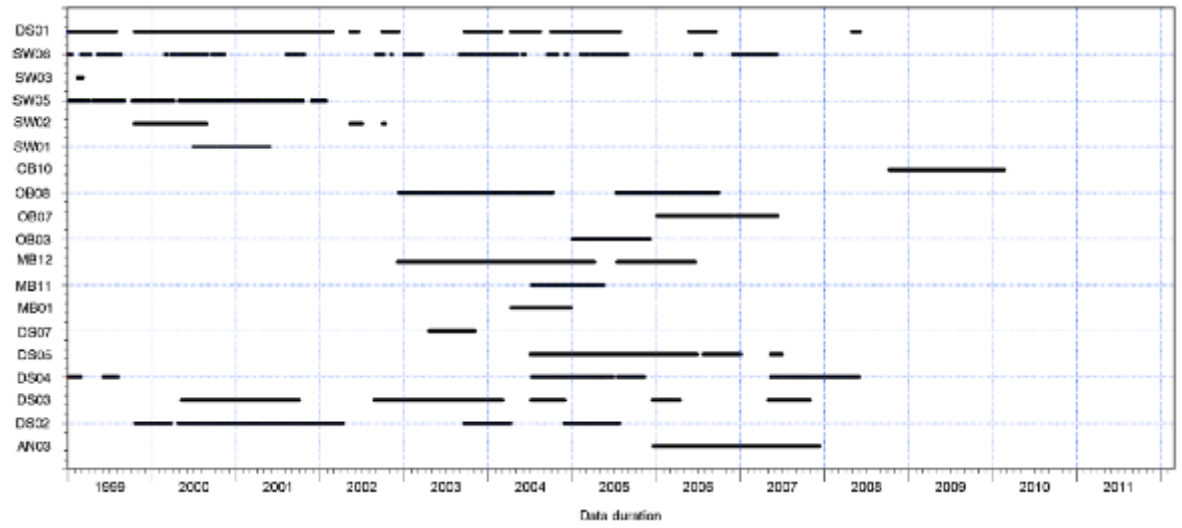

Fig. 3.2. Example of fragmentation in the coverage of data recorded by wave buoys (India; Samiksha et al., 2015).

In the last decades, in order to compensate for the lack of data from wave buoys, alternative methods for the assessment of sea wave parameters have been proposed, such as those based on numerical modelling (Mentaschi et al., 2013, 2015; Niclasen et al., 2010), microseism analysis (Ardhuin et al., 2012; Bromirski et al., 2005), and High Frequency (HF) radar systems. The former aim to determine wave parameters through numerical modelling of sea wave propagation forced by atmospheric conditions, microseism analysis consist in relating sea wave characteristics to microseismic energy, and radar systems measure wave parameters exploiting the emission of a signal and its reflection by the marine surface. The advantages of using these alternative monitoring systems lie in the fact that they are either mathematical (in the case of models) or based on structures installed on land (as in the case of seismic networks or radar systems) and therefore do not suffer from the difficulties generated by being at sea. In the case of seismic networks, the further advantage lies in the fact that these networks are generally already existing and widespread on the territory and, therefore, exploiting them also for monitoring sea waves would also allow economic savings in addition to having a wide territorial coverage. However, buoy measurements remain of fundamental importance for assessing the reliability and accuracy of the results obtained from the application of hindcasts (databases derived from statistical calculations that determine the likely past conditions, such as sea wave characteristics, at a given location and time), microseisms and HF radar systems.

Over the last twenty years, wave simulation models have become indispensable tools for sea state predictions in both scientific and engineering fields. Among the various spectral wave models available, the WAM (WAve prediction Model) is the most widely used; another popular model for wave simulation is the SWAN (Simulating WAves Nearshore). SWAN is a latest-generation model that describes the evolution of the energy density spectrum under arbitrary wind, current and bathymetry conditions. Its physical implementation and numerical calculation algorithms have been developed and designed precisely to overcome the traditional difficulties encountered in applying a wave model in shallow coastal areas (Booij et al., 1999; Bargagli et al., 2011). The continuous efforts made in recent years to improve the different aspects of wave simulations in closed basins or marginal seas, such as the Mediterranean Sea, have resulted in a better representation of local wave dynamics. In particular, Ardhuin et al. (2010) have achieved significant progress in this direction through the introduction of new source terms (parameters characterising the source) for wave growth and dissipation. Originally, these source terms were developed to reproduce in the WAVEWATCH III® (WWIII) model the growth and dissipation description of the wave already present in the WAM model. An innovative contribution by Ardhuin et al. (2010) consists of a new term to describe the dissipation of the long sea (swell) as a function

of wind friction speed. Comparisons between the model results and observations from satellites and buoys indicated a significant improvement in the simulations on a global scale. Mentaschi et al. (2015) evaluated the performance of the WWIII numerical model in the Mediterranean Sea, constrained by the Weather and Research Forecasting (WRF) atmospheric model, generating a hindcast dataset over a period between 1979 and 2017.

Microseisms include all ground movements detectable with seismographs and due to various causes with different characteristics depending on their origin. Depending on the origin, the nature of the associated elastic waves varies. There are microseisms due to wind, traffic, mechanical actions on the ground (as for example in industrial areas), sea waves, sea waves breaking on rocky coasts, rain and generally large weather disturbances (Giorgi and Rosini, 1950). Microseisms due to wave motion are characterised by periods between about 2 and 40 seconds and, in general, it is possible to distinguish them into two different types: the primary microseism is directly generated by the variation of pressure induced by the waves on the seabed (with shallow water) and has the same period (8-20 s) and the same frequency (0.05-0.1 Hz) of the sea waves that generate it; the secondary microseism, instead, is characterised by a frequency that is about twice that of the sea wave (0.1-0.5 Hz) and a period that is half that of the sea waves (3-10 s), and is generated by the fluctuation of the pressure on the seabed caused by the interaction of two waves of the same wavelength that move in opposite directions (Davy et al, 2014). Within the complex of secondary microseisms, it is possible to distinguish between long-period microseisms (frequency 0.085-0.2 Hz) produced by distant sources (e.g., ocean swells) and short-period microseisms (frequency 0.2-0.5 Hz) generated by near-shore sources (e.g., local wind waves) (Bromirski et al. 2005). The main component of secondary microseisms is the Rayleigh surface elastic waves, which travel within the surface of the seabed and whose low attenuation allows the microseism to travel long distances (Roux et al., 2005), thus allowing the recording of events produced over long distances such as ocean storms. In 1999, Bromirski et al. presented a study based on the correlation between the measurements made by a wave buoy and those of a seismograph along the California coast; in this study, the Authors demonstrated that elements of the sea wave climate can be accurately reconstructed using data from the seismograph present in the coastal hinterland. Indeed, the details of the seismic wave spectrum contain the details that characterise the sea waves that generate them; these, in turn, are derived from the characteristics of wind fields and coastal reflections (Ardhuin et al., 2011). It is therefore possible from the analysis of the seismic wave spectrum to trace the height of the sea wave. A positive aspect of exploiting seismic data is to take advantage of existing networks of seismic stations that are already present in the area, cover a wide part of the territory and provide fewer maintenance problems.

A further step forward in technologies applied to the real-time measurement of sea waves is the application of coastal radars, which have developed over the last twenty years and is now in full swing. The term "radar" originates as an acronym for “RAdio Detection And Ranging" and defines a device that transmits a radio-frequency signal (typically in the microwave range) towards a target that reflects the signal and produce an echo; the distance to the target can be calculated from the time it takes for the reflected signal to reach the antenna. In a coastal radar system, the target is represented by the sea waves propagating on the surface of the coastal basin. Short-wave HF coastal radars, positioned along the coast, emit radio signals (8-37 MHz) which are transmitted in the direction of the sea and reflected by the sea waves. The rippled surface of the sea thus acts as a large reflection-diffraction grating for electromagnetic waves. Since the waves are never stationary but travel radially as they approach and recede from the radar, the reflected signal returns at a different frequency from the transmitted one, and in particular, this frequency increases for approaching wave trains and decreases for receding ones. The analysis of the backscatter spectrum of these waves, thanks to the Doppler effect, makes it possible to obtain maps of the surface current and sea waves (Bué et al., 2020; Rubio et al., 2017). The application of coastal radar allows accurate and precise wave measurements with good resolution (from 250 m to 15 km depending on the specific application), continuously (typically one measurement every hour) and in real time, in any weather condition and covers sea areas extending kilometres (Mantovani et al.,

2020; Orasi et al., 2018). At the end of 2016, there were 400 coastal radars installed worldwide, while more than 50 radar systems were deployed in Europe (Mader et al., 2016). Currently, a good number of radar systems have been installed or are being planned and prepared, also along the Ligurian Sea coasts, thanks to European Projects such as SICOMAR (Marine control system), SICOMAR plus (Cross-border system for maritime safety against maritime hazards and protection of the marine environment) and IMPACT (Port impact on marine protected areas: cross-border cooperative actions).

3.1 References

Ardhuin F., Balanche E., Stutzmann E., Obrebski M. (2012). From seismic noise to ocean wave parameters: general methods and validation. Journal of Geophysical Research 117: C05002. https://doi.org/10.1029/2011JC007449

Ardhuin F., Rogers E., Babanin A.V., Filipot J., Magne R., Roland A., van der Westhuysen A., Queffeulou P., Lefevre J., Aouf L., Collard F. (2010). Semiempirical dissipation source functions for ocean waves. Part I: definition, calibration, and validation RID A-1364-2011. Journal of Physical Oceanography 40(9): 1917–1941.

Ardhuin F., Stutzmann E., Schimmel M., Mangeney A. (2011). Ocean wave sources of seismic noise. Journal of geophysical Research 116: C09004. https://doi.org/10.1029/2011JC006952

Bargagli A., Carillo A., Ruggiero V., Lanucara P., Sannino G. (2011). Ricerca di Sistema elettrico - Modello di onde per l'area mediterranea. Report RdS/2011/26, pp. 28. https://www.enea.it/it/Ricerca_sviluppo/documenti/ricerca-di-sistema-elettrico/correnti-marine/rds-26.pdf

Booij N., Ris R.C., Holthuijsen L.H. (1999). A third-generation wave model for coastal regions: 1. model description and validation. Journal of Geophysical Research 104: 7649–7666. https://doi.org/10.1029/98JC02622

Bromirski P.D., Duennebier F.K., Stephen R.A. (2005). Mid-ocean microseisms. Geochemistry Geophysics Geosystems 6(4): Q04009. https://doi.org/10.1029/2004GC000768

Bromirski P.D., Flick R.E., Graham N. (1999). Ocean wave height determined from inland seismometer data: Implications for investigating wave climate changes in the NE Pacific. Journal of Geophysical Research: Oceans 104(C9): 20753–20766. https://doi.org/10.1029/1999JC900156

Bué I., Semedo A., Catalao J. (2020). Evaluation of HF Radar wave measurements in Iberian Peninsula by comparison with satellite altimetry and in situ wave buoy observations. Remote sensing 12: 3623. https://doi.org/10.3390/rs12213623

Cousins W., Sapsis T.P. (2014). Quantification and prediction of extreme events in a one-dimensional nonlinear dispersive wave model. Physica D: Nonlinear Phenomena 280-2081: 48–58. https://doi.org/10.1016/j.physd.2014.04.012

Davy C., Barruol G., Fontaine F.R., Sigloch K., Stutzmann E. (2014). Tracking major storms from microseismic and hydroacoustic observations on the seafloor. Geophysical Research Letters 41: 8825–8831. https://doi.org/10.1002/2014GL062319

Giorgi M., Rosini E. (1950). Sulla natura delle cause che generano i microsismi. www.annalsofgeophysics.eu/index.php/annals/article/view/6023/5950

Londhe S.N., Panchang V. (2007). Correlation of wave data from buoy networks. Estuarine, Coastal and Shelf Science 74(3): 481–492. https://doi.org/10.1016/j.ecss.2007.05.003

Mader J., Rubio A., Asensio J.L., Novellino A., Alba M., Corgnati L., Mantovani C., Griffa A., Gorringe P., Fernandez V. (2016). The European HF Radar inventory. EuroGOOS Pubblications, pp. 23.

Mantovani C., Corgnati L., Horstmann J., Rubio A., Reyes E., Quentin C., Cosoli S., Asensio J.L., Mader J., Griffa A. (2020). Radar practices on High Frequency Radar deployment and operation for ocean current measurement. Frontiers in Marine Science 7: 210. doi: 10.3389/fmars.2020.00210

Mentaschi L., Besio G., Cassola F., Mazzino A. (2013). Developing and validating a forecast/hindcast system for the Mediterranean Sea. Journal of Coastal Research SI 65: 1551-1556. http:/dx.doi.org/102112/SI65-262.1

Mentaschi L., Besio G., Cassola F., Mazzino A. (2015). Performance evaluation of Wavewatch III in the Mediterranean Sea. Ocean Modelling 90: 82–94. https://doi.org/10.1016/j.ocemod.2015.04.003

Niclasen B.A., Simonsen K., Magnusson A.K. (2010). Wave forecasts and small-vessel safety: a review of operational warning parameters. Marine Structures 23: 1–21. https://doi.org/10.1016/j.marstruc.2010.02.001

Novak D.R. (2015). Weather forecasting - Operational Meteorology. Encyclopedia of Atmospheric Sciences (Second Edition), pp. 293–302.

Orasi A., Picone M., Drago A., Capodici F., Gauci A., Nardone G., Inghilesi R., Azzopardi J., Galea A., Ciraolo G., Sanchez musulin J., Alonso-Martirena A. (2018). HF radar for wind waves measurements in the Malta-Sicily Channel. Measurement 128: 446-454. https://doi.org/10.1016/j.measurement.2018.06.060

O'Connor M., Lewis T., Dalton G. (2013). Weather window analysis of Irish west coast wave data with relevance to operations and maintenance of marine renewables. Renewable Energy 52: 57-66. http://dx.doi.org/10.1016/j.renene.2012.10.021

Pensieri S., Schiano M.E., Picco P., Tizzi M., Bozzano R. (2018). Analysis of the precipitation regime over the Ligurian Sea. Water 10: 566. doi:10.3390/w10050566.

Roux P., Sabra K.G., Gerstoft P., Kuperman W., Fehler M.C. (2005). P-waves from cross-correlation of seismic noise. Geophysical Research Letters 32: L19303. https://doi.org/10.1029/2005GL023803

Rubio A., Mader J., Corgnati L., Mantovani C., Griffa A., Novellino A., Quentin C., Wyatt L., Schulz-Stellenfleth J., Horstmann J., Lorente P., Zambianchi E., Hartnett M., Fernandes C., Zervakis V., Gorringe P., Melet A., Puillat I. (2017). HF Radar Activity in European Coastal Seas: Next Steps toward a Pan-European HF Radar Network. Frontiers in Marine Science 4: 8. https://doi.org/10.3389/fmars.2017.00008

Samiksha S.V., Polnikov V.G., Vethamony P., Rashmi R., Pogarskii F., Sudheesh K. (2015). Verification of model wave heights with long-term moored buoy data: Application to wave field over the Indian Ocean. Ocean Engineering 104: 469–479.

Von Storch H., Emeis K., Meinke I., Kannen A., Matthias V., Ratter B.M.W., Stanev E., Weisse R., Wirtz K. (2015). Making coastal research useful - cases from practice. Oceanologia 57(1): 3–16. https://doi.org/10.1016/j.oceano.2014.09.001

Zhu N., Kim Y., Lim K.-H., Shin B.-S. (2016). Change detection of ocean wave characteristics. Expert Systems with Applications 51(1): 245–258. https://doi.org/10.1016/j.eswa.2015.12.017

4 Sea state characteristics of the Ligurian Sea

The Mediterranean Sea, due to its nature of semi-enclosed basin, shows a large variety of wave climate features. This variability is mainly governed by the highly diversified weather characteristics active on the different sub-basins (Sartini et al., 2017). In particular, complex mechanisms involving severe atmospheric-climatic forcing and local land configuration of the sub-basins forcing the air masses and favouring the formation of cyclogenesis systems make the Mediterranean Sea one of the most active regions of the Northern Hemisphere in terms of weather and wave seasonal variability (Orfila et al., 2005; Sartini et al. 2017; Trigo et al., 2002). In the north-western Mediterranean Sea, the Ligurian Sea, and especially the Gulf of Genoa, is a preferred site of cyclogenesis together with the Gulf of Lion. The presence of the mountains (the Alps) near the coast is a key factor in the climatic characteristics of the Ligurian Sea (Carniel et al., 2012; Lionello et al., 2006; Orfila et al., 2005) because they play a decisive role as boundaries for the atmospheric pressure and wind distribution over the basin. Cyclones are a constant feature over the whole year on the Ligurian Sea (Lionello et al., 2006) but they are generally deeper and more frequent in winter than during the other seasons (Trigo et al. 2002).

Cremonini et al. (2021), basing their study on a 37-year dataset of wind and wave hindcast covering the entire Ligurian Sea at 10-km resolution, described the characteristic wave climate that affect the Ligurian coast: in Fig. 4.1 it can be appreciated how the waves in front of Genoa propagate from three main directions, i.e. NNW, SWS and SSE. From the polar plot, it is possible to see also that the highest significant wave heights are from SWS and NNW. Sartini et al. (2017), analysing the same hindcast dataset of Cremonini et al. (2021), confirmed that the combination of the NW and SW wind regimes are responsible for the development of severe sea states in the Ligurian Sea (Fig. 4.2), where swell sea conditions are frequent. It must be pointed out that due to the conformation and the southern exposure of the Ligurian region, while strong winds and swells from the N only affect the open sea, sea storms from the southern quadrants also affect the coasts. From Fig. 4.2 it is possible to see how the maximum wave height characteristics are different between the eastern and western Liguria (exposed to the SW and SE quadrants, respectively), precisely because of the arched shape of the region.

Finally, Sartini et al. (2017) pointed out that the most energetic sea conditions occur mainly during the winter from December to March in the western Mediterranean basin, but that they are also constant and temporally

spread throughout the year, as suggested by the frequent and intense storm events documented in the Ligurian Sea in spring and autumn (Lionello et al., 2006).

In a recent and detailed study on the changes in wave climate, Amarouche et al. (2021) pointed out that an increase in the coastal storm intensity has occurred in recent decades and that the Mediterranean Sea is identifiable as a climate change hotspot for the coming decades. They elaborated a study on the last 41 years wave observation in the western Mediterranean Sea and highlighted that the outstanding storm observed in October 2018 (the Adrian Storm), which caused enormous damage to the Ligurian coasts, was a new record in the significant sea wave height in the Ligurian Sea (Fig. 4.3). Evidence such as that provided by Amarouche et al. (2021) further highlights how important the study of wave regime in a basin is and how important it is to have as much wave data as possible available to understand how the climate evolves and how to protect the coastline.

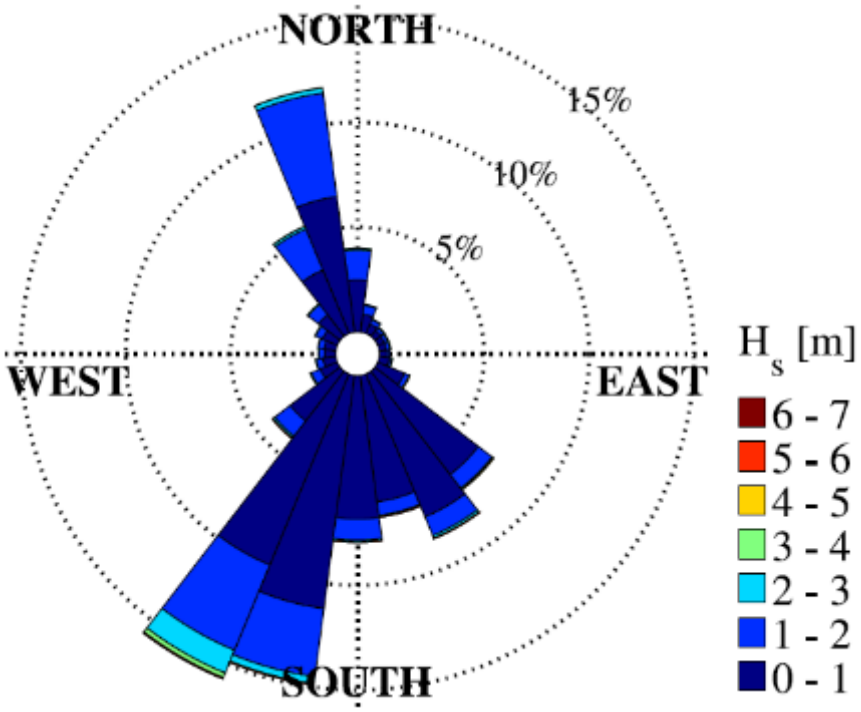

Fig. 4.1. Polar plot of the 1979–2018 time series of significant sea wave height (H_s) in the area of Genoa (Cremonini et al., 2021). It is recalled that wave direction is the incoming direction.

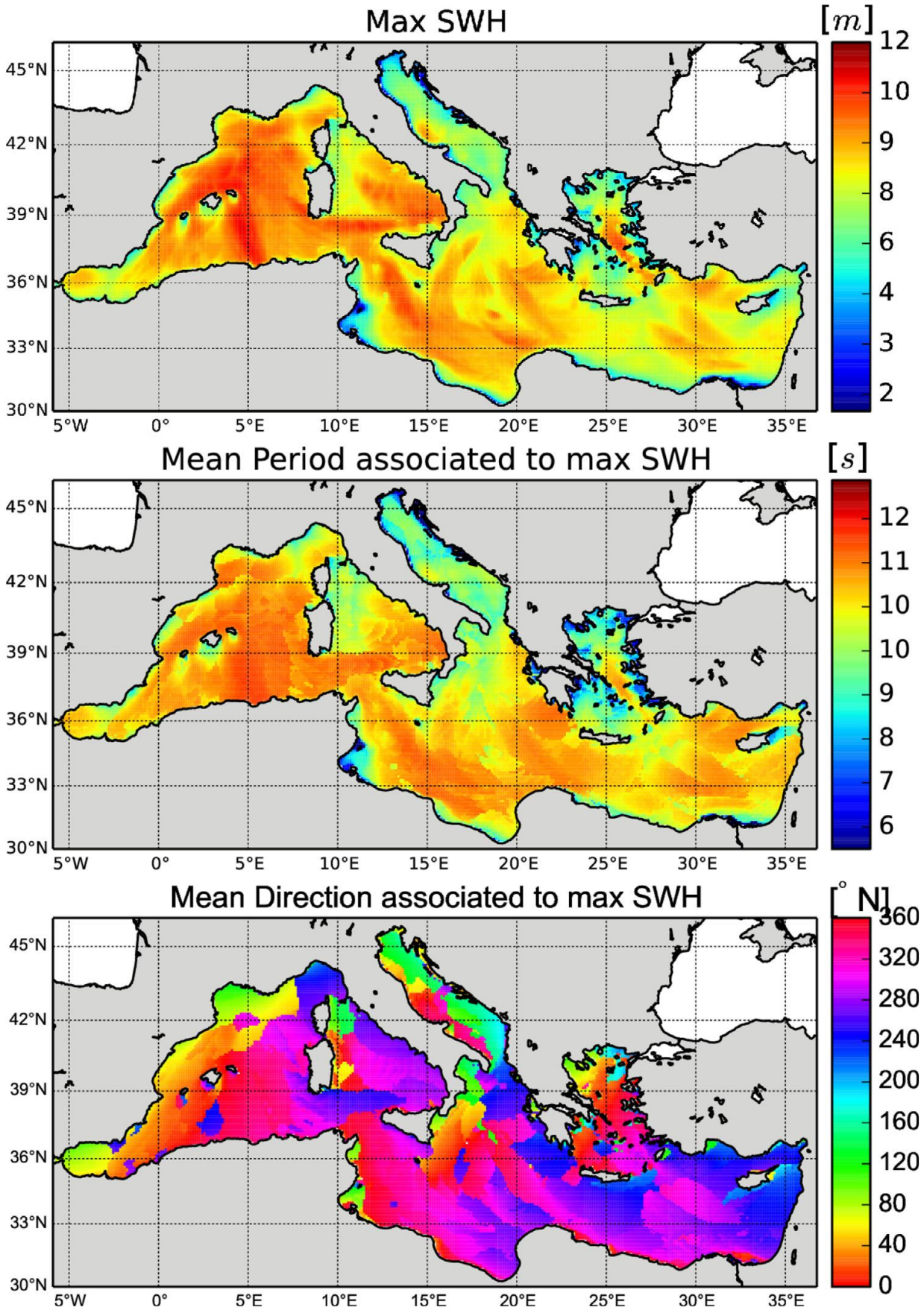

Fig. 4.2. Absolute maxima of significant wave heights (top) and corresponding mean period (centre) and mean direction (bottom) in the Mediterranean Sea (Sartini et al., 2017).

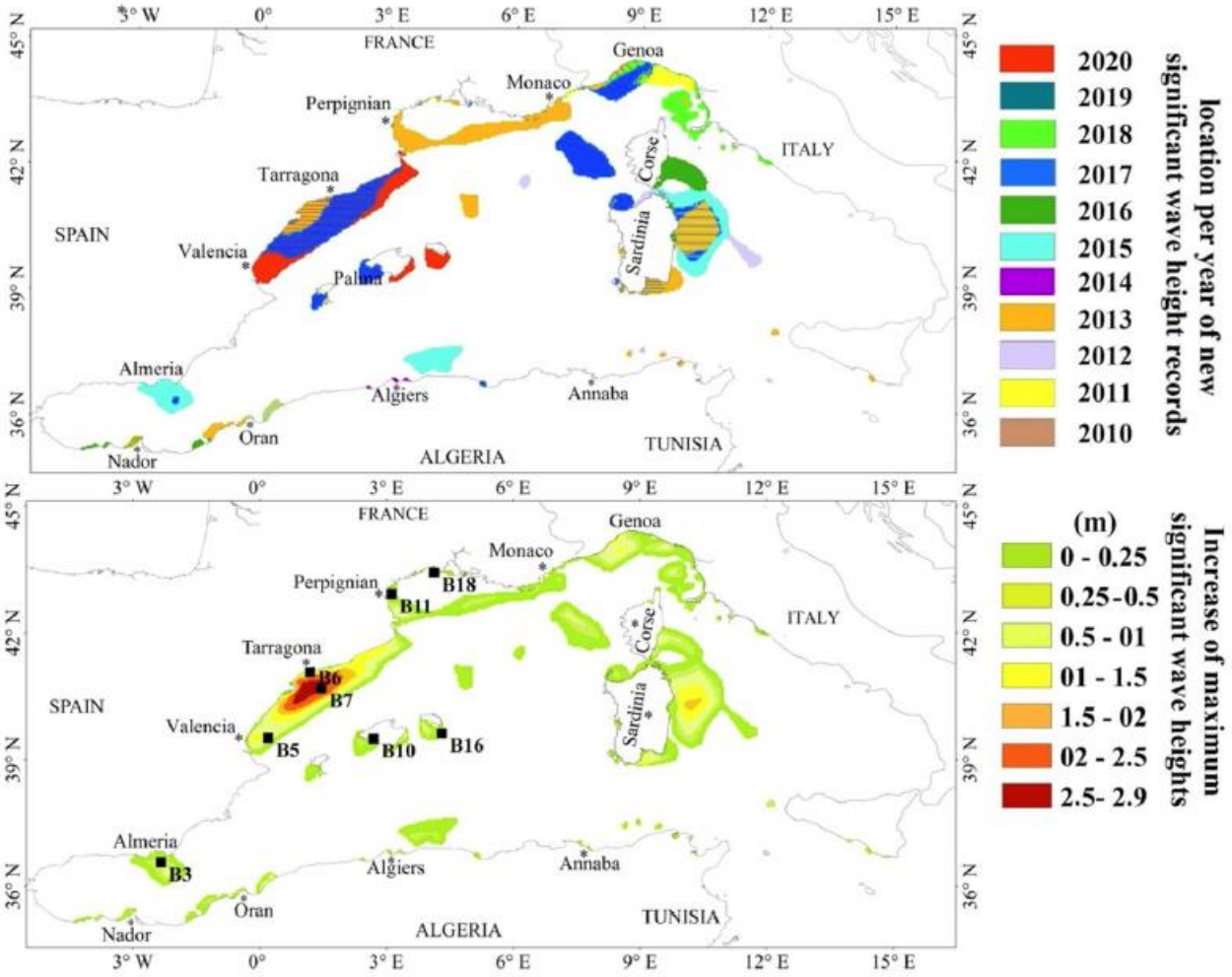

Fig. 4.3. Spatial distributions of the annual new records of significant wave height between January 2010 and 2020 (top) and the differences between the maximum significant wave height observed from 2010 to 2020 and those observed from 1979 to 2010 (bottom)(Amarouche et al., 2021).

4.1 References

Amarouche K., Bingolbali B., Akpinar A. (2021). New wind-wave climate records in the Western Mediterranean Sea. Climate Dynamics https://doi.org/10.1007/s00382-021-05997-1

Cremonini G., De Leo F., Stocchino A., Besio G. (2021). On the selection of time-varying scenarios of wind and ocean waves: Methodologies and applications in the North Tyrrhenian Sea. Ocean Modelling 163: 101819. https://doi.org/10.1016/j.ocemod.2021.101819

Lionello P., Bhend J., Buzzi A., Della-Marta P., Krichak S., Jansa A., Maheras P., Sanna A., Trigo I., Trigo R. (2006). Cyclones in the Mediterranean region: climatology and effects on the environment. Developments in earth and environmental sciences 4: 325-372. https://doi.org/10.1016/S1571-9197(06)80009-1

Orfila A., Alvarez A., Tintoré J., Jordi A., Basterretxea G. (2005). Climate teleconnections at monthly time scales in the Ligurian Sea inferred from satellite data. Progress in Oceranography 66: 157-170. doi: 10.1016/j.pocean.2004.07.011.

Sartini L., Besio G., Cassola F. (2017). Spatio-temporal modelling of extreme wave heights in the Mediterranean Sea. Ocean Modelling 117: 52-69. http://dx.doi.org/10.1016/j.ocemod.2017.07.001

Small R.J., Carniel S., Campbell T., Teixeira J., Allard R. (2012). The response of the Ligurian and Tyrrhenian Seas to a summer Mistral event: A coupled atmosphere-ocean approach. Ocean Modelling 48: 30-44. doi: 10.1016/j.ocemod.2012.02.003.

Trigo I.F., Bigg G.R., Davies T.D. (2002). Climatology of cyclogenesis mechanisms in the Mediterranean. American Meteorological Society 130: 549-569.

5 Microseisms for sea wave height estimation

The seismic noise recorded by a seismic station is the result of the temporal superposition of different signals from largely unrelated and spatially distributed sources. Noise-producing sources are all those that interact with the earth's crust or the ground in such a way as to generate elastic waves that propagate in every direction. Sources that can generate seismic noise are generally divided into natural (weather phenomena such as wind and ocean waves) and anthropogenic (cultural noise: vehicular traffic, use of industrial machinery, etc.; Fig. 5.1) and are characterised by different frequencies at which they develop: at frequency <1 Hz, sources are essentially natural (ocean, weather conditions on large-scale); at high frequencies (>5 Hz), sources are anthropogenic; and at intermediate frequencies (between 1 and 5 Hz) sources can be natural (local weather conditions) or anthropogenic (urban noise; Bonnefoy-Claudet et al., 2006). Vibrations at low frequencies (<1 Hz) are called “microseisms”, while those at high frequencies (>1 Hz) are called “microtremors”. Spectral analysis is the first and fundamental step in identifying the characteristics and content of the seismic noise signal (Marzorati, 2007).

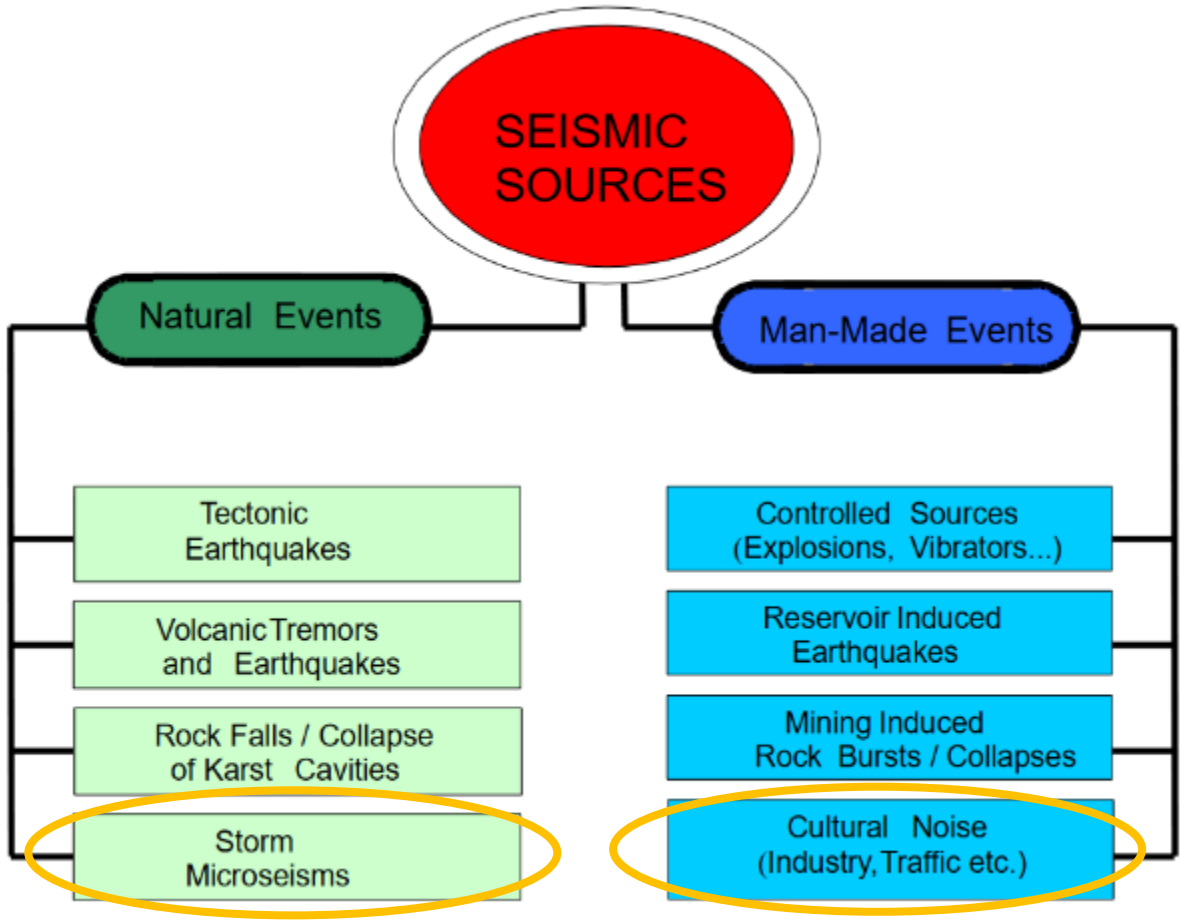

Fig. 5.1. Schematic classification of various kinds of events which generate seismic waves (from Bormann et al., 2009). In yellow, the seismic noise sources.

Already at the turn of the 1940s and early 1950s, Longuet-Higgins and Ursell (1948), Longuet-Higgins (1950) and Gutemberg (1951) claimed that the strongest peaks of the seismic noise are represented by microseisms and are generated by two mechanisms involving sea-bottom interaction. In fact, microseisms are originated by atmospheric energy in the form of storms over the oceans that coupled into the water column via the generation of ocean swell, is transmitted to the seafloor, and then travels as elastic waves at the seafloor (Ebeling, 2012).

Microseisms are divided in primary and secondary microseisms related to the different types of interaction of the sea waves with the coast that produce them.

The primary microseisms are generated by surface waves incident on a sloping bottom in shallow water and have periods similar to the main sea swell (10-20 s) and frequency equal to that of the sea waves responsible for their generation (Fig. 5.2 and Fig. 5.3). Sea waves may travel great distances before primary microseisms are generated (Ebeling, 2012).

The secondary microseisms are generated only when ocean wave trains of the same frequency that travel in opposite directions meet. They are originated by the nonlinear interaction between direct and reflected swell waves that result in depth-independent half period (5-10 s) pressure variations with amplitude proportional to the product of wave amplitudes, and frequency double that of the opposite waves trains (Fig. 5.2 and Fig. 5.3). Opposing wave trains can be generated at or near storms in deep or shallow water; in this case energy is transported from the storm to a receiving station via microseisms. Another generation mode is in shallow water when an incoming wave train meets waves reflected from the coast; in this case, it is primarily ocean waves that transport the energy. Both generation modes may be active for any particular storm (Ebeling, 2012). Generally, the secondary microseisms are the strongest peak in the microseism noise spectrum.

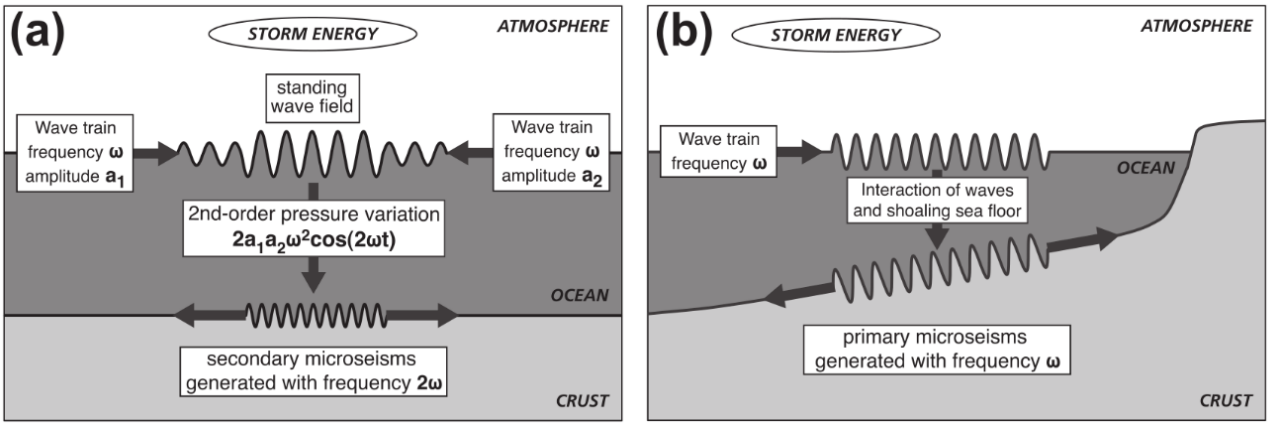

Fig. 5.2. Schemes of the microseism generation mechanisms of (a) secondary microseisms and (b) primary microseisms (Ebeling, 2012).

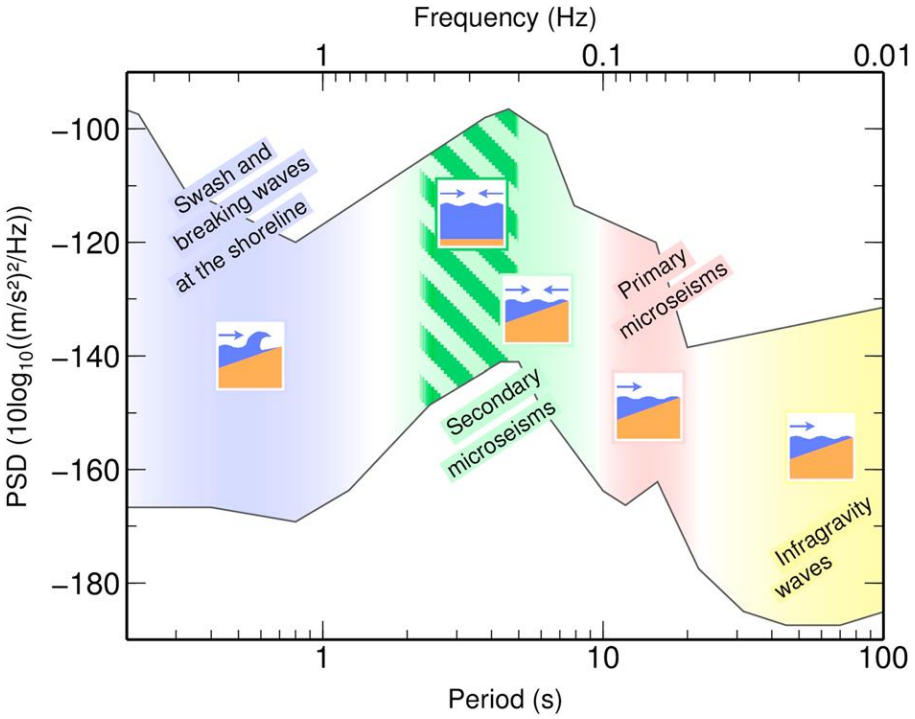

Fig. 5.3. Summary of the ocean signature on seismic energy recorded at Atlantic shoreline stations by Beucler et al. (2015). The seismic energy for periods lower than 2 s (blue area) is due to the wave breaking on cliffs or in swash areas; secondary microseisms generated in open ocean by opposite-waves trains prevail in the period band of 2.5–5 s (striped, green area); secondary microseisms generated in shallow areas prevail in 5-10 s band (green area); primary microseisms prevail in the 10-20 s period band over the 0.1 Hz frequency band (red area).

Thanks to their formation mechanism, the secondary microseisms can be associated with cyclonic depressions or a depression that is moving with the same velocity of the waves generated by it. These storms can be generated and can move over waters of any depth, thus allowing secondary microseism generation in deep waters. Moreover, the secondary microseisms can also be generated in shallow waters when conditions favourable to opposing wave train formation exist, such as when reflected swell interacts with incoming swell at coasts (Ebeling, 2012). Therefore, the site of secondary microseisms generation can be either in open sea/ocean or near the coast. The prevalence of one mechanism over the other does not seem to be definable, since different behaviours were observed in different sites in the world and at different moments, and seem to be dependent on different factors, such as the site geology, bathymetry, coastal geometry, or water depth (Beucler et al., 2015; Bormann et al., 2009; Li, 2018).

Starting from 1999, Bromirski et al. showed that elements of the wave climate can be accurately reconstructed using near-coastal inland broadband seismometer data. Due to the correlation between microseismic spectral power and ocean wave height and period, microseismic observation can be used as a tool to study local sea states. The authors proposed a site-specific, empirically derived seismic-to-wave transfer function applicable to seismic data recorded by seismic stations from the same location and demonstrated that ocean wave heights can be estimated from near-coastal broadband seismometer data.

Since the study of 1999, Bromirski and co-Authors have continued to explore this issue (Bromirski and Duennebier, 2002, Bromirski et al., 2005) and other several authors have deepened the research on the relationship between storms and sea-wave properties and microseismic signal (Ardhuin et al., 2012; Gualtieri et al., 2013; Obrebski et al., 2012; Stutzmann et al., 2012; Sufri et al., 2014; Xiao et al., 2018) due the complexity of the non-linear and frequency-dependent energy transfer between the atmosphere and the ocean

and the resulting transfer between the ocean and the solid Earth (Gualtieri et al. 2018). These studies were addressed to the determination of both the sea wave characteristics in real-time (on the base of short-period dataset) and the remote wave-climate and the reconstruction of sea states in the context of climate changes (on the base of long-period dataset; Zupo, 2015). Several authors proposed empirical functions and site-specific models of sea wave height restitution starting from microseismic signal analysis (Bromirski et al., 1999; Ardhuin et al., 2012; Cannata et al., 2020; Neale et al., 2017).

5.1. References

Ardhuin F., Balanche A., Stutzmann E., Obrebski M. (2012). From seismic noise to ocean wave parameters: General methods and validation. Journal of Geophysical Research 117: C05002. doi:10.1029/2011JC007449

Beucler É., Mocquet A., Schimmel M., Chevrot S., Quillard O., Vergne J., Sylvander M. (2015). Observation of deep water microseisms in the North Atlantic Ocean using tide modulations. Geophysical Research Letters 42. doi: 10.1002/2014GL062347.

Bonnefoy-Claudet S., Cotton F., Bard P.Y. (2006). The nature of noise wavefield and its applications for site effects studies - A literature review. Earth-Science Reviews 79: 205-227. doi: 10.1016/j.earscirev.2006.07.004

Bormann P., Baumbach M., Bock G., Grosser H., Choy G.L., Boatwright J. (2009). Seismic sources and source parameters. In: Bormann P (ed) New Manual of Seismological Observatory Practice 2 - NMSOP, Potsdam, pp. 1162. doi: 10.2312/GFZ.NMSOP_r1_ch3

Bromirski P.D., Duennebier F.K. (2002). The near-coastal microseism spectrum: Spatial and temporal wave climate relationships. Journal of Geophysical Research 107(B8). doi: 10.1029/2001JB000265.

Bromirski P.D., Duennebier F.K., Stephen R.A. (2005). Mid-ocean microseisms. Geochemistry Geophysics Geosystems 6(4): Q04009. doi: 0.1029/2004GC000768

Bromirski P.D., Flick R.E., Graham N. (1999). Ocean wave height determined from inland seismometer data: Implications for investigating wave climate changes in the NE Pacific. Journal of Geophysical Research: Oceans 104(C9): 20753-20766. https://doi.org/10.1029/1999JC900156

Cannata A., Cannavò F., Moschella S., Di Grazia G., Nardone G., Orasi A., Picone M., Ferla M., Gresta S. (2020). Unravelling the Relationship Between Microseisms and Spatial Distribution of Sea Wave Height by Statistical and Machine Learning Approaches. Remote Sensing 12(5): 761. https://doi.org/10.3390/rs12050761

Ebeling C.W. (2012) Inferring Ocean Storm Characteristics from Ambient Seismic Noise. In: Dmowska R. (ed) Advances in Geophysics, Elsevier, pp 1-33.

Gualtieri L., Camargo S.J., Pascale S., Pons F.M.E., Ekstrom G. (2018). The persistent signature of tropical cyclones in ambient seismic noise. Earth and Planetary Science Letters 484: 287-294. https://doi.org/10.1016/j.epsl.2017.12.026

Gualtieri L., Stutzmann E., Capdeville Y., Ardhuin F., Schimmel M., Mangeney A., Morelli A. (2013). Modelling secondary microseismic noise by normal mode summation. Geophysical Journal International 193(3): 1732–1745. https://doi.org/10.1093/gji/ggt090

Gutemberg B. (1951). Observation and theory of microseisms. T.F. Malone (Ed.), Compendium of Meteorology, American Meteorological Society, Providence, Rhode Island, pp. 1303-1311.

Li L. (2018). Understanding seismic body waves retrieved from noise correlations: Toward a passive deep Earth imaging. Doctoral dissertation in: Terre Solide (CETSOL), Communauté Université Grenoble Alpes, pp. 2014.

Longuet-Higgins MS (1950) A Theory of the Origin of Microseisms. Philosophical Transactions of The Royal Society A: Mathematical Physical and Engineering Sciences 243:1–35. doi: 10.1098/rsta.1950.0012

Longuet-Higgins MS, Ursell F (1948) Sea waves and microseisms. Nature 162:700. doi: 10.1038/162700a0

Marzorati S. (2007). Fenomenologia del noise sismico ambientale: dalla conoscenza del segnale alle applicazioni empiriche. Doctoral dissertation in: Scienze Geologiche e Geotecnologiche per l'Ambiente e il Territorio, Università degli Studi di Milano-Bicocca, pp. 182.

Neale J., Harmon N., Srokosz M. (2017). Monitoring remote ocean waves using P-wave microseisms. Journal of Geophysical Research: Oceans 122(1): 470-483. doi: 10.1002/2016JC012183.

Obrebski M.J., Ardhuin F., Stutzmann E., Schimmel M. (2012). How moderate sea states can generate loud seismic noise in the deep ocean. Geophysical Research Letters 39: L11601. doi: 10.1029/2012GL051896

Stutzmann E., Srdhuin F., Schimmel M., Mangeney A., Patau G. (2012). Modelling long-term seismic noise in various environments. Geophysical Journal International 191: 707-722. doi: 10.1111/j.1365-246X.2012.05638.x

Sufri O., Koper K.D., Burlacu R., de Foy B. (2014). Microseisms from Superstorm Sandy. Earth and Planetary Science Letters 402: 324-336. http://dx.doi.org/10.1016/j.epsl.2013.10.015

Xiao H., Xue M., Yang T., Liu C., Hua Q., Xia S., et al. (2018). The characteristics of microseisms in South China Sea: Results from a combined data set of OBSs, broadband land seismic stations, and a global wave height model. Journal of Geophysical Research: Solid Earth 123: 3923-3942. https://doi.org/10.1029/2017JB015291

Zupo M. (2015). Secondary Microseisms Characterization and Green's Function Extraction at the Larderello-Travale Geothermal Field (Italy). Doctoral dissertation in: Geofisica, Università di Bologna, pp. 172.

6 Application of microseism to the sea wave height estimation in the Ligurian Sea (Italy)

The first step in the study of the relationship between sea waves and microseism in the Ligurian Sea was carried out by Ferretti et al. (2013). They started their study on data from the October-November 2008 period and discussed the results comparing microseism data to sea wave data measured by the Côte d'Azur buoy (Météo-France) in the January-February 2012 period. Authors proposed an empirical law to estimate the significant sea wave height as a function of the vertical component of microseism:

$$H_{\frac{1}{3}}^{\text{calc}} = \exp\left(a + b \ln\left(\sqrt{\int_{f_{\min}}^{f_{\max}} \frac{2}{T}|S_m(f)|^2 \mathrm{d}f}\right)\right)$$

where $H_{1/3}$ is the significant sea wave height, $2/T|Sm(f)|$ is the power spectral density (PSD) of the microseism, T is the time of the window considered, a, b, f_{min} and f_{max} are the four unknown parameters of the estimation model. From the data available to them, Authors selected the 'best-fitting model' corresponding to:

$$\mathbf{m} = (f_{\min}, f_{\max}, a, b) = (0.24, 0.78, 9.48, 0.66).$$

The second step was the study entitled **Applicability of an empirical law to predict significant sea-wave heights from microseisms along the Western Ligurian Coast (Italy)** (Ferretti G., Scafidi D., Cutroneo L., Gallino S., Capello M., Continental Shelf Research 2016 122: 36-42. https://doi.org/10.3390/jmse9030319). In this study, Authors started from the model of Ferretti et al. (2013) and presented an updated procedure that utilises microseisms recorded by five seismic stations to estimate the significant sea wave height in the western Ligurian Sea. The calibration and validation of the procedure was performed using sea wave data obtained from the wave buoy of Capo Mele (ARPAL) in the June-December 2012 period. The calibration procedure therefore consisted of finding the four unknown parameters of the estimation law of Ferretti et al. (2013)(a, b, f_{min} and f_{max}) that best allow to estimate the wave height measured at the Capo Mele buoy. Authors calculated the mean of the significant sea wave height values estimated from the microseism recorded at each station to provide the final data of significant sea wave height:

$$H_{1/3}^{best} = \frac{1}{nsta} \sum_{n=1}^{nsta} H_{1/3}^{n}$$

where $nsta$ is the number of stations in the seismic network (in this case, five stations) and $H_{1/3}^{n}$ is the significant sea wave height obtained from the microseism recorded at the seismic stations. The results indicated that the differences between the significant heights measured by the Capo Mele buoy and the empirical procedure were less than 10 cm (corresponding to 10% of the mean measured value) for 47% of the data and less than 20 cm (corresponding to 20% of the mean measured value) for 72%.

The evolution of the study continued with the manuscript **Near real-time monitoring of significant sea wave height through microseism recordings: An application in the Ligurian Sea (Italy)** (Ferretti G., Barani S., Scafidi D., Capello M., Cutroneo L., Vagge G., Besio G., Ocean and Coastal Management 2018 165: 185-194, https://doi.org/10.1016/j.ocecoaman.2018.08.023) that was the starting point of the *Ph.D.* project. In this paper,

Authors proposed an automatic procedure for near real-time monitoring of significant sea wave height. This procedure used the microseism recordings provided by the network of nine seismic stations in Liguria to monitoring the sea wave height at five specific points (hindcast nodes) along the coasts (Fig. 6.1). Authors developed the procedure using a series of linked empirical estimation models, each calibrated for a specific wave height interval using hindcast data from the Ligurian Sea as sea wave height reference. The reference period of this study was between 1 January 2013 and 1 June 2014. The scheme summarising the functioning of the procedure is shown in Fig. 6.2. The procedure operation can be summarised as follows: the base model evaluates sea wave height at each seismic station and returns the mean value with the standard deviation (step 4 of Fig. 6.2); if the obtained sea wave height value (step 5 of Fig. 6.2) is lower than the 1-m threshold, the procedure eliminates the values resulting from teleseisms and returns the final sea wave height value (step 6); if the sea wave height value obtained is equal to or exceeds the 1-m threshold, the model calibrated on the values of sea wave height ≥1m intervenes and returns a new mean sea wave height; if the new sea wave height value is lower than 1.5 m, it is considered as valid and filtered by the eventual teleseisms; otherwise, the model calibrated on the sea wave height ≥1.5 m intervenes, and so on up to significant heights greater than or equal to 3 m.

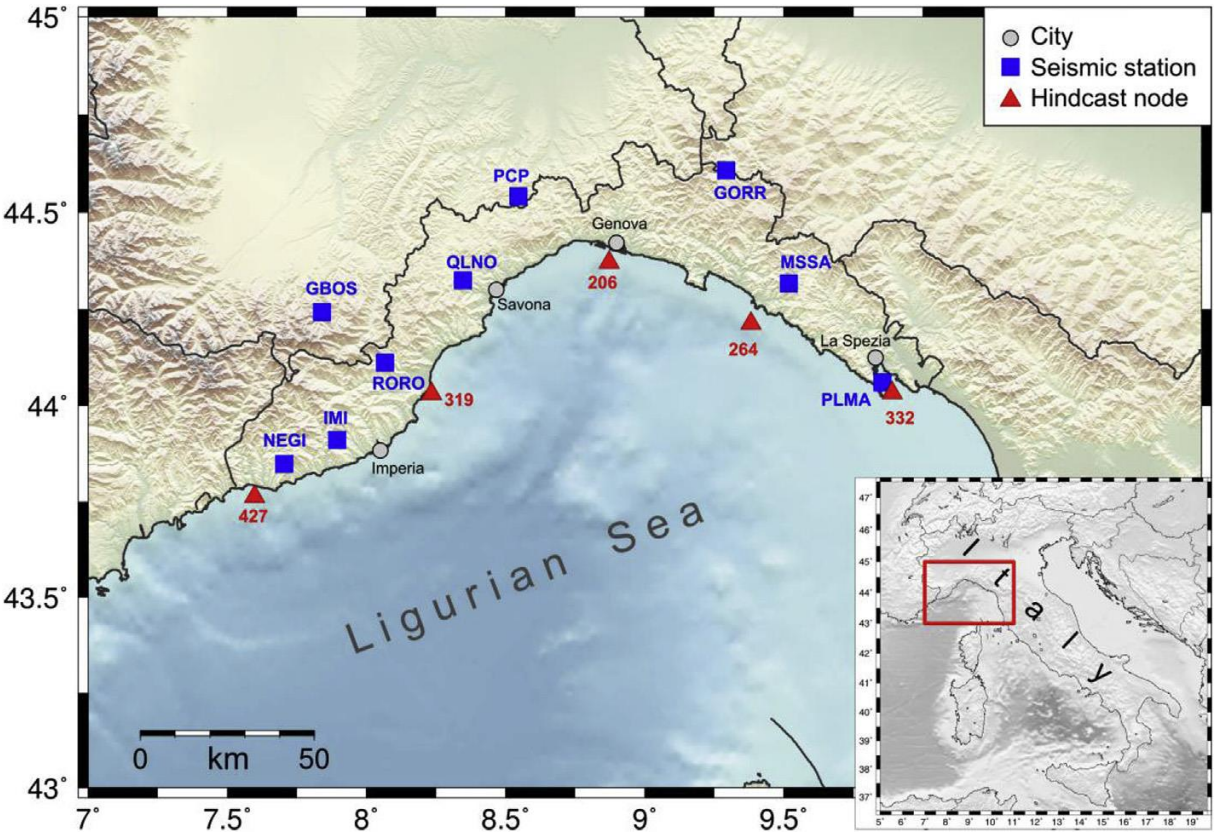

Fig. 6.1. Ligurian Sea and location of seismic stations (blue squares) and reference sea points (hindcast nodes, red triangles) considered in Ferretti et al. (2018).

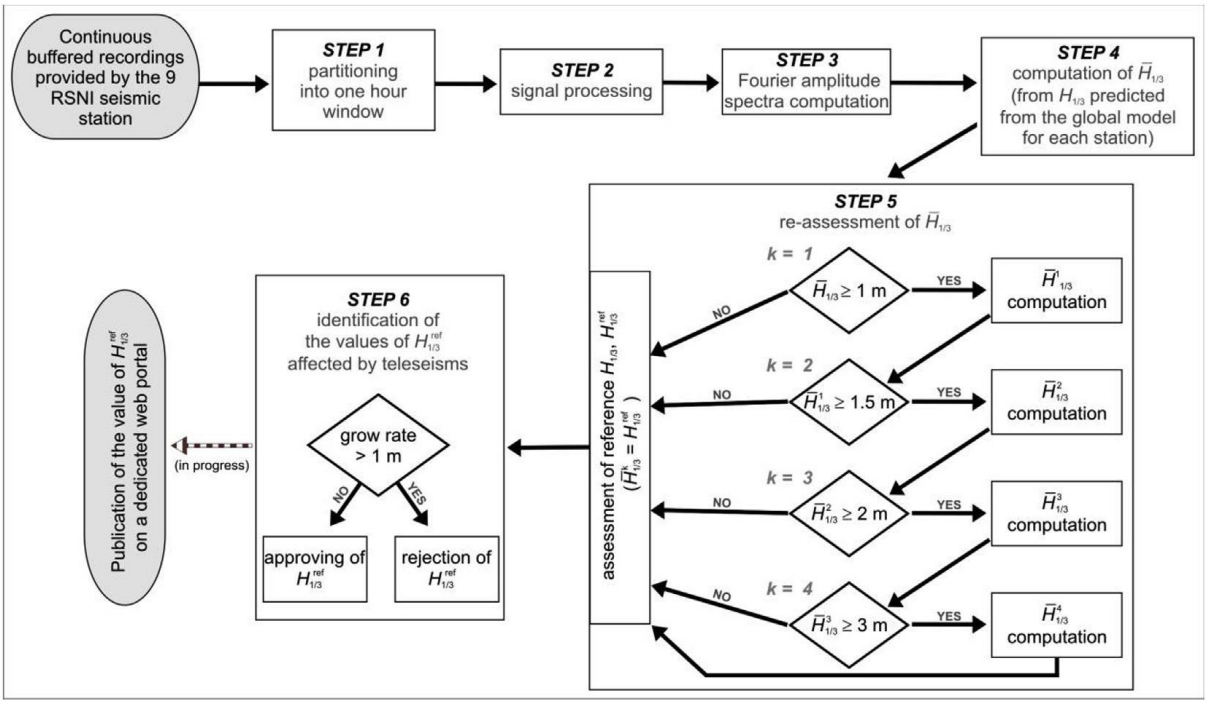

Fig. 6.2. Flowchart of the automatic procedure for estimating the significant sea wave height from microseism proposed by Ferretti et al. (2018).

Thanks to the application of statistical analysis and comparison with the hindcast data, the Authors highlighted that errors in the wave height measurement tend to be concentrated within two standard deviations of the mean, and that estimated wave heights fall within a few centimetres of the reference hindcast values. Only in very few cases, they have found discrepancies larger than 50 cm. For the final verification of the reliability of the estimated data, these were compared with those recorded by the wave buoy of Capo Mele. The results of the comparison showed very good agreement between observations and evaluations, with residuals rarely exceeding 40 cm. Overestimates of the buoy observations of more than 50 cm and underestimates of more than 20 cm have been observed very occasionally.

One of the main strengths of the procedure proposed by Ferretti et al. (2018) is that it exploits data from seismic stations, i.e. stations located on the territory and which, unlike wave buoys, are not subject to frequent damage and require much less maintenance than buoy, guaranteeing almost continuous temporal coverage. Thanks to the diffusion of the stations over the territory, the method also allows for extended spatial coverage, unlike the data measured by a buoy which have a purely punctual nature.

Consequently to this study, an internet page (Seism4Sea) for the visualisation of the estimated sea wave heights has been created (and continuously updated) on the DISTAV website (http://www.distav.unige.it/rsni/seism4sea.php), with links also from the MeteOcean webpage dedicated to the study of the ocean on the DICCA website (http://www3.dicca.unige.it/meteocean/wave_forecast.html). In this webpage, it is possible to see the significant wave height "measured" by the microseisms in real time (Fig. 6.3), and to print or save the image of the displayed sea wave height profile.

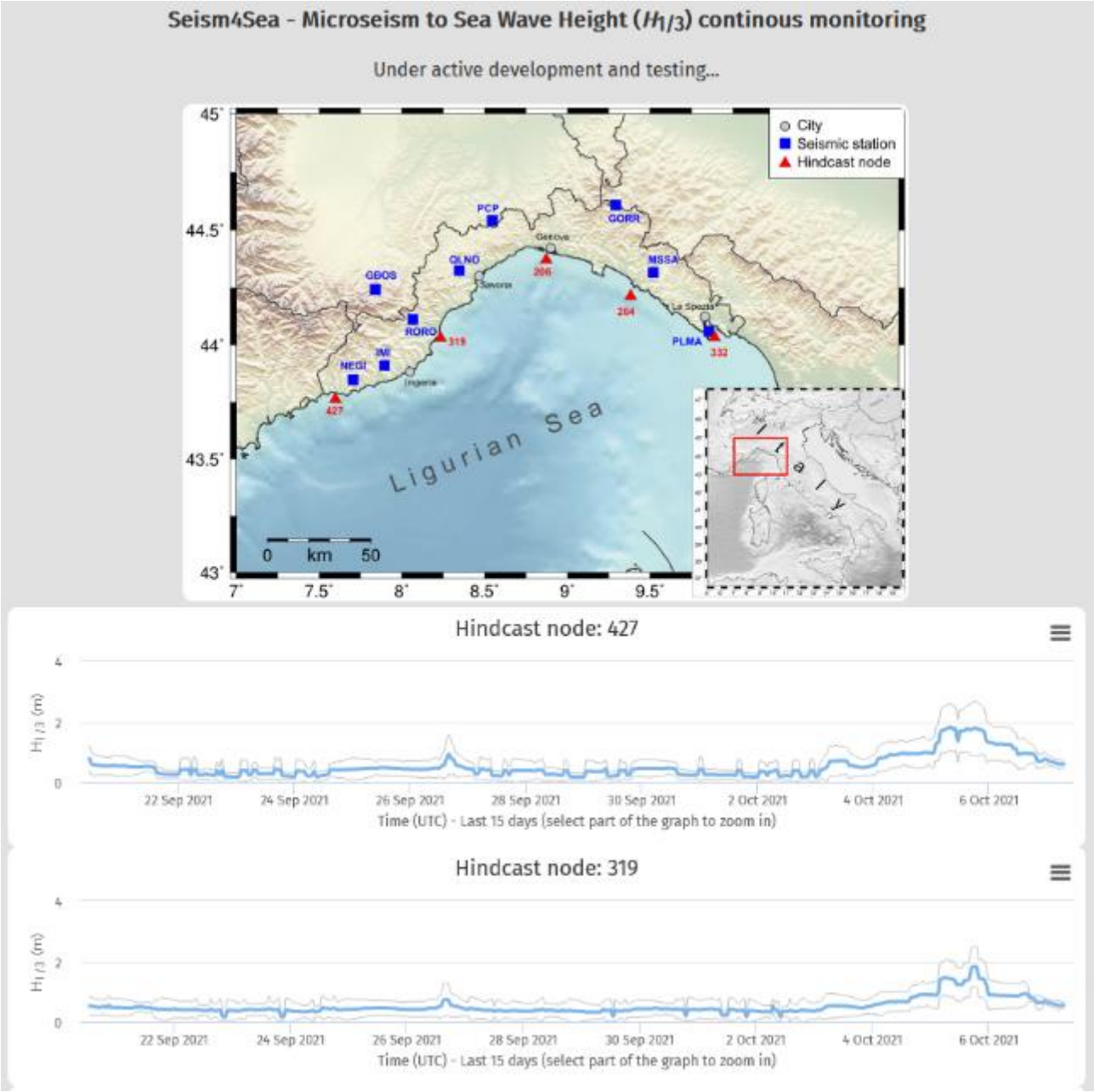

Fig. 6.3. Extract from the Seism4Sea webpage.

6.1. References

Ferretti G., Barani S., Scafidi D., Capello M., Cutroneo L., Vagge G., Besio G. (2018). Near real-time monitoring of significant sea wave height through microseism recordings: An application in the Ligurian Sea (Italy). Ocean and Coastal Management 165: 185-194. https://doi.org/10.1016/j.ocecoaman.2018.08.023

Ferretti G., Scafidi D., Cutroneo L., Gallino S., Capello M. (2016). Applicability of an empirical law to predict significant sea-wave heights from microseisms along the Western Ligurian Coast (Italy). Continental Shelf Research 122: 36-42. https://doi.org/10.3390/jmse9030319

Ferretti G., Zunino A., Scafidi D., Barani S., Spallarossa D. (2013). On microseisms recorded near the Ligurian coast (Italy) and their relationship with sea wave height. Geophysical Journal International 194: 524-533. https://doi.org/10.1093/gji/ggt114

7 Extreme sea storm of 2018 and paper published

In the context of the application of microseisms to the monitoring of the sea wave heights (H_s) in the Ligurian Sea, and the application and validation of the procedure provided by Ferretti et al. (2018), the extreme sea storm that occurred in the Ligurian Sea on 29 October 2018 (Adrian Storm) was taken into consideration by the *Ph.D.* project. In fact, despite its peculiar and rare (for the Ligurian basin) characteristics of H_s (maximum wave height 9.6 m and peak period 11.7 s measured from the Capo Mele buoy), it did not produce an equally energetic microseism and therefore generated an underestimation of H_s by the applied procedure. The refinement of the estimation model has allowed the production of a mathematical element that, thanks to the introduction of weather parameters (wind and atmospheric pressure), intervenes when the microseism is not energetic, and can therefore avoid underestimating H_s even in the case of an exceptional sea storm equivalent to that of 2018.

In order to obtain the final version of the manuscript, the study underwent numerous revisions that made it possible to:

- deep investigate the characteristics of the storm;
- focus on the most influential weather parameters characterising the storm;
- identify the most significant wave parameters during the storm;
- apply appropriate statistical analysis;
- insert a corrective element in the estimation procedure.

Journal of Marine Science and Engineering 2021, 9: 319

Near Real-Time Monitoring of Significant Sea Wave Height through Microseism Recordings: Analysis of an Exceptional Sea Storm Event

Laura Cutroneo[1], Gabriele Ferretti[1], Simone Barani[1], Davide Scafidi[1], Francesco De Leo[2], Giovanni Besio[2], Marco Capello[1]

1 DISTAV, University of Genoa, 26 Corso Europa, I-16132 Genoa, Italy.

2 DICCA, University of Genoa, 1 Via Montallegro, I-16145 Genoa, Italy.

https://doi.org/10.3390/jmse9030319

Abstract

Microseisms are used to estimate significant sea wave heights (Hs) in different parts of the world and also during extreme events (e.g., typhoons and hurricanes), as they are generated by the effect of sea waves on the sea bottom and are strictly related to the wave height. On 29 October 2018, an exceptional sea storm event (the Adrian storm) occurred in the Ligurian Sea (NW Mediterranean Sea), producing severe damage to coastal constructions and infrastructures. However, the microseism measured at seismic stations located near the coast did not show equivalent high energy, thus resulting in a severe underestimation of the Hs predicted. In the present study, the Adrian storm was compared to other sea storms that have occurred in the Ligurian Sea in recent decades. The aim of this paper is to statistically examine the distinctive peculiarities of the Adrian storm in order to find new parameters to insert in the empirical models used in the procedure recently implemented for monitoring of Hs through microseism recordings in the Ligurian Sea, improving the effectiveness in Hs estimates in cases of extreme events that do not produce high-energy microseisms. The results show that the additional parameters to be taken into account into the predictive model are the atmospheric pressure gradient and the wind intensity. A correction term is finally proposed and applied to the predictive model to significantly reduce the Hs underestimation.

Keywords: microseisms; significant sea wave height; automatic near real-time monitoring; extreme sea storm events; Adrian storm

1. Introduction

Sea wave height is one of the most relevant sea parameters to the monitoring and protection of coastal areas and to mitigation of marine risk associated with the occurrence of strong sea storm events. The study of the wave characteristics, such as wave period, wavelength, significant wave height, and return period of sea storm, is essential for the design of offshore and coastal infrastructures, such as oil platforms, wind farms, breakwaters and artificial reefs, and for their conservation [1,2]. Due to the impact of sea waves on economic activities, a great effort has been made in the last decades to develop methods for direct sea wave height measurements using wave buoys. Nonetheless, wave buoys are typically very expensive and problematic, especially regarding their installation and maintenance. Moreover, they usually provide discontinuous data (e.g., due to temporary damage) with poor spatial resolution (due to the low density of monitoring stations in sea areas). Most common alternative methods are based on numerical modelling [3,4], remote sensing [5–7], coastal radars [8,9], and microseism recordings [10–15].

Microseisms are produced by the pressure exerted by sea waves on the sea floor and propagate in the surface layer of seabed for hundreds of kilometres thanks to their low frequency content, which typically ranges between 0.05 and 0.5 Hz. Microseisms are classically divided into primary and secondary microseisms. Primary microseisms cover the same frequency range of ocean swells, between 0.05 and 0.1 Hz, and are generated by pressure variation induced by sea waves on the seabed in coastal areas. The secondary microseism shows half the period of ocean waves (3–10 s), corresponding to frequencies between 0.1 and 0.5 Hz. Its origin is associated with the interference of waves of similar periods but opposite directions. In this last category, three different classes of microseism are recognised: (I) microseism generated by a rapidly moving large storm system with wind and waves in many directions (including opposing waves); (II) microseism generated by reflection of sea waves impinging on the coast; (III) microseism generated by two opposing wave systems—that is, a wind-sea opposing a swell or two opposing swells. An exhaustive description of the theory behind the relationship between sea waves and microseisms is presented by Ardhuin et al. [16].

Microseisms have been used to estimate the significant sea wave height (H_s) since the 1990s and, nowadays, microseism-based predictive models are applied in different parts of the world [16–18]. Recently, Ferretti et al. [15] have also proposed a procedure for near real-time monitoring of H_s, with application in the Ligurian Sea (north-western Mediterranean Sea). This procedure uses the microseism recorded by the stations of the Regional Seismic network of north-western Italy (RSNI) [19] to monitor H_s at different target sites using a set of predefined models that are selected within an iterative scheme. All predictive models, each of which covers a specific wave height range, were calibrated from separate sets of H_s extracted from an 18-month hindcast database for the Mediterranean Sea [3,20]. The H_s values provided by the procedure were obtained by averaging the H_s values estimated from the microseism recorded at each station. Details about the multistep automatic procedure can be found in Section 3.2 of Ferretti et al. [15]. Currently, the procedure proposed by Ferretti et al. [15] is used for the near-real time monitoring of H_s along the Ligurian coast. The H_s values estimated through microseism recordings can be accessed at the web page http://www.dipteris.unige.it/rsni/seism4sea.php (accessed on 19 November 2020).

In recent years, microseism application to H_s prediction in the case of extreme weather events, such as cyclones, typhoons, and hurricanes [21–26], has largely developed with the aim of examining the microseism response to such events, and thus to improve standard monitoring networks.

On 29 October 2018, an exceptional sea storm (hereinafter, the Adrian storm), characterised by maximum wave height of 10 m and peak wave period (T_p) of 11 s [27], occurred in the Ligurian Sea (Figure 1), causing extensive damage to coastal assets and infrastructures along the Ligurian coast. The urban development of the Ligurian Region, as well as of many other Mediterranean regions, is mostly concentrated near the coastline, protected by few physical barriers—this is how extreme sea storm events can strike infrastructures, such as ports, roads and railroads, or commercial properties, such as restaurants and beach resorts located on the beaches [28]. The Adrian storm has caused considerable damages in both the eastern part of the Ligurian Region, such as, for example, to port structures and coastal roads, and in the western part of the region, such as damages to beaches and bathing establishments. Fifty-seven out of 63 Ligurian coastal municipalities have applied to the National Civil Protection for aid to deal with the damage caused by this storm [29]. Because of the consistent amount of damage, the Adrian storm represents one of the most significant events in the Ligurian Sea.

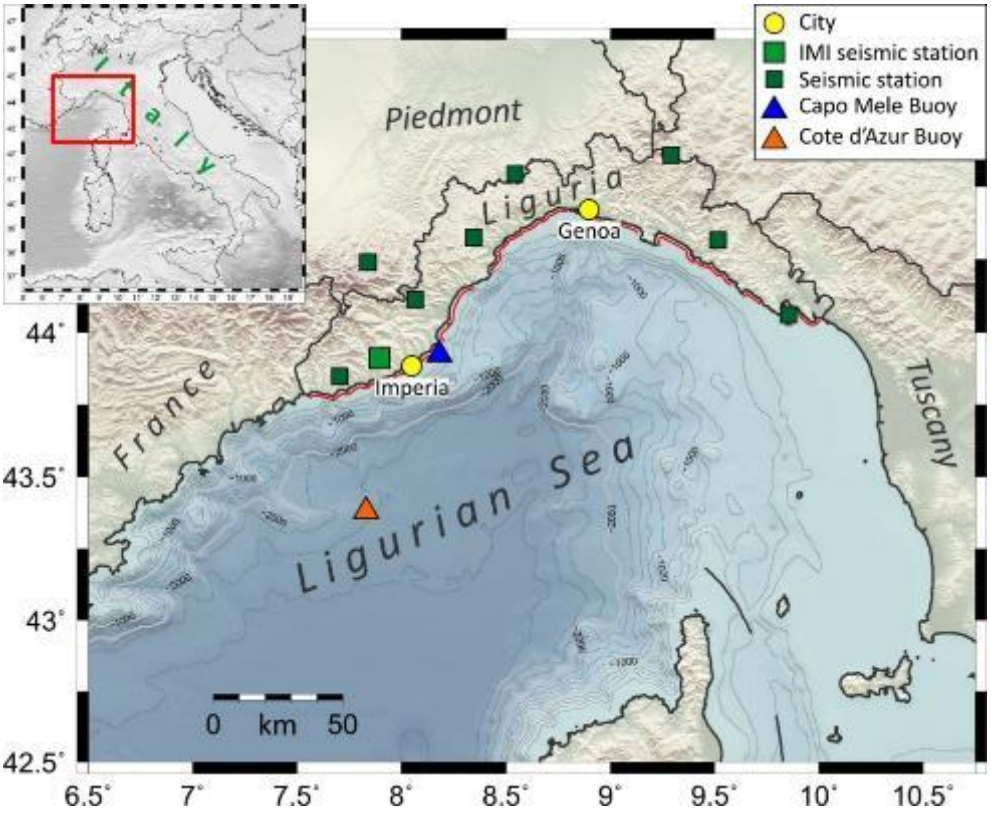

Figure 1. Location of the Imperia seismic station (IMI; large green square), the other Regional Seismic network of northwestern Italy (RSNI) seismic stations located near the Ligurian coast (small green squares) and the two buoys (Capo Mele–Italy and Cote d'Azur–France; blue and orange triangle, respectively) considered in this study. The tide gauge station of Imperia Porto Maurizio and the weather station of the Seismic and Meteorological Observatory of Imperia are located in the city of Imperia. Red line shows the coastal area affected by damages.

Despite these characteristics, the microseism recorded at several seismic stations of the RSNI network located along the Ligurian coast and in the hinterland did not show equivalent high

energy, with a consequent underestimation of the sea wave heights derived by Ferretti et al.'s [15] procedure. Thus, the Adrian storm offered the rare opportunity of analysing the characteristics of the microseism produced by this type of event and, therefore, to make a first attempt to understand why the use of microseism recordings could fail to estimate the H_s during extreme events. The aim of this study is to firstly identify and examine the distinctive peculiarities of the Adrian storm in order to improve future H_s estimations in the Ligurian Sea using additional informative parameters derived from other marine and weather observations (i.e., storm surge and atmospheric pressure). Since the Adrian storm has shown that predictive models based only on microseism data could not be completely effective for monitoring H_s during extreme storms, an empirical correction term is proposed here. Such a correction term has been applied to the predictive models proposed by Ferretti et al. [15], allowing for a significant reduction in the underestimation of the H_s observed during the Adrian storm.

2. Study Area and General Features of the Adrian Storm

The study area (Figure 1) is the coastal part of the Ligurian Sea in the western Mediterranean Sea. The Ligurian Sea has a narrow continental shelf (with an average distance from the coast of 10 km) with steep slope incised by submarine canyons located along the main waterways of the region [30]. The Ligurian coast (about 330 km long) has steep arch-shaped mountains interspersed with wide valleys that control and channel the air movements. In the Ligurian Sea, the most frequent and significant sea storms are generated by winds from SE (Sirocco), SW (Libeccio), and NW (winds coming from the Gulf of Lion in cyclonic rotation; "short" Libeccio). These winds are usually related to perturbations from the Atlantic Ocean and Gulf of Lion, which carry strong, humid, and warm winds. These morphological and meteorological characteristics imply frequent events of heavy rainfall and rough sea and make the Ligurian Sea one of the most active areas of cyclogenesis in Europe [31–35], with strong and very rapid changes in weather conditions. In the past, the most destructive sea storms occurred in 1898 and 1955 (sea state > 7 of the Douglas Sea Scale), causing severe damage to the structures and vessels in the Port of Genoa [36].

On 27 October 2018, a deep trough between the Arctic Ocean and North African coasts was established on the Iberian Peninsula, and then moved eastwards and hit the whole Italian peninsula, causing an intense SW flow in the mid-troposphere and an SE flow in the lower layers. On 29 October, the cyclogenesis on the Gulf of Lion has deepened and the flow on the eastern edge of the cut-off was intense and from S, with a consequent recall of hot and humid air of African origin in the central Europe. In the Ligurian Sea, in the early hours of 29 October, a V-shape structure developed. It was characterised by a strong, self-regenerating convective activity with a high vertical development, which stationed on the basin for several hours. The convective activity was characterised by the continuous formation of new storm cells produced by the downdraft in the opposite direction to the main flow, which therefore caused the persistence of thunderstorm phenomena on the basin. This structure was generated by several factors: the strong flows from SW at high altitude due to the tiling on the western Mediterranean Sea, the presence of a high quantity of water vapour, a high convective available potential energy, and high values of equivalent potential temperature.

In the afternoon of 29 October, the entire Italian territory was affected by the passage of a cold front coming from W, along which a squall line (a very intense thunderstorm line) developed, accompanied by intense precipitation and numerous lightning strikes along the cold front line. This complex scenario brought very low-pressure values (~978 hPa; Figure 2) which, combined with strong S winds, caused a storm surge phenomenon (i.e., a strong and rapid rise of the sea

surface elevation) that contributed to increase the effect of the sea storm. At its maximum intensity, the storm was characterised by wind gusts over 150 km h-1, H_s greater than 6 m, maximum wave height of 10 m, and peak wave period (T_p) of 11 s. This value of T_p is very rare in a closed sea such as the Mediterranean Sea. The development of the sea wave can be divided into two phases: a first phase during which the wave direction spanned between 120° and 160° (from 04:00 to 21:00 of 29 October), followed by a second phase during which the wave direction was mainly around 200°. In the Ligurian Sea, this shift in wave direction is very common during storm. In fact, the interaction of the synoptic flows with the complex mountain topography causes the development of deep orographic lows, usually very dynamic, that, in turn, cause very rapid transition of winds from SE to SW, with intensity strongly enhanced by coastal effects [37].

Since the night of 29 October, the perturbed system moved NE, leaving space for a gradual ascent of the geopotential field on 30 October [27,38,39].

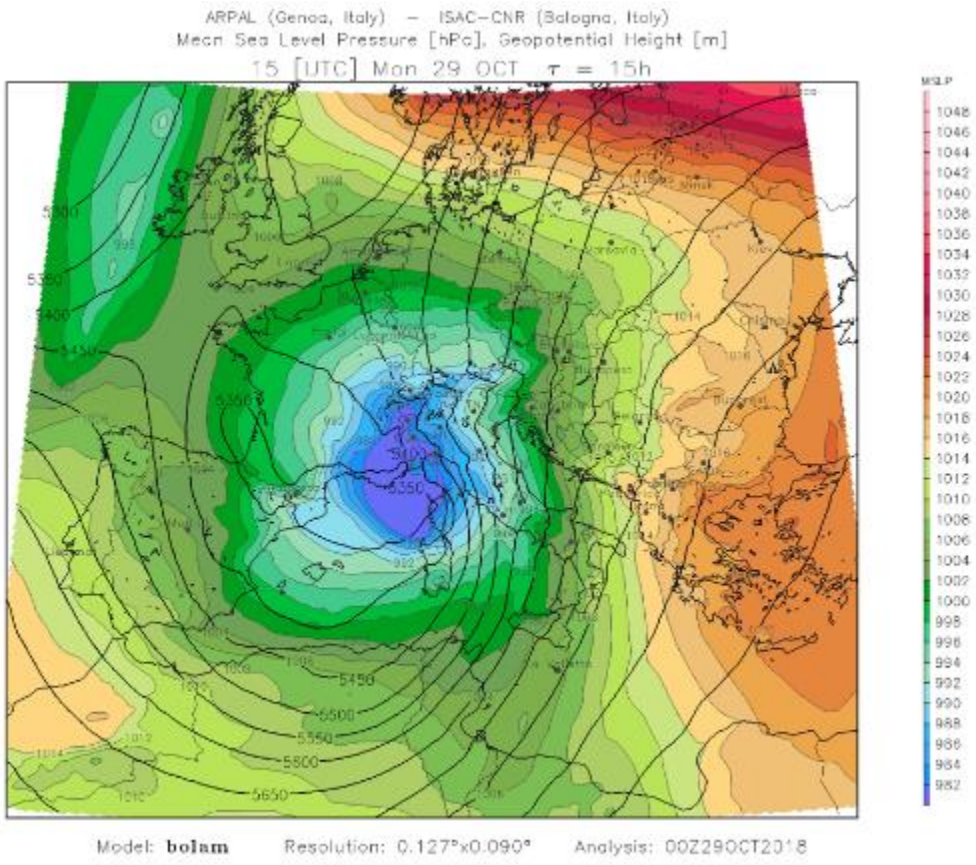

Figure 2. Maps of the mean sea level pressure (hPa, grey lines and colour fill) and geopotential height (m, black lines) on 29 October 2018 during the Adrian storm [27].

3. Materials and Methods

3.1. Weather and Sea Data

In order to examine the distinctive peculiarities of the Adrian storm to improve the procedure proposed by Ferretti et al. [15] for monitoring H_s from microseism recordings during strong marine events, four significant sea storms that occurred in the Ligurian Sea in 2008 and between 2012 and 2018 were analysed and compared to the recent Adrian storm. Specifically, the considered the events occurred on 30 October 2008 (the sea storm already considered by Ferretti et al. [13]), 28 October 2012, 10 November 2013, and 25 December 2013 (three sea storms

occurred in the period 2012–2018, for which continuous seismic recordings were available for analysis). All the sea storms considered were generated by strong southerly winds and showed H_s > 3 m. Data of sea wave characteristics, sea level, and atmospheric conditions were collected in order to highlight differences among these sea storms in terms of sea wave parameters and in terms of microseism characteristics.

For each selected sea storm, hourly H_s (in m), maximum individual sea wave height (H_{max}), wave direction and T_p were collected from buoys installed in the Ligurian Sea. In particular, for the event that occurred in 2008, we analysed data measured by the Côte d'Azur buoy (latitude 43.38° N, longitude 7.83° E, depth of anchoring 2300 m), which belongs to the Meteo-France network (www.shom.fr (accessed on 19 November 2020)). Concerning the 2012, 2013, and 2018 events, data measured by the buoy of Capo Mele (latitude—43.92° N, longitude—8.18° E, depth of anchoring—90 m), which is managed by the Ligurian Environmental Protection Agency (http://servizi-meteoliguria.arpal.gov.it/boacapomele.html (accessed on 19 November 2020)), were considered. Sea level (m), atmospheric pressure (hPa), and relative humidity (%) data measured during the five sea storms were collected from the tide gauge station of Imperia Porto Maurizio (part of the National Tide-gauge Network; www.mareografico.it (accessed on 19 November 2020)) located 13 km far off the Capo Mele buoy.

Wind direction (° N) and velocity (m s^{-1}) were obtained from the Seismic and Meteorological Observatory of Imperia (managed by the Municipality of Imperia; http://www.cartografiarl.regione.liguria.it/SiraQualMeteo/script/PubAccessoDatiMeteo.asp (accessed on 19 November 2020)) located 14 km SW off the Capo Mele buoy. The two measuring stations and the buoy of Capo Mele are not colocated, but given the relatively small distance between them, the effect of this distance on the results of the analyses is assumed negligible given the noninstantaneous inertia of the system (i.e., the sea).

All data were sampled hourly.

Starting from the water level records (provided by the station of Imperia Porto Maurizio), the storm surge series were computed for each of the investigated events. First, the tidal contribution was predicted through the Tidal Model Driver (TMD) package for MATLAB software (TMD software v. 2.05, [40]) provided by the Earth & Space Research (https://www.esr.org/research/polar-tide-models/tmd-software/ (accessed on 19 November 2020)). Then, the predicted tides were taken off the total water level, leading to the tidal residual. When tides are relevant, it is advisable to split the tidal residual in two contribution, i.e., a low-frequency and a high-frequency signal, corresponding to the meteorological-induced surge and the interaction between the tides and the surge [41]. However, given that in the Ligurian Sea the tidal oscillation accounts to a few centimetres at most over the total water level, we assumed the tidal residual was driven only by the storm surge.

In addition to the previous data, the distance between the Capo Mele buoy and the minimum of atmospheric pressure was estimated (in km) for each considered event. This distance can be useful to explain the oscillation of the microseism amplitude [25], and therefore to explain the relation between this latter and the H_s generated during the storms.

Finally, a statistical analysis was carried out in order to find the most influential atmospheric parameters during the Adrian storm. Specifically, the Redundancy Analysis (RDA) [42] multivariate technique was applied to explain the linear relationship between the explanatory variables, which are the atmospheric forcing (wind velocity, atmospheric pressure and pressure

gradient), and the response variables, which are the sea responses to such forcing (storm surge, H_s, and T_p). For each storm and for each parameter of interest, the analyses were carried out on ordered time series of 25 hourly samples around the time of the H_{max}. Details of the method used for the RDA analysis are described in Cutroneo et al. [43]. The RDA was performed using the Brodgar software (Highland Statistics Ltd., v. 2.7.5, 2017).

3.2. Microseismic Data

In this study, we present the results of the analysis of the microseism recorded at the IMI station (Figure 1), which is the RSNI station closest to the Capo Mele buoy. For all storms, only the vertical component of the signals was considered.

Following Ferretti et al. [13–15], microseismic data were processed according to the following steps:

1. Instrumental correction (deconvolution).
2. Signal resampling at a frequency of 2 Hz.
3. Offset and linear trend removal.
4. Signal windowing into 1 hr windows.
5. Computation of the Fourier transform for each window.
6. Spectrogram calculation.

The spectral characteristics of the microseism were thus determined through Fourier amplitude spectra and spectrograms.

4. Results

Following the methods described above, the sea wave parameters (derived from measuring buoys and microseisms) and atmospheric pressure data were analysed for the five sea storms considered in this study.

4.1. Microseism Analysis

Figure 3 compares H_s measured by the buoys (red lines) and those obtained using microseism recordings according to the procedure of Ferretti et al. [15] (green lines). Except for the Adrian storm (Figure 3e) and for the initial phase of the November 2013 event (Figure 3c), H_s measured by the buoy and H_s estimated by microseism were similar with differences that, on average, are lower than 0.2 m. During the Adrian storm, the Capo Mele buoy measured H_s greater than 6 m, which are almost twice the values estimated using the microseism.

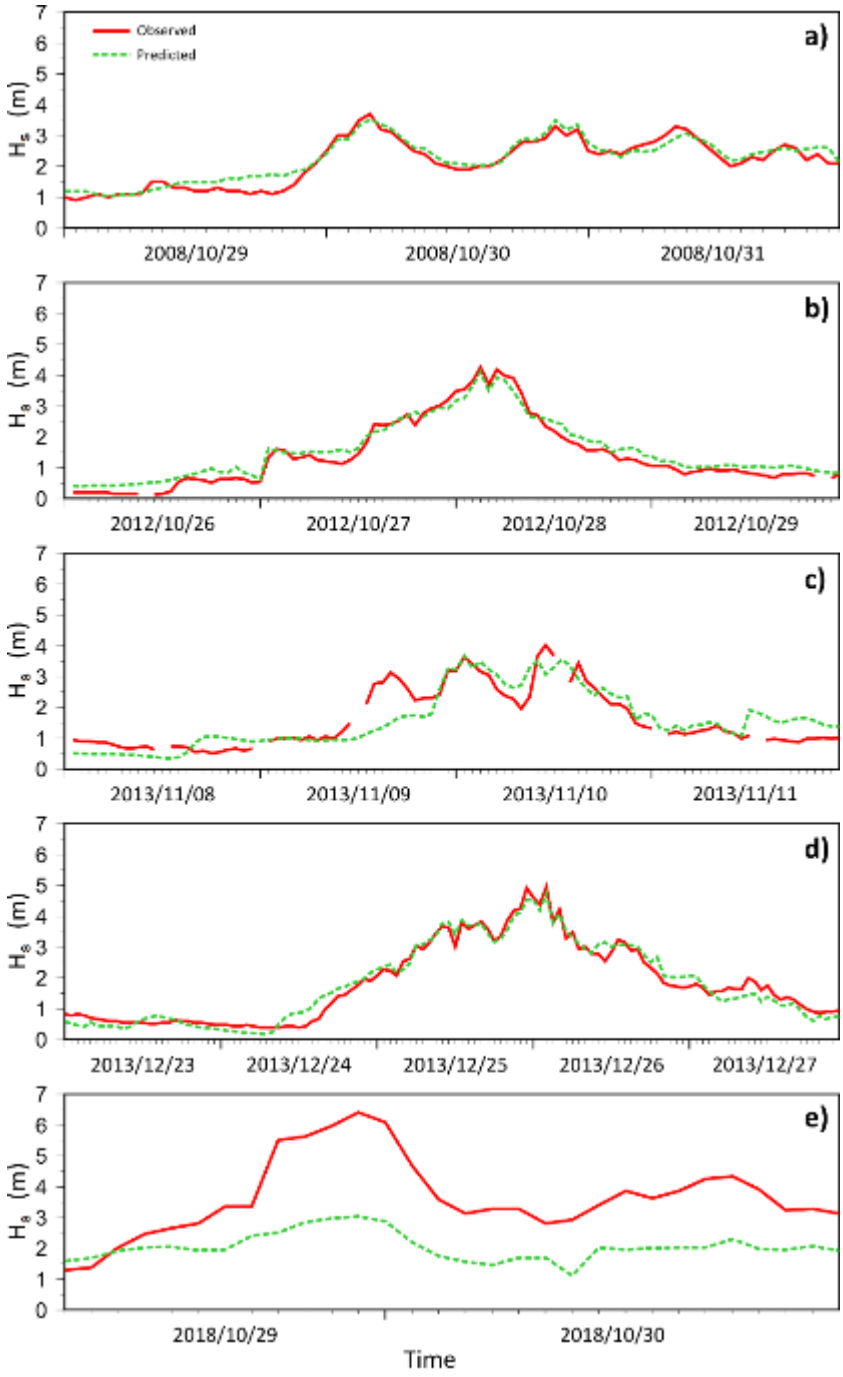

Figure 3. Comparison between the significant sea wave heights (H_s) measured by the buoys (red lines) and those estimated using microseism recordings (green dotted lines) during the five considered sea storm events: (**a**) October 2008; (**b**) October 2012; (**c**) November 2013; (**d**) December 2013; (**e**) October 2018. The time window considered is not the same for all sea storm due to lack of data.

Figure 4 shows the characteristics of the microseism recorded at the IMI station during the five sea storms in terms of the Fourier amplitude spectra for different hourly signal windows and spectrograms. As already shown by Ferretti et al. [13], the microseism associated with sea storms in the Ligurian Sea is dominated by frequencies of around 0.2–0.3 Hz, whereas the microseism controlled by frequencies lower than 0.15 Hz is associated with storms located in the Atlantic Ocean. For all sea storms considered in the present study, the largest microseism amplitude concentrates around 0.2 Hz. During the 2008, 2012, and December 2013 events, the spectral

amplitude at 0.2 Hz exceeded, on average, the value of 6×10^{-7} m s^{-1}, reaching values greater than 8×10^{-7} m s^{-1}. On November 2013, during the sea storm that generated the lowest H_{max} (Table 1), the spectral amplitude of microseism slightly exceeded 4×10^{-7} m s^{-1} and a significant underestimation of the H_s provided by microseism (up to 1.5 m) has been observed during the initial phase of the storm (Figure 3c). During the Adrian storm, the spectral amplitude of the microseism at 0.2 Hz remained nearly below 2×10^{-7} m s^{-1}.

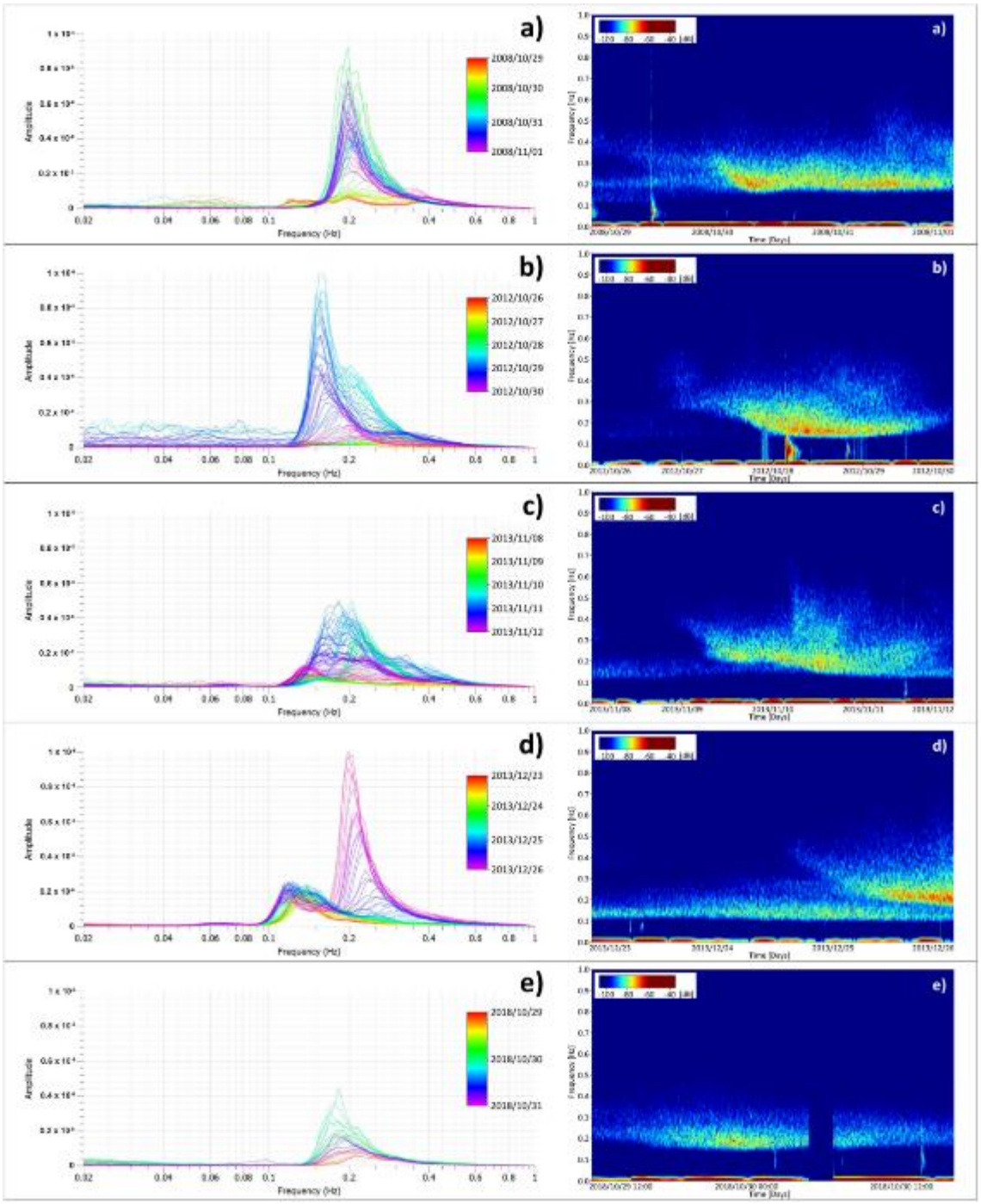

Figure 4. Fourier amplitude spectra (normalised to the duration of the signal) for all one-hour windows in which each microseism recording was divided (on the left) and spectrogram of the vertical component of the microseism recorded during the five sea storms under study (on the right). (**a**) October 2008; (**b**) October 2012; (**c**) November 2013; (**d**) December 2013; (**e**) October 2018. The time window considered is not the same for all sea storm due to lack of data.

Table 1. Weather and sea data for the five sea storm events considered in this study. n.a.: not available.

Sea Storm	Sea Storm Peak (dd/mm/yyyy hh:mm)	Period Considered for Weather Condition Evaluation (dd/mm/yyyy hh:mm)	Maximum Sea Wave Height (H_{max}, m)	Maximum Significant Sea Wave Height (H_s, m)	Peak Sea Wave Period (T_p, s)	Mean Wave Direction during the Sea Storm Peak (°N)	Maximum Storm Surge (m)	Minimum Atmospheric Pressure (hPa)	Maximum of Mean Wind Velocity ($m\ s^{-1}$)	Estimated Distance between the Capo Mele Buoy and the Minimum of Atmospheric Pressure (km) at the Maximum H_s Moment
October 2008	30/10/2008 n.a.	26/10/2008 00:00 - 31/10/2008 23:30	n.a.	3.7[1]	n.a.	n.a.	n.a.	n.a.	n.a.	22
October 2012	28/10/2012 03:00	22/10/2012 00:00 - 28/10/2012 23:30	6.37	4.16	9.97	216	0.47	984.3	8.6	88
November 2013	10/11/2013 11:00	05/11/2013 11:00[2] - 10/11/2013 23:30	6.02	4.02	9.67	340	0.23	1000	9.7	25
December 2013	25/12/2013 23:00	20/12/2013 00:00 - 26/12/2013 23:30	8.40	5.14	10.5	185	0.29	984.4	11.3	105
October 2018	29/10/2018 22:00	24/10/2018 00:00 - 30/10/2018 23:30	9.61	6.08	11.7	246	0.61	977.7	16.1	25

[1]Significant sea wave height collected by the Côte d'Azur buoy [13].

[2]Data before 05/11/2013 11:00 UTC were not available.

It is noteworthy that the H_s values estimated using the procedure of Ferretti et al. [15] and reported in Figure 3 have been computed considering the microseism recordings provided by the RSNI seismic stations located along the Ligurian coast (the H_s values is calculated by averaging over the nine stations shown in Fig. 1). The underestimation of the H_s provided by the procedure of Ferretti et al [15] is due to the low energy of the microseism recorded along the Ligurian coast during the Adrian storm. In fact, all recordings provided by the other RSNI seismic stations located along the Ligurian coast (Fig. 1) show microseism characteristics as similar as those observed at the IMI station. Moreover, the H_s values predicted by microseism show a significant underestimation at all target sites considered in the Ferretti et al.'s [15] procedure and located along the Ligurian coast. The predicted H_s values never exceed 3.5 m at any target site while indirect observations (such as damages to coastal infrastructures) indicate sea waves with certainly much greater heights along the entire Ligurian coast (see previous paragraphs).

Similar considerations on the microseism energy can be observed from the spectrograms (Figure 4). For the events occurred in 2008, 2012, and 2013, the spectral amplitude values for the frequencies dominating microseism recordings reached values greater than -65 dB, whereas during the Adrian storm they rarely exceeded -75 dB.

4.2. Weather and Sea Data Analysis

Table 1 summarises the main weather and sea parameters measured during the five sea storms considered. The H_{max} spans between 6 m (November 2013 event) and 9.6 m (October 2018 event), whereas the maximum H_s spans between 3.7 m (October 2008 event) and 6.1 m (October 2018 event). The T_p observed during the five sea storms ranges between 9.7 s (November 2013 event) and 11.7 s (October 2018 event). The maximum storm surge is between 0.29 and 0.47 m for the 2012 and 2013 events, and 0.61 m for the 2018 one. The minimum atmospheric pressure spans between 970 hPa (October 2018 event) and 1,000 hPa (November 2013 event). The mean wind velocity reached the maximum value of 11.3 m s^{-1} for the 2012 and 2013 storms, while reached the maximum value of 16.1 m s^{-1} during the 2018 storm. It appears clear that the Adrian storm has the highest H_s, the highest T_p, the highest storm surge, the lowest atmospheric pressure, and the highest mean wind velocity. The distance between the study area and the centre of the low pressure indicates two possible group of storms: the first group collects sea storms occurred when the pressure minimum was very close to the study area with distances less than 25 km (October 2008, November 2013, and October 2018 events); the second group is characterised by distances greater than 88 km (October 2012 and December 2018 events).

Figure 5 shows the evolution of storm surge, atmospheric pressure, H_s, and mean wind velocity measured during four of the five sea storms considered (no data are available for the 2008 event). Noteworthy is the fact that the rapid decrease of the atmospheric pressure values, the strong increase in wind velocity, and the related large storm surge, were almost simultaneously only during the Adrian storm. In fact, during the 2012 storm, the minimum of atmospheric pressure preceded the increase of wind velocity and storm surge, while during the 2013 storms, the increase in wind velocity preceded the decrease in pressure and the rise of storm surge.

Figure 6 shows the time variation of H_s and the atmospheric pressure gradient for hourly time windows for the four sea storms. It is evident that the Adrian storm is associated with an anomalous baric gradient trend, showing a wider and steeper pressure variation occurred in a very short time.

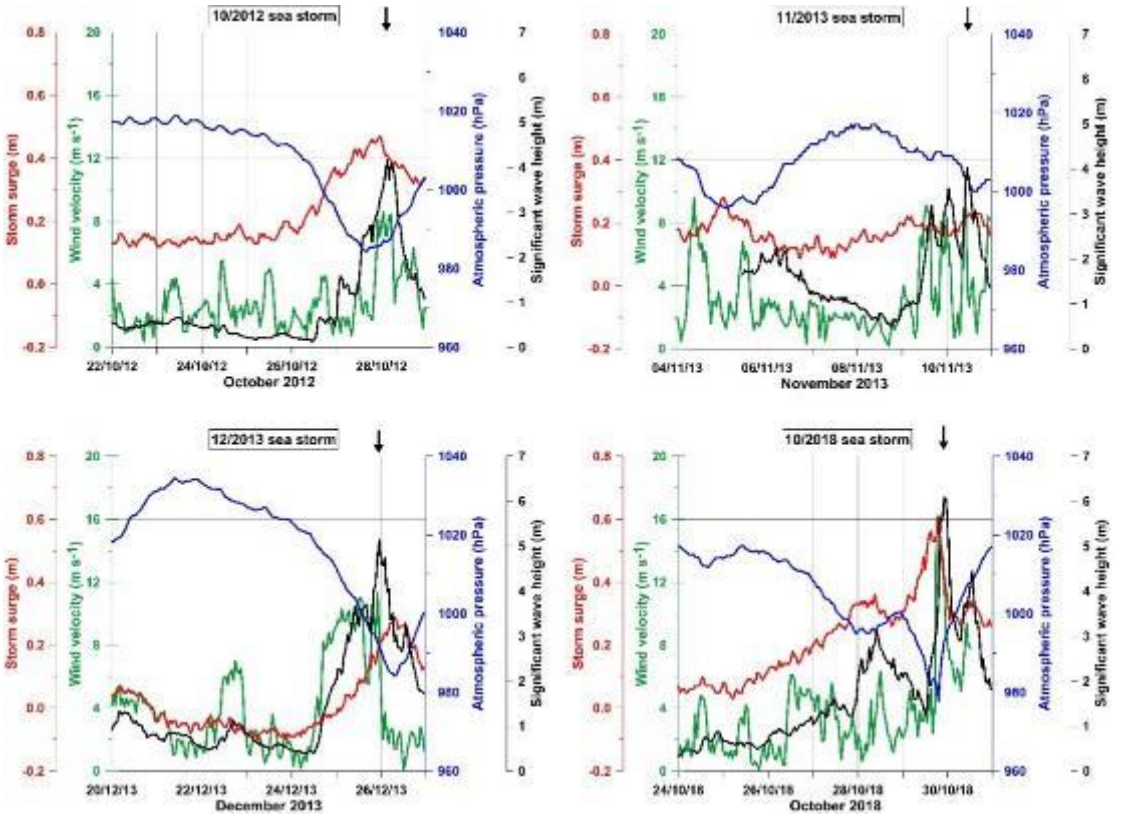

Figure 5. Storm surge (red lines), atmospheric pressure (blue lines), mean wind velocity (green lines) measured by the Imperia stations, and significant sea wave height (black lines) measured by the Capo Mele buoy. Black arrows indicate the time of the maximum sea wave height.

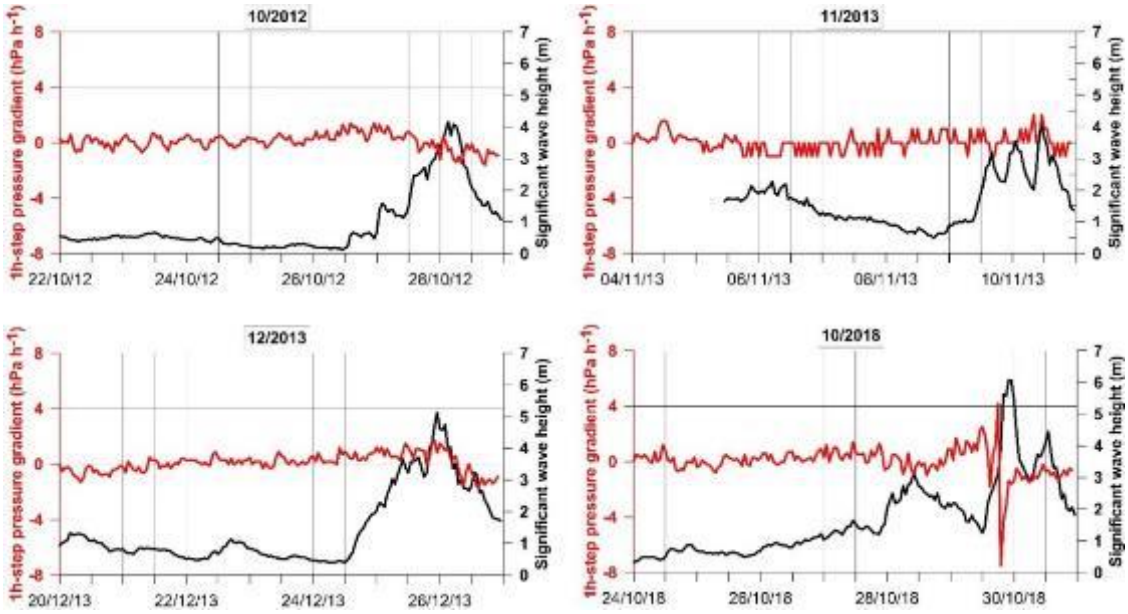

Figure 6. Significant wave height (m, black lines) superimposed on the temporal variation of the baric gradient (hPa, red lines) for hourly time window for a period of seven days around the sea storms of October 2012, November and December 2013, and October 2018.

Figure 7 summarises the results of RDA. In this plot, the angles between all vectors reflect their (linear) correlation. The correlation is equal to the cosine of the angle between vectors. Right-

angled projections of observation points onto vectors representing response variables approximate variable values for a given observation. Considering overall the results of RDA, the atmospheric pressure is slightly more informative in explaining the variability of the sea wave parameters, followed by the wind velocity. Considering individual parameters, the atmospheric pressure is positively related to T_p and negatively related to storm surge. Focusing on H_s, the most significant parameter in our study case, Figure 7 shows that H_s is strictly correlated with pressure gradient and wind velocity. Moreover, data recorded around the maximum development of the Adrian storm (data between 4_9 and 4_16 highlighted in light blue in Figure 7) are associated with the highest values of H_s, wind velocity and pressure gradient.

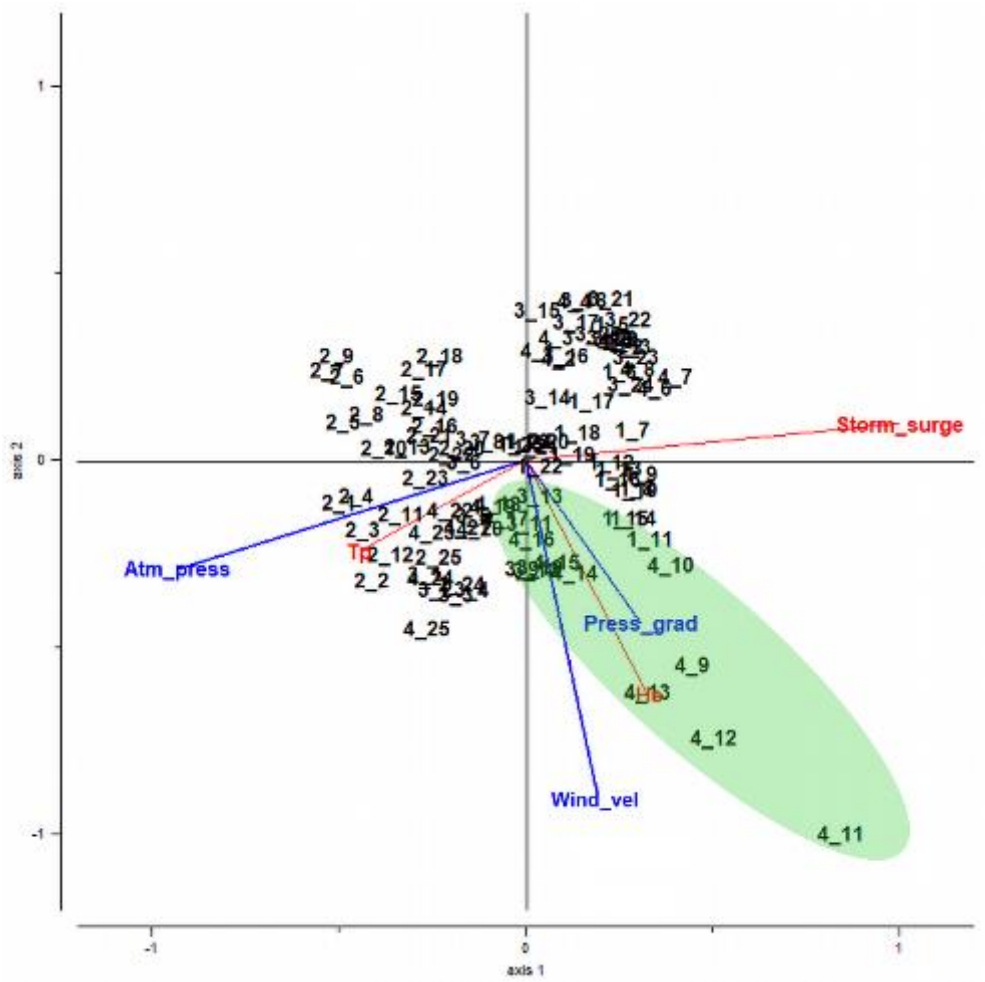

Figure 7. RDA plot showing the relationship between the explanatory variables (Wind_vel: wind velocity; Atm_press: atmospheric pressure; Press_grad: gradient of atmospheric pressure) and response variables (Storm_surge: storm surge; Hs: significant sea wave height; Tp: peak period of sea wave). Each event is indicated using double numbering: the first number indicates the sea storm event (1: October 2012; 2: November 2013; 3: December 2013; 4: October 2018) while the second one indicates the sample number (from 1 to 25). The sum of all canonical eigenvalues is 0.34.

5. Discussion

Through the analyses performed in the present study, the distinctive peculiarities of the Adrian storm have been examined. With respect to the other storms considered, the Adrian storm showed very peculiar features in terms of microseismic energy and meteorological-oceanic parameters. Specifically, during the Adrian storm, the pressure gradient has been significantly steeper than during the other events, and the wind velocity and the storm surge resulted very high values. The

microseismic frequency content was akin to the other storms, but its energy has been proved to be significantly lower, leading to an underestimation of the H_s value provided by the procedure proposed by Ferretti et al. [15].

The exceptionality of the Adrian storm was confirmed by comparison of its peculiar features with bibliographic data. For example, storm surge, primarily due to the wind associated with transit or stationery (24-48 h) low-pressure systems at medium latitudes [44], is generally weak in semienclosed basins such as the Mediterranean Sea. Ullmann and Pirazzoli [45], who analysed storm surges measured at three tide gauge stations located along the coast of the Gulf of Lions (north-western Mediterranean Sea) between 1948 and 2003, found that more than 80% of storm surges ≥ 0.60 m (as recorded during the Adrian storm) are associated with winds >10 m s^{-1}, which mostly contribute to the storm surge peak. Nevertheless, storm surge values ≥ 0.60 m are not frequent in the Mediterranean Sea, except for areas such as Venice lagoon (north-eastern Italy), and occur one time per season [45]. During the Adrian storm, the simultaneous strong decrease in atmospheric pressure and strong increase in wind speed, with a large fetch involving a vast portion of the Mediterranean, have contributed to the exceptional height of the storm surge. Moreover, during its peak, the sea waves were characterised by a peak period of 11.7 s, an extreme value relatively to the Mediterranean Sea. Pasi et al. [46] have observed that, in the period 1998–2010 (out of our study period), a sea storm characterised by a similar T_p occurred only once in the Ligurian Sea (on 1–2 January 2010) and, in the same 12-year period, they noted that sea storms with H_s greater than 4.3 m are generally characterised by mean wave periods of about 8.4 s.

Despite its meteorological-oceanic characteristics, the Adrian storm did not produce a high-energy microseism. As is well known, there is a strong correlation between H_s and local microseisms [13–15,47], but the generation mechanism of (primary) microseisms requires the sea surface-waves to interact with the sea bottom—namely, it occurs mainly in coastal areas with water shallower than half of the wavelength [48]. The correlation between sea waves and microseisms also depends on the duration of the storm; Traer et al. [48] found that sea waves typically evolve over a scale of days and that microseism features change with a similar time scale. Ardhuin et al. [49] found that an atmospheric perturbation that moves quickly and affects an area of shallow water near the coastline generates a weak conversion of wave-induced pressure to seismic noise. Therefore, sea waves produced by the Adrian storm had great energy, but their very rapid development, the position of the pressure minimum very close to the coast, and the very rapid variation of wave direction (from SE to SW) may have prevented the generation of a high-energy microseism. It is noteworthy that, a microseism with energy less than expected has also been observed during the November 2013 storm which developed very close to the Ligurian coast (see Table 1).

These effects along with a very high storm surge and a very high wind velocity may explain the nature of the Adrian storm, characterised by very high sea waves but a low-energy microseism. In summary, during this storm, the exceptional meteorological conditions (i.e., wind velocity and pressure gradient) and their spatial-temporal trend caused a peculiar response of the Ligurian Sea (in terms of storm surge, period and height of sea waves), linked to an anomalous microseism.

Although the mechanism of the microseism origin is difficult to discriminate in the Ligurian Sea, as already highlighted by Ferretti et al. [13], the secondary microseism, being by far stronger than the primary microseism, is probably the dominant influence on the microseism-based predictive models proposed by Ferretti et al. [15] for near real-time monitoring of H_s. Therefore, during the Adrian storm, because of the peculiarities listed above, the generation of a secondary microseism has been exceptionally low, leading to an underestimation of H_s. Unfortunately, at the moment,

we cannot suggest any explanation for which the situation is not favorable for generating secondary microseisms during some storms (such the Adrian one). Following our results, in order to avoid a significant underestimation of the H_s during future extreme sea storm events and, therefore, to improve the effectiveness of the procedures for real-time monitoring of the H_s through microseismic data, we can only propose adding the pressure gradient together with the wind velocity into microseism-based predictive models. These parameters are nowadays easily available from weather station networks.

Therefore, an empirical correction of the prediction model is proposed here. According to our results, the correction term must be applied to the predictive model only when extreme values of wind velocity and pressure gradient are observed. Specifically, it is assumed the correction term must be applied only when the hourly wind velocity values or the absolute values of the pressure gradient exceed the 95th percentile of data distribution. Considering data measured during the 2012, 2013, and 2018 events, the 95th percentile of wind velocity and pressure gradient data distributions are 8.4 m s^{-1} and 1.1 hPa h^{-1}, respectively.

The correction term has been derived and calibrated considering two main pieces of empirical evidence that are:

1. the differences between H_s measured by the buoy and those obtained by microseism linearly increase when the wind velocity and the absolute values of pressure gradient increase;

2. the increases of wind velocity and absolute values of pressure gradient produce an increase of H_s with a delay up to 5 h (Figure 8). Then, the most suitable correction parameters are estimated averaging six samples of wind velocity and absolute values of pressure gradient.

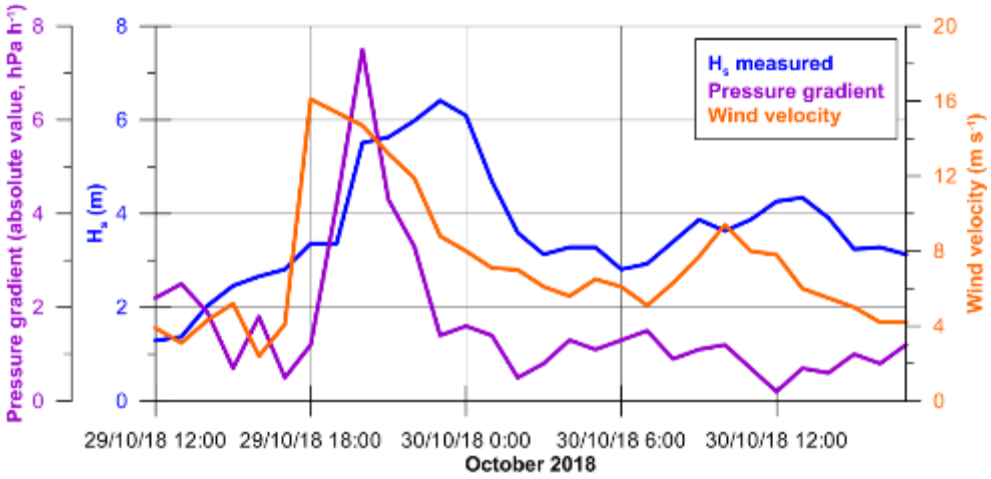

Figure 8. H_s measured (blue line), pressure gradient (violet line) and wind velocity (orange line) during the Adrian storm.

Finally, the model of Ferretti et al. [15] was modified accordingly as follows:

If

$$WMV_{i-6} > 8.4\ \left(m\ s^{-1}\right)\ or\ APG_{i-6} > 1.1\ \left(hPa\ h^{-1}\right)\ i = 1, \ldots, 6 \quad (1)$$

then

$$H_{s\_new} = H_{s\_est} + a * \sum_{i=1}^{6} \frac{WMV_{i-6}}{6} + b * \sum_{l=1}^{6} \frac{APG_{i-6}}{6} \quad (2)$$

where *WMV* is the wind mean velocity, *APG* is the absolute value of pressure gradient, *i* indicates the sample number (e.g., *i*=0 corresponds to the current time; *i*=-5 corresponds to the data measured five hours before), and H_{s_est} and H_{s_new} are the H_s estimated by the procedure of Ferretti et al. [15] before and after the correction, respectively.

Figure 9 compares H_s measured by the buoy (blue line) and those provided by the procedure of Ferretti et al. [15] before (red line) and after (green line) the application of the proposed correction term for the Adrian storm. The differences between the H_s values measured by Capo Mele buoy and those obtained by using the microseism-based procedure corrected are strongly reduced (old maximum difference 3.4 m, new maximum difference 1.2 m). Since the applicability conditions were not met for the other sea storms (during which *WMV* and *APG* stayed under the thresholds), the correction term was not applied. It is worth highlighting that the thresholds, guiding the use of the correction term, were defined based on statistical analysis. Specifically, the thresholds of wind velocity and pressure gradient corresponds to the 95th percentile of data distributions. Among all storms that have occurred in Liguria since 2008, the Adrian storm is the only one that presents both wind velocity and pressure gradient values that exceed the thresholds chosen. However, it is worth noting that the data scarcity does not allow us to effectively verify the robustness of such criterion for differentiating storms, and if the wrong application of such a correction term to storms that generate high-energy microseism could generate significant errors in the estimation of H_s.

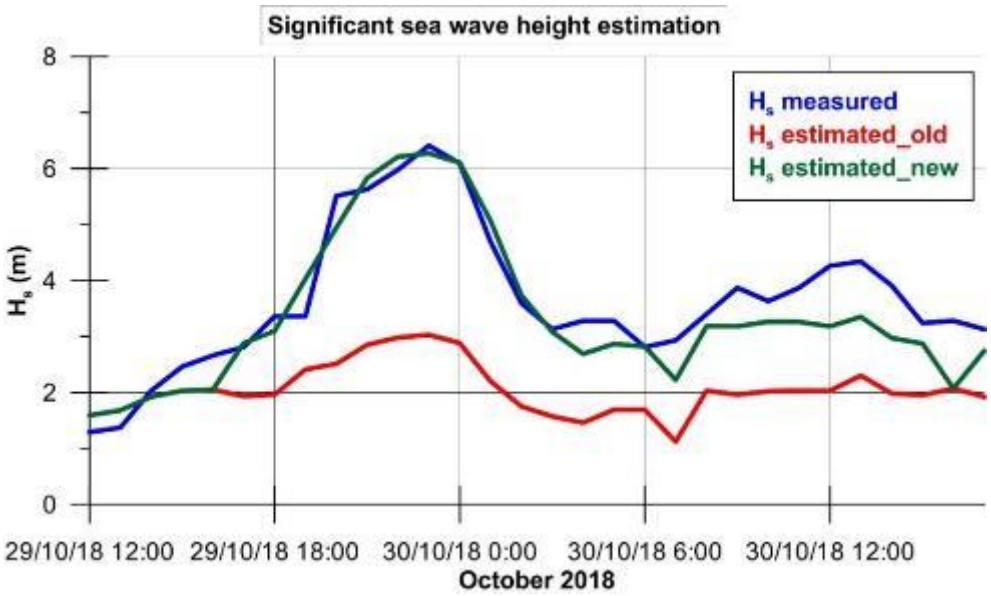

Figure 9. Comparison between H_s measured by the buoy (blue line) and those provided by model of Ferretti et al. [15] before (red line) and after (green line) the application of the correction term.

6. Conclusions

In the present study, we compared the characteristics of five of the most significant sea storms that struck the Ligurian coast between 2008 and 2018. Specifically, we analysed both sea wave and atmospheric parameters, and presented a spectral analysis of the storm-related microseisms. The aim was to highlight the distinctive features of the exceptional event occurred on October

2018 (Adrian storm) with respect to other strong sea storms in the same area in order to make (also during exceptional storms) the procedure proposed by Ferretti et al. [15] more effective for monitoring the sea wave height. In fact, although the Adrian storm caused sea wave heights up to 9 m and significant damage to coastal infrastructures, it generated a very low energy microseism, thus leading to a severe underestimation of the H_s values assessed through the procedure proposed by Ferretti et al. [15]. Therefore, a correction term, that takes into account wind velocity and the atmospheric pressure gradient, was proposed and applied to the predictive model, allowing a significantly reduction in the underestimation of the estimated H_s when dealing with storms that generate low energy microseisms (such as the Adrian storm). In our case, the wind velocity and pressure data were provided by the weather station of the Seismic and Meteorological Observatory of Imperia and, therefore, the applicability of the proposed correction term is limited to the area around Imperia and Capo Mele buoy (Figure 1). For the Adrian storm, the inclusion of meteorological data (wind velocities and pressure gradients above an empirically determined threshold) together with the microseism amplitude in the prediction of significant wave height resulted in a significantly better fit. Whether this or a similar formula, although promising, is applicable in general must be validated by a larger dataset. It will also be necessary to monitor if the H_s estimation is realistic during other events similar to the Adrian storm, even in presence of different storm characteristics.

References

1. Devis-Morales, A.; Montoya-Sánchez, R.A.; Bernal, G.; Osorio, A.F. Assessment of extreme wind and waves in the Colombian Caribbean Sea for offshore applications. Appl. Ocean Res. **2017**, 69, 10–26.
2. Ardhuin, F.; Stopa, J.E.; Chapron, B.; Collard, F.; Husson, R.; Jensen, R.E.; Johannessen, J.; Mouche, A.; Passaro, M.; Quartly, G.D.; et al. Observing Sea States. Front. Mar. Sci. **2019**, 6, 124.
3. Mentaschi, L.; Besio, G.; Cassola, F.; Mazzino, A. Performance evaluation of Wavewatch III in the Mediterranean Sea. Ocean Model. **2015**, 90, 82–94.
4. O'Reilly,W.C.; Olfe, C.B.; Thomas, J.; Seymour, R.J.; Guza, R.T. The California coastal wave monitoring and prediction system. Coast. Eng. **2016**, 116, 118–132.
5. He, Y.; Shen, H.; Perrie, W. Remote Sensing of Ocean Waves by Polarimetric SAR. J. Atmos. Ocean. Tech. **2006**, 23, 1768–1773.
6. Yaakob, O.; Zainudin, N.; Samian, Y.; Maimun, A.; Malik, A.; Palaraman, R.A. Presentation and validation of remote sensing ocean wave data. IJRRAS **2010**, 4, 373–379.
7. Reale, F.; Dentale, F.; Pugliese Carratelli, E.; Fenoglio-Marc, L. Influence of sea state on sea surface height oscillation from Doppler altimeter measurements in the North Sea. Remote Sens. **2018**, 10, 1100.
8. Ludeno, G.; Reale, F.; Raffa, F.; Centale, F.; Soldovieri, F.; Pugliese Carratelli, E.; Serafino, F. Integration between X-band radar and buoy sea state monitoring. Ocean Coast. Discuss. **2016**, 1–16.
9. Cui, J.; Bachmayer, R.; de Young, B.; Huang, W. Ocean wave measurement using short-range K-band narrow beam continuous wave radar. Remote Sens. **2018**, 10, 1242.
10. Bromirski, P.D.; Duennebier, F.K.; Stephen, R.A. Mid-ocean microseisms. Geochem. Geophy. Geosy. **2005**, 6.
11. Stutzmann, E.; Schimmel, M.; Patau, G.; Maggi, A. Global climate imprint on seismic noise. Geochem. Geophy. Geosy. **2009**, 101.
12. Ardhuin, F.; Gualtieri, L.; Stutzmann, E. How ocean waves rock the Earth: Two mechanisms explain microseisms with periods 3–300s. J. Geophys. Res. **2015**, 42, 765–772.
13. Ferretti, G.; Zunino, A.; Scafidi, D.; Barani, S.; Spallarossa, D. On microseisms recorded near the Ligurian coast (Italy) and their relationship with sea wave height. Geophys. J. Int. **2013**, 194, 524–533.
14. Ferretti, G.; Scafidi, D.; Cutroneo, L.; Gallino, S.; Capello, M. Applicability of an empirical law to predict significant sea-wave heights from microseisms along the Western Ligurian Coast (Italy). Continent. Shelf Res. **2016**, 122, 36–42.
15. Ferretti, G.; Barani, S.; Scafidi, D.; Capello, M.; Cutroneo, L.; Vagge, G.; Besio, G. Near real-time monitoring of significant sea wave height through microseism recordings: An application in the Ligurian Sea (Italy). Ocean Coast. Manag. **2018**, 165, 185–194.

16. Ardhuin, F.; Stutzmann, E.; Schimmel, M.; Mangeney, A. Ocean wave sources of seismic noise. J. Geophys. Res. **2011**, 116, C09004.
17. Davy, C.; Barruol, G.; Fontaine, F.R.; Sigloch, K.; Stutzmann, E. Tracking major storms from microseismic and hydroacoustic observations on the seafloor. Geophys. Res. Lett. **2014**, 41, 8825–8831.
18. Donne, S.; Nicolau, M.; Bean, C.; O'Neil, M. Wave Height Quantification Using Land Based Seismic Data with Grammatical Evolution. 2014. Available online: http://ncra.ucd.ie/papers/cec2014_waves.pdf (accessed on 11 March 2021).
19. University of Genoa. Regional Seismic Network of North-Western Italy; Other/Seismic Network; International Federation of Digital Seismograph Networks: Seattle, DC, USA, 1967.
20. Mentaschi, L.; Besio, G.; Cassola, F.; Mazzino, A. Implementation and validation of a wave hindcast/forecast model for the west Mediterranean. J. Coast. Res. **2013**, 65, 1551–1556.
21. Chi, W.C.; Chen, W.J.; Kuo, B.Y.; Dolenc, D. Seismic monitoring of western Pacific typhoons. Mar. Geophys. Res. **2010**, 31, 239–251.
22. Chen, X.; Tian, D.; Wen, L. Microseismic sources during Hurricane Sandy. J. Geophys. Res. Solid Earth **2015**, 120, 6386–6403.
23. Davy, C.; Barruol, G.; Fontaine, F.R.; Cordier, E. Analyses of extreme swell events on La Réunion Island from microseismic noise. Geophys. J. Int. Oxf. Univ. Press (OUP) **2016**, 207, 1767–1782.
24. Lin, J.; Lin, J.; Xu, M. Microseisms generated by super typhoon Megi in the western Pacific Ocean. J. Geophys. Res. Oceans **2017**, 122.
25. Butler, R.; Aucan, J. Multisensor, microseismic observations of a hurricane transit near the ALOHA Cabled Observatory. J. Geophys. Res. Solid Earth **2018**, 123, 3027–3046.
26. Xiao, H.; Xue, M.; Yang, T.; Liu, C.; Hua, Q.; Xia, S.; Huang, H.; Manh Le, B.; Yu, Y.; Huo, D.; et al. The characteristics of microseisms in South China Sea: Results from a combined data set of OBSs, broadband land seismic stations, and a global wave height model. J. Geophys. Res. Solid Earth **2018**, 123, 3923–3942.
27. Pedemonte, L.; Corazza, M.; Forestieri, A.; Turato, B. Rapporto di Evento Meteorologico del 27-30/10/2018. Ligurian Environmental Protection Agency—Weather-Hydrological Functional Center of Civil Protection of the Liguria Region. 2019; p.16. Available online: https://www.arpal.gov.it/contenuti_statici//pubblicazioni/rapporti_eventi/2018/REM_20181027-30_rossaBCDE_vers20190107.pdf (accessed on 11 March 2021).
28. Casella, E.; Rovere, A.; Pedroncini, A.; Mucerino, L.; Casella, M.; Cusati, L.A.; Vacchi, M.; Ferrari, M.; Firpo, M. Study of wave runup using numerical models and low-altitude aerial photogrammetry: A tool for coastal management. Estuar. Coast. Shelf Sci. **2014**, 149, 160–167.
29. Decreto del Commissario Delegato n. 2/2019. Eccezionali Eventi Meteorologici che Hanno Interessato il Territorio Della Regione Liguria nei Giorni 29 e 30 Ottobre 2018—OCDPC n.558/2018. Approvazione Elenco Comuni Danneggiati. Available online: https://www.regione.liguria.it/components/com_publiccompetitions/includes/download.php?id=32935:cdc-558-2-2019.pdf (accessed on 18 January 2021).
30. Corradi, N.; Zaquini, M.; Ferretti, O. Interpretazione Sismostratigrafica Della Piattaforma Costiera Antistante la Foce Dell'Entella. ENEA "Il Golfo del Tigullio—Liguria Orientale. Avanzamento Degli Studi per la Creazione di Strumenti Della Gestione Costiera". 2003. Available online: http://www.santateresa.enea.it/wwwste/dincost/dincost_pdf/7sismica.pdf (accessed on 11 March 2021).
31. Capello, M.; Cutroneo, L.; Ferretti, G.; Gallino, S.; Canepa, G. Changes in the physical characteristics of the water column at the mouth of a torrent during an extreme rainfall event. J. Hydrol. **2016**, 541, 146–157.
32. De Leo, F.; Solari, S.; Besio, G. Extreme waves analysis based on atmospheric patterns classification: An application along the Italian coast. Nat. Hazards Earth Syst. Sci. Discuss. **2020**, 20, 1233–1246.
33. Lionello, P.; Abrantes, F.; Congedi, L.; Dulac, F.; Gacic, M.; Gomis, D.; Goodess, C.; Hoff, H.; Kutiel, H.; Luterbacher, J.; et al. Introduction: Mediterranean climate—Background information. In The Climate of the Mediterranean Region; Lionello, P., Ed.; Elsevier: Oxford, UK, 2012.
34. Pensieri, S.; Bozzano, R.; Schiano, M.E. Comparison between QuikSCAT and buoy wind data in the Ligurian Sea. J. Marine Syst. **2010**, 81, 286–296.
35. Sartini, L.; Cassola, F.; Besio, G. Extreme waves seasonality analysis: An application in the Mediterranean Sea. J. Geophys. Res. Oceans **2015**, 120, 6266–6288.

36. Gallino, S.; Benedetti, A.; Onorato, L.Wave watching. In Lo Spettacolo Delle Mareggiate in Liguria; Hoepli: Milano, Italy, 2016; p. 182.
37. Orlandi, A.; Pasi, F.; Onorato, L.f.; Gallino, S. An observation and numerical case study of a flash sea storm over the Gulf of Genoa. Adv. Sci. Res. **2008**, 2, 107–112.
38. Cavaleri, L.; Bajo, M.; Barbariol, F.; Bastianini, M.; Benetazzo, A.; Chiggiato, J.; Davolio, S.; Ferrarin, C.; Magnusson, L.; Papa, A.; et al. The October 29, 2018 storm in Northern Italy—An exceptional event and its modeling. Prog. Oceanogr. **2019**, 178, 102–178.
39. Celano, M.; Costa, S.; Foraci, R. Rapporto dell'evento meteorologico dal 27 al 30 ottobre 2018. Servizio Idro-Meteo-Clima. 2018, p.49. Available online: https://allertameteo.regione.emilia-romagna.it/documents/20181/437770/Evento+27-30+ottobre+2018/ab59ec27-27c2-4793-b6f9-b0a91ceef30e (accessed on 11 March 2021).
40. Erofeeva, S.; Padman, L.; Howard, S.L. Tide Model Driver (TMD) Version 2.5, Toolbox for Matlab, GitHub. Available online: https://www.github.com/EarthAndSpaceResearch/TMD_Matlab_Toolbox_v2.5 (accessed on 18 January 2020).
41. Feng, X.; Olabarrieta, M.; Valle-Levinson, A. Storm-induced semidiurnal perturbations to surges on the US Eastern Seaboard. Cont. Shelf Res. **2016**, 114, 54–71.
42. Zuur, A.F.; Ieno, E.N.; Smith, G.M. Analysing Ecological Data; Springer: New York, NY, USA, 2007.
43. Cutroneo, L.; Castellano, M.; Carbone, C.; Consani, S.; Gaino, F.; Tucci, S.; Magrì, S.; Povero, P.; Bertolotto, R.M.; Canepa, G.; et al. Evaluation of the boundary condition influence on PAH concentrations in the water column during the sediment dredging of a port. Mar. Pollut. Bull. **2015**, 101, 583–593.
44. Vousdoukas, M.I.; Voukouvalas, E.; Annunziato, A.; Giardino, A.; Feyen, L. Projections of extreme storm surge levels along Europe. Clim. Dyn. **2016**, 47, 3171–3190.
45. Ullmann, A.; Pirazzoli, P.A. Recent evolution of extreme sea surge-related meteorological conditions and assessment of coastal flooding risk on the gulf of Lions. Méditerranée **2007**, 108, 69–76.
46. Pasi, F.; Orlandi, A.; Onorato, L.F.; Gallino, S. A study of the 1 and 2 January 2010 sea-storm in the Ligurian Sea. Adv. Sci. Res. **2011**, 6, 109–115. Available online: www.adv-sci-res.net/6/109/2011/ (accessed on 1 February 2021).
47. Bromirski, P.D.; Flick, R.E.; Graham, N. Ocean wave height determined from inland seismometer data: Implications for investigating wave climate changes in the NE Pacific. J. Geophys. Res. **1999**, 104, 20753–20766.
48. Traer, J.; Gerstoft, P.; Bromirski, P.D.; Shearer, P.M. Microseisms and hum from ocean surface gravity waves. J. Geophis. Res. **2012**, 117, B11307.
49. Ardhuin, F.; Balanche, A.; Stutzmann, E.; Obrebski, M. From seismic noise to ocean wave parameters: General methods and validation. J. Geophys. Res. **2012**, 117, C05002.

8 Verification of reliability of the H_s estimation model

8.1 Introduction

Given the significant H_s underestimation due to the lack of microseism energy peak occurred during the Adrian Storm in October 2018, it was decided to monitor the reliability of the estimation model defined in Ferretti et al. (2018) over the long term by defining the magnitude of the difference between the H_s resulting from the microseism and H_s generated by simulation (hindcast) and measured by the wave buoy of Capo Mele. This was intended to highlight any other differences between the measured and estimated H_s or criticalities in the reliability of the estimation model, in addition to those highlighted during the Adrian Storm.

As the buoy stopped working in November 2019 and has not been restored, and as the buoy represents a measurement point along the western coast of Liguria and therefore does not return representative sea state data for the rest of the region, the reference taken into account is represented by the hindcast data. Therefore, a data analysis was prepared to provide the quantification of the differences between the H_s derived from the hindcasts developed by DICCA (H_s(hindcast)) and the H_s derived from the model applied to microseisms (H_s(μseism)) considering the node 319 corresponding to the western part of the Ligurian coast near Imperia (Fig. 6.1). Moreover, since the model by Ferretti et al. (2018) was calibrated from hindcast data, it was chosen to carry out the monitoring firstly using hindcast data. The first analysis was applied to the period between August 2018 and November 2019. Subsequently, the comparison was also made between the H_s measured by the wave buoy of Capo Mele (H_s(buoy)) and H_s(μseism) considering the node 391 corresponding to the buoy to check for any criticalities with respect to the data measured at sea.

8.2 Materials and methods

The following steps were identified for monitoring the reliability and effectiveness of the mathematical procedure applied to microseisms.

Phase I: H_s(μseism) vs. H_s(hindcast) - node 319, 31/08/2018-02/11/2019 period

a) Comparison between the H_s(hindcast) and the H_s(μseism) and calculation of the difference between the two (ΔH_s):

- LinePlot(Date, H_s(hindcast) & H_s(μseism))
- $\Delta H_s = H_s$(hindcast) - H_s(μseism)
- DotPlot(Date, ΔH_s)

b) Considering the absolute value of ΔH_s (ΔH_sAbs) to highlight the range of variation.

c) Comparison between magnitude of the ΔH_s and H_s(hindcast) and H_s(μseism) to verify if the deviation increases in cases of higher H_s or if it is independent of H_s:

- DotPlot(H_s(μseism), ΔH_s) and DotPlot(H_s(hindcast), ΔH_s)

d) Removal the Adrian Storm from the dataset and repetition of point c); identification of sea storm with significant ΔH_s (>1.50 m) and analyse their characteristics.

e) Control on other nodes in the Ligurian Sea considered by Ferretti et al. (2018)(i.e., nodes 206, 264, 332, 427; Fig. 6.1).

Phase II: H_s(buoy) vs. H_s(μseism) - node 391, 31/08/2018-02/11/2019 period

Steps from a) to d) equal to Phase I, but comparing the H_s(buoy) to the H_s(μseism), and H_s(hindcast) to the H_s(μseism).

Phase III: Proposal of amendment to the mathematical procedure

A) Two tests were carried out considering the node 319 in the 2013-2014 period (the same period considered by Ferretti et al., 2018), and all the seismic stations of Ferretti et al. (2018)(i.e. GBOS, IMI0, QLNO, RORO, GORR, MSSA, PLMA; Fig. 6.1), with the exception of station NEGI in the western part of Liguria, that, meanwhile, has been removed from the seismic network.

- test 1: fixing of the integration intervals of the model, f_{min} and f_{max}, to 0.2 Hz and 0.9 Hz, respectively, and definition of new coefficients *a* and *b* for all the estimation model, i.e. base, 1.0 m, 1.5, 2.0 m and 3.0 m.

- test 2: same modifications of test 1 plus the modification of the procedure for the higher H_s considering in each step the mean value of H_s + 2 standard deviations. This amendment favours the evaluation of high H_s and allows more frequent use of steps calibrated to higher wave heights (H_s>1.0 m, H_s>1.5 m, H_s>2.0 m and H_s>3.0 m).

B) Launch of the modified procedure using the same data considered by Ferretti et al (2018) between 2013 and 2014.

C) Comparison between the new H_s(μseism) with the reference H_s(hindcast) for verifying new residuals and the presence of any new H_s underestimations in the node 319 on the 2013-2014 period.

D) Verification of the modified procedure with test 2 only for the node 319 on the 2018-2019 dataset.

E) Repetition of steps from A to C considering only test 2 in the node 391 on the 2013-2014 period for comparison between the new H_s(μseism) with the reference H_s(buoy) to verify new residuals and the presence of any new H_s underestimations.

8.3 Results and discussion

Phase I: H_s(μseism) vs. H_s(hindcast) - node 319, 31/08/2018-02/11/2019 period

Considering the $\Delta H_{s.319}$ deviation, the average was 0.09 m ± 0.32 m, with a minimum of -1.92 m and a maximum of 3.10 m occurred during the Adrian Storm. Only a minimal part of the data exceeds 1 m of ΔH_s. The profiles of the H_s(hindcast) and H_s(μseism) and the profile of the ΔH_s deviation are shown in Fig. 8.1 and Fig. 8.2. Generally, the profiles of the two heights overlap but there is a general underestimation of H_s(μseism) with respect to H_s(hindcast). The underestimation of H_s by the microseism is present in only 4 cases; from the analysis of the specific data three of these are defined as spikes in microseism data and deleted from the dataset, while one was a real data and related to the Adrian Storm.

Considering the absolute value of ΔH_s (ΔH_sAbs), most of the data falls within the range 0.00-0.49 m (89%) and the 10% in the range 0.50-0.99 m (Table 8.1).

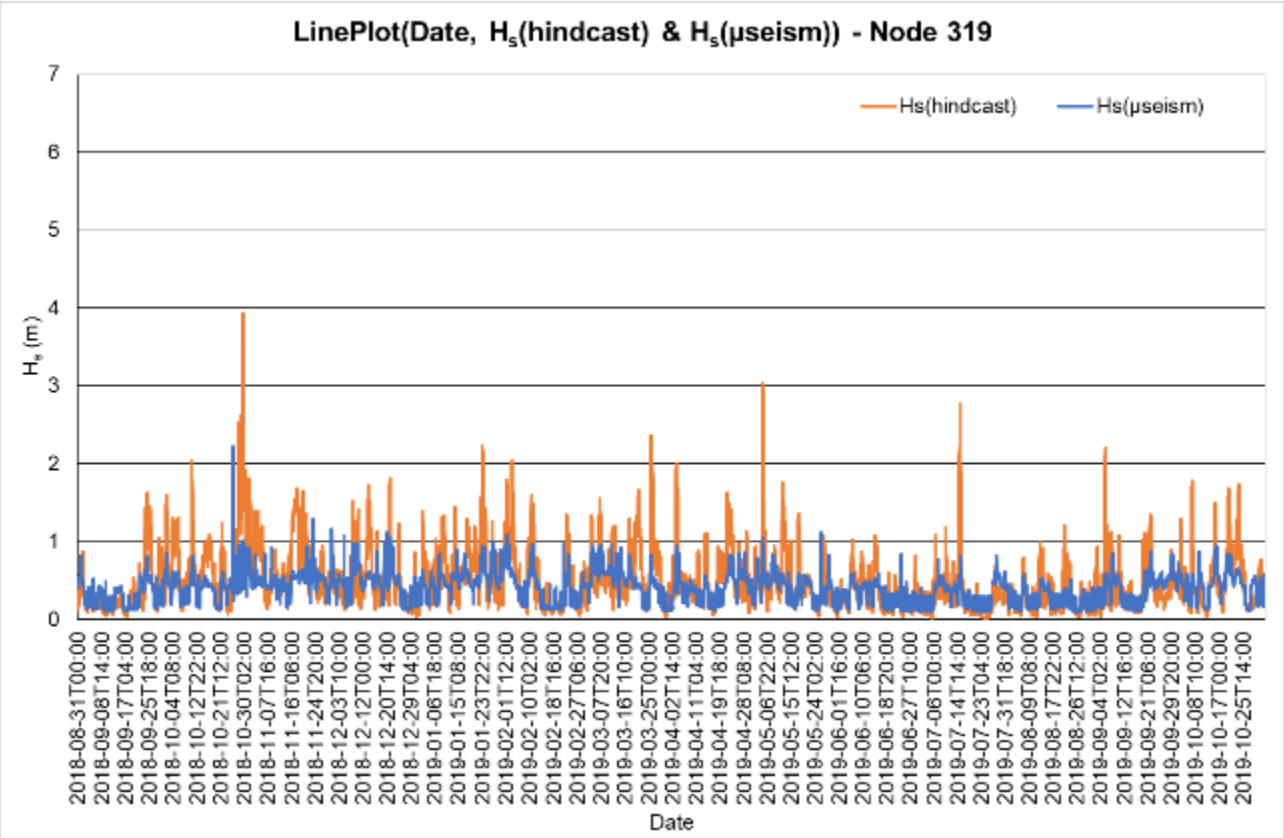

Fig. 8.1. Temporal distribution of H_s(hindcast) and H_s(µseism).

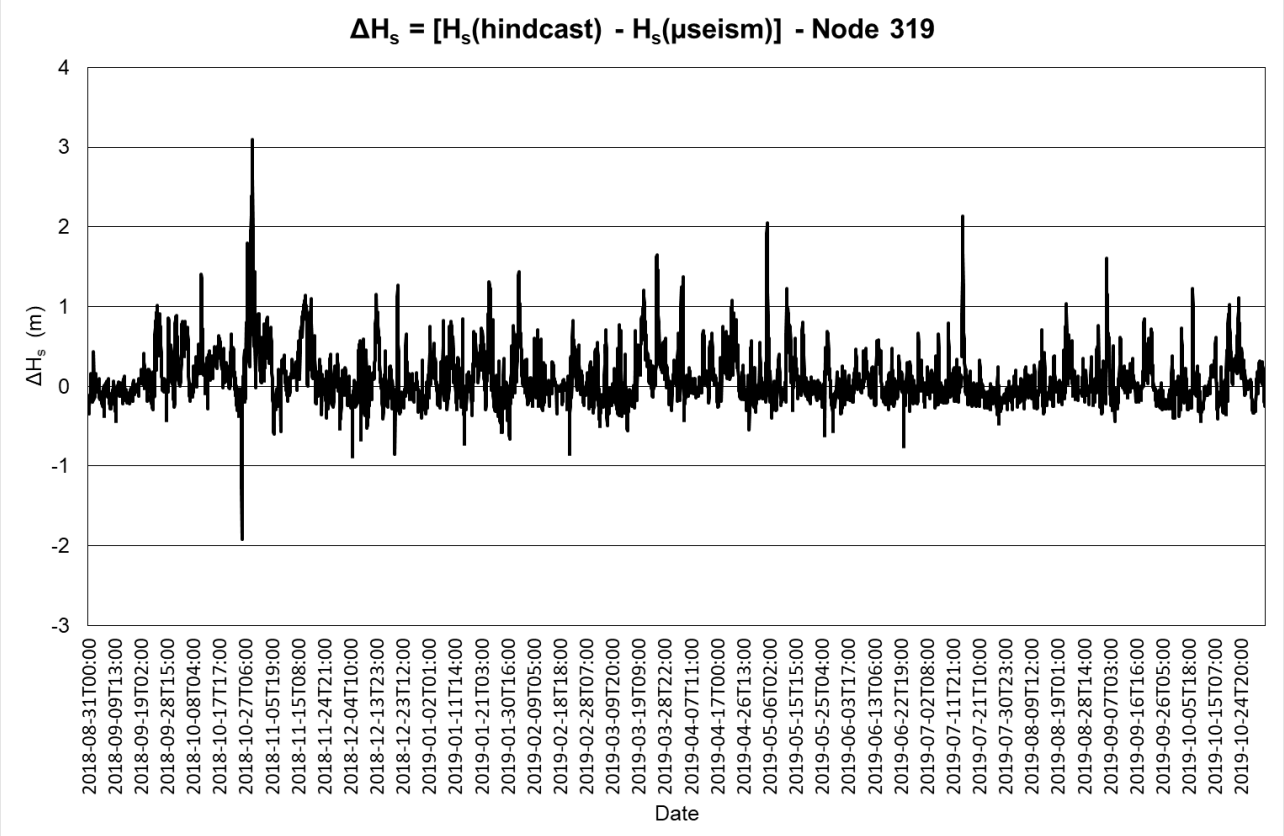

Fig. 8.2. Temporal distribution of ΔH_s between H_s(hindcast) and H_s(µseism).

Table 8.1. Number and percentage of cases that fall in the different ΔH_sAbs ranges.

ΔH_sAbs range (m)	**Case number**	**Percentage**
0.00	186	1.81
0.01-0.49	8927	87.06
0.50-0.99	972	9.48
1.00-1.99	152	1.48
>2.00	17	0.17
Total	10254	100.00

The relationship between H_s(hindcast) and H_s(μseism) is very week (R^2=0.3715; Fig. 8.3-top). By relating the H_s(μseism) to the ΔH_s deviation, there is no relationship (Fig. 8.3-middle); on the contrary, relating the H_s(hindcast) to the ΔH_s deviation (Fig. 8.3-bottom), there is a linear relationship between the two factors (R^2=0.7507), so as the H_s(hindcast) increases, the ΔH_s generally increases as well. This therefore highlights a first criticality in the reliability of the procedure of Ferretti et al. (2018), which returns a good H_s value for wave heights generally <1 m, but which produces an increasing underestimation with wave heights >1 m. This may be due to the method used to calibrate the H_s evaluation system from the microseism, a method that was based on a relatively small dataset (from 1 January 2013 to 1 June 2014; Ferretti et al., 2018) and that included very few sea storm characterised by H_s>2 m.

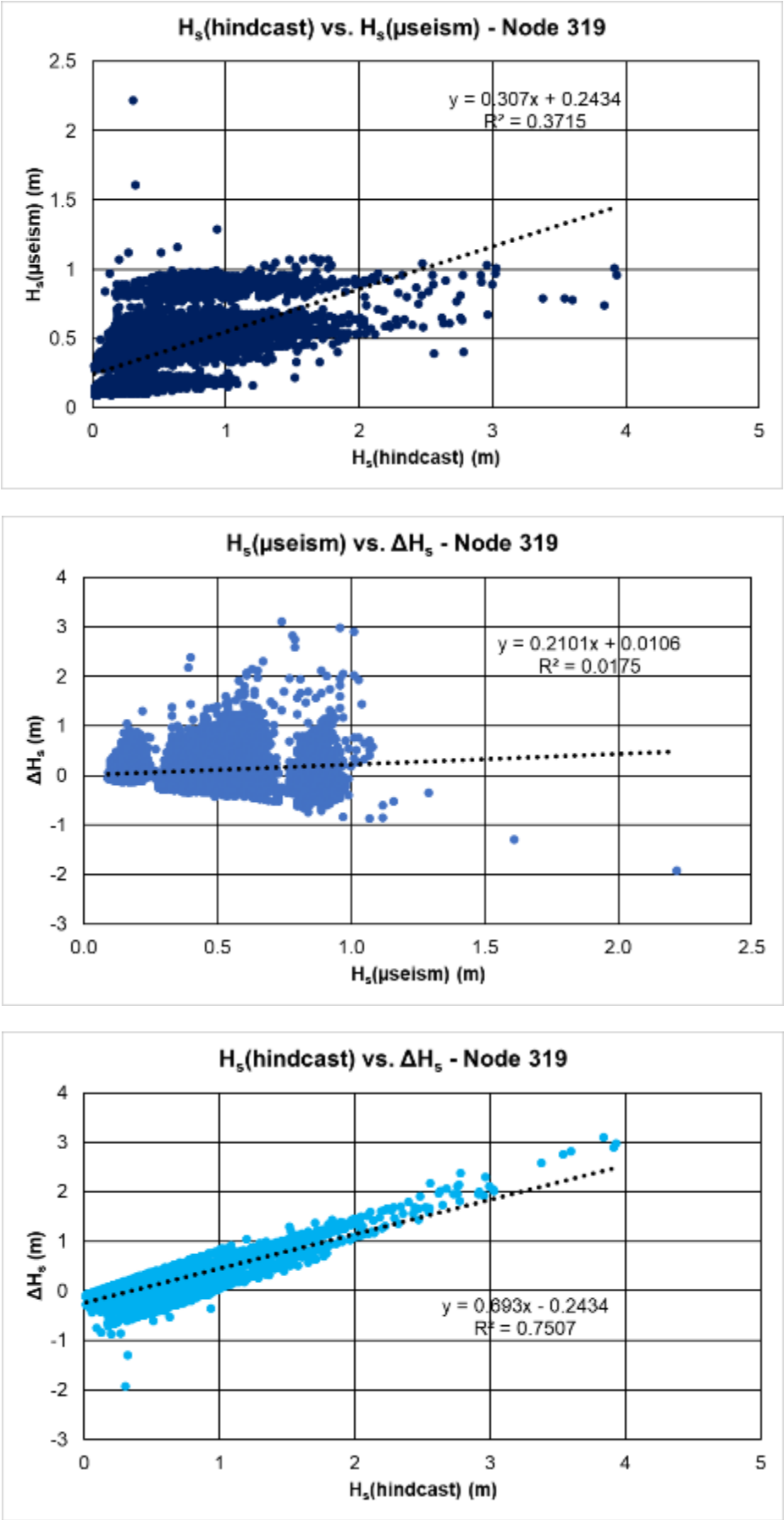

Fig. 8.3. Scatter plots between H_s(hindcast) and H_s(μseism) (top), H_s(μseism) and ΔH_s (middle), and H_s(hindcast) and ΔH_s (bottom).

Not considering the Adrian Storm in the dataset, i.e. removing the period between 00:00 on 28/10/2018 and 23:00 on 30/10/2018, the mean deviation drops to 0.09 m ± 0.30 m, with a range between -1.92 and 2.14 m. The positive relationship between H_s(hindcast) and ΔH_s remains (R^2=0.7236; Fig. 8.4-bottom) and highlights that with sea storms with H_s>2 m the model significantly underestimates H_s.

Table 8.2. Number and percentage of cases that fall in the different ΔH_sAbs ranges without the Adrian Storm.

ΔH_sAbs range (m)	**Number without the Adrian Storm**	**Percentage without the Adrian Storm**
0.00	186	1.83
0.01-0.49	8918	87.58
0.50-0.99	941	9.24
1.00-1.99	133	1.31
>2.00	5	0.05
Total	10183	100.00

Disregarding the Adrian Storm allowed us to identify other sea storms that produced a significant ΔH_s (>1.50 m) and therefore a significant underestimation of the H_s, namely the swells of 07-09/12/2018, 01-02/02/2019, and 27/01/2019, and analyse them to look for possible similarities in characteristics with the Adrian Storm. These five swells had H_s greater than 2 m and mean SE propagation direction, whereas the Adrian Storm was characterised by a variable propagation direction from the southern quadrants, with SW direction during the peak. The fact that these sea storms had H_s>2 m reinforces the fact that the model was not structured appropriately for the most intense sea storms due to the small dataset considered for its calibration.

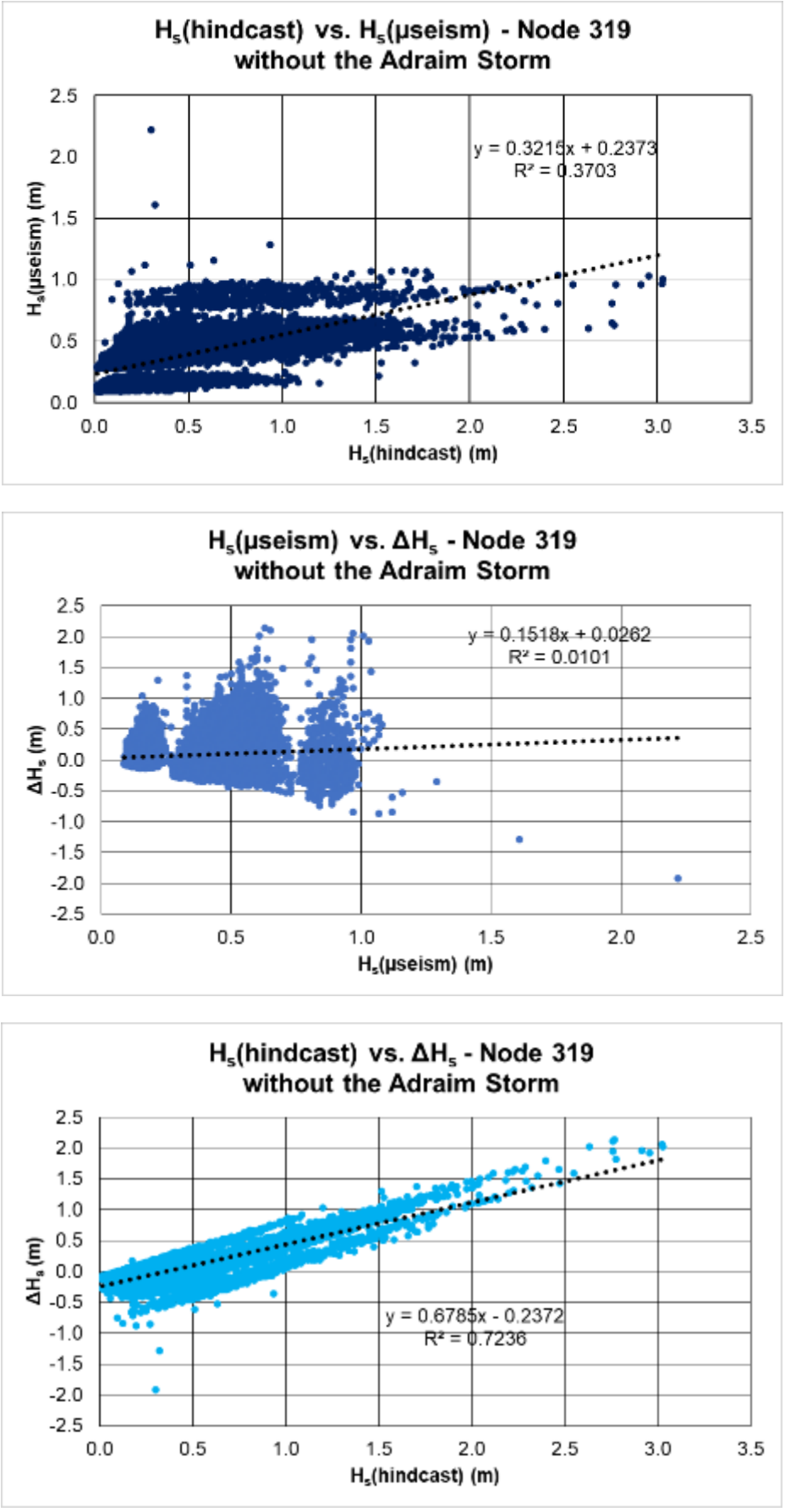

Fig. 8.4. Scatter plots between H_s(hindcast) and H_s(μseism) (top), H_s(μseism) and ΔH_s (middle), and H_s(hindcast) and ΔH_s (bottom) without data of the Adrian Storm.

The following Panel 1 is a comparison between H_s(μseism) and H_s(hindcast) for all the nodes considered by Ferretti et al. (2018). For convenience, the map in Fig. 6.1 is also shown here. The difference between the two curves is clearly higher at nodes 319 and 427 than at the others, and the better situation is in the central part of the Liguria (nodes 206 and 264). This can be due to the fact that western nodes, and especially node 427, are in the extreme western of the region and suffer different types of sea wave than the eastern part of the Liguria, and the seismic stations respond in different way.

Panel 2 shows the scatter plots between H_s(hindcast) and ΔH_s for all the nodes; it is possible to see the constant presence of the positive linear regression.

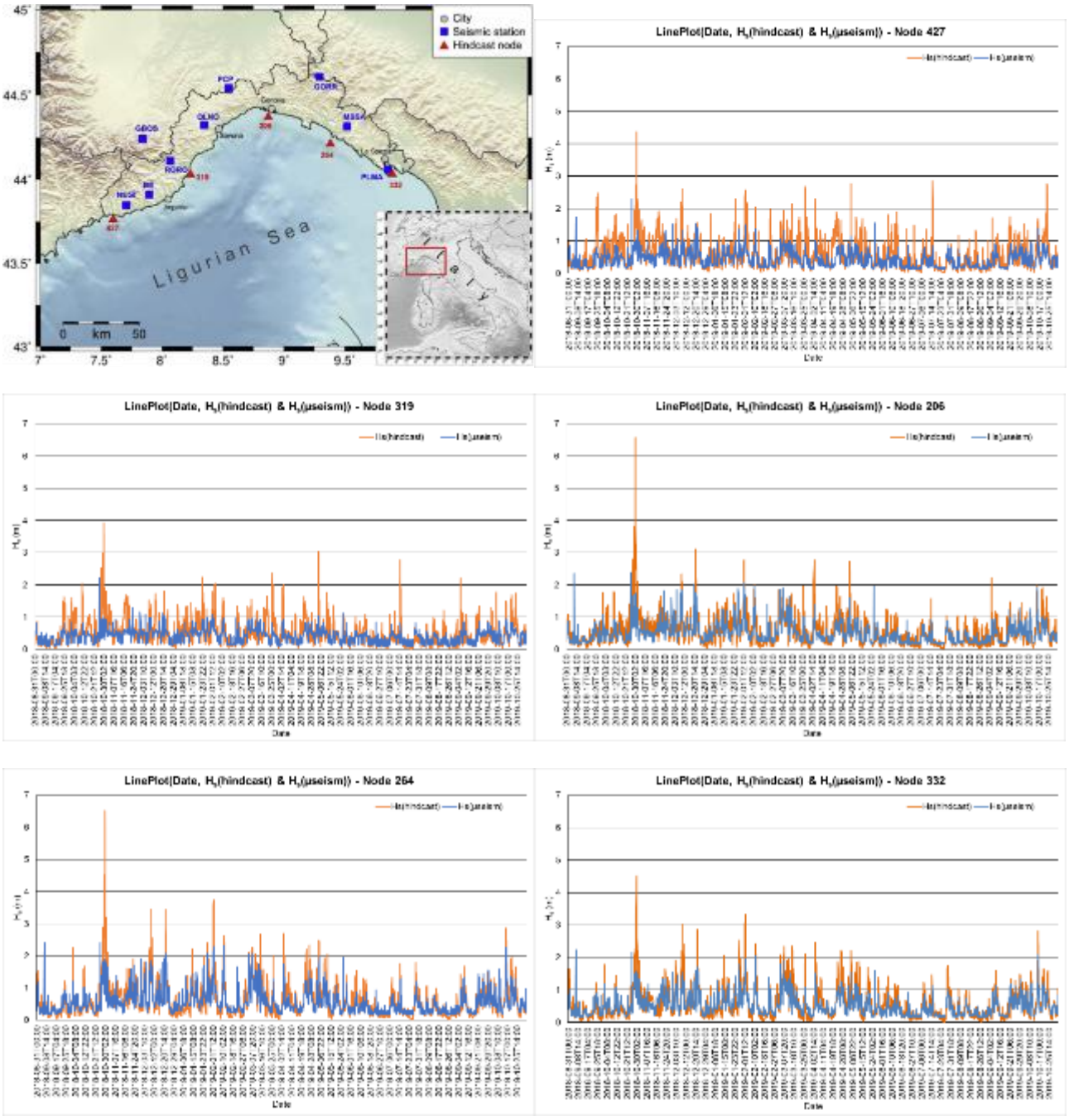

Panel 1. Comparison between H_s(μseism) and H_s(hindcast) for the nodes 427, 319, 206, 264 and 332 shown in the map on top.

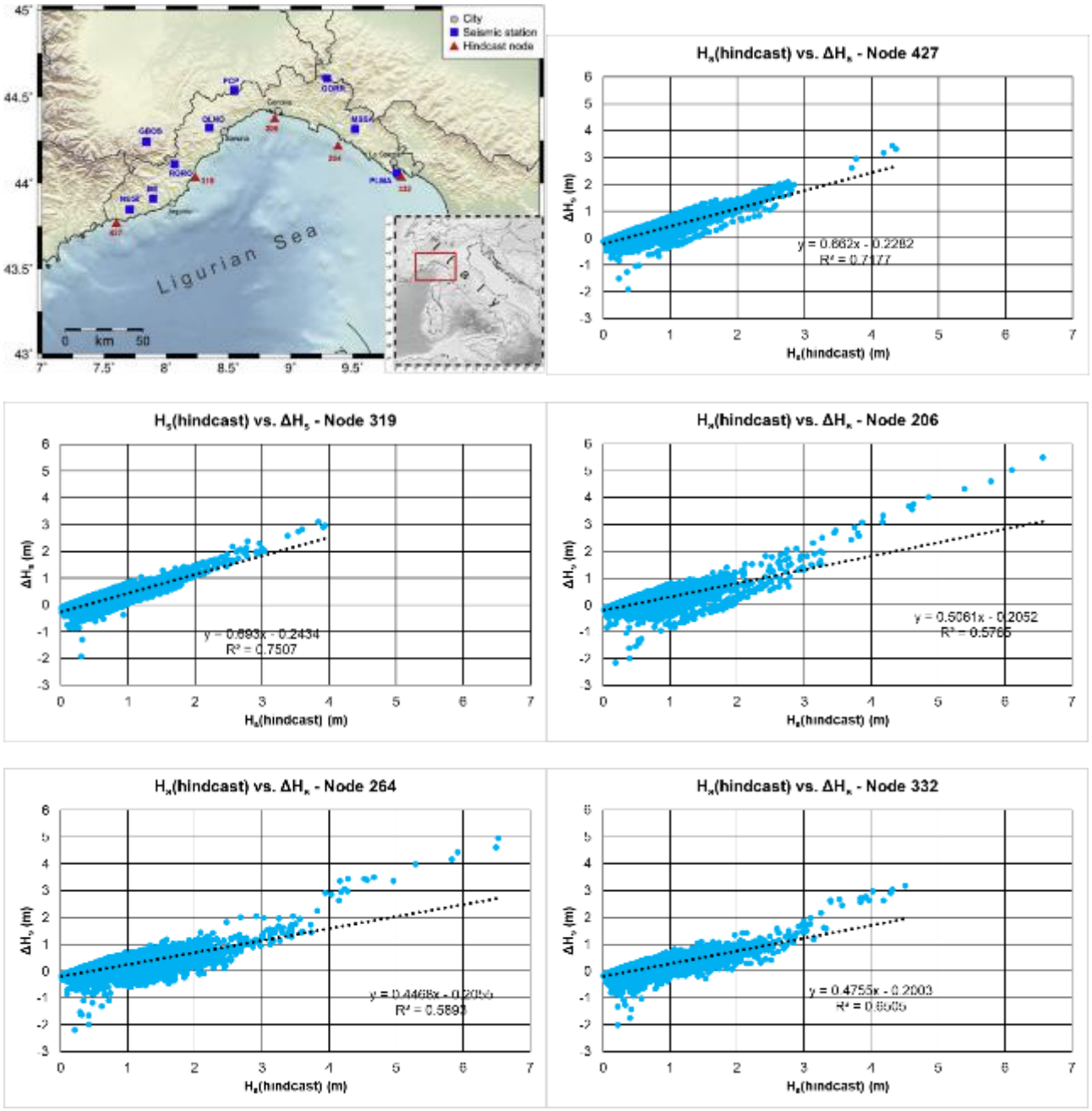

Panel 2. Scatter plots between H_s(hindcast) and ΔH_s for the nodes 427, 319, 206, 264 and 332 shown in the map on top.

Phase II: H_s(buoy) vs. H_s(μseism) - node 391, 31/08/2018-02/11/2019 period

Given the differences between H_s(μseism) and H_s(hindcast) on five nodes of Fig. 6.1, it was decided to also investigate the difference between H_s(μseism) and H_s(buoy), and also H_s(hindcast), considering the node 391 corresponding to the buoy position, over the same 31/08/2018-02/11/2019 period.

Starting from H_s(μseism) and H_s(buoy), the ΔH_s average is -0.04 m ± 0.30 m, with a minimum of -3.64 m and a maximum of 4.28 m during the Adrian Storm. Considering the absolute value of ΔH_s (ΔH_sAbs; Table 8.3), most of the data falls within the range 0.01-0.49 m (90%) and the 7% in the range 0.50-0.99 m. Only a minimal part of the data (<1%) exceeds 1 m of ΔH_s. The profiles of the H_s(buoy) and H_s(μseism), and the profile of the

ΔH_s deviation are shown below (Fig. 8.5 and Fig. 8.6). The overlap of the two curves is good and only two large underestimates of the H_s are noted, one at the Adrian Storm and one in December 2018.

Table 8.3. Number and percentage of cases that fall in the different ΔH_sAbs ranges.

ΔH_sAbs range (m)	**Case number**	**Percentage**
0.00	216	2.20
0.01-0.49	8853	90.34
0.50-0.99	6448	6.57
1.00-1.99	71	0.72
>2.00	16	0.16
Total	9800	100.00

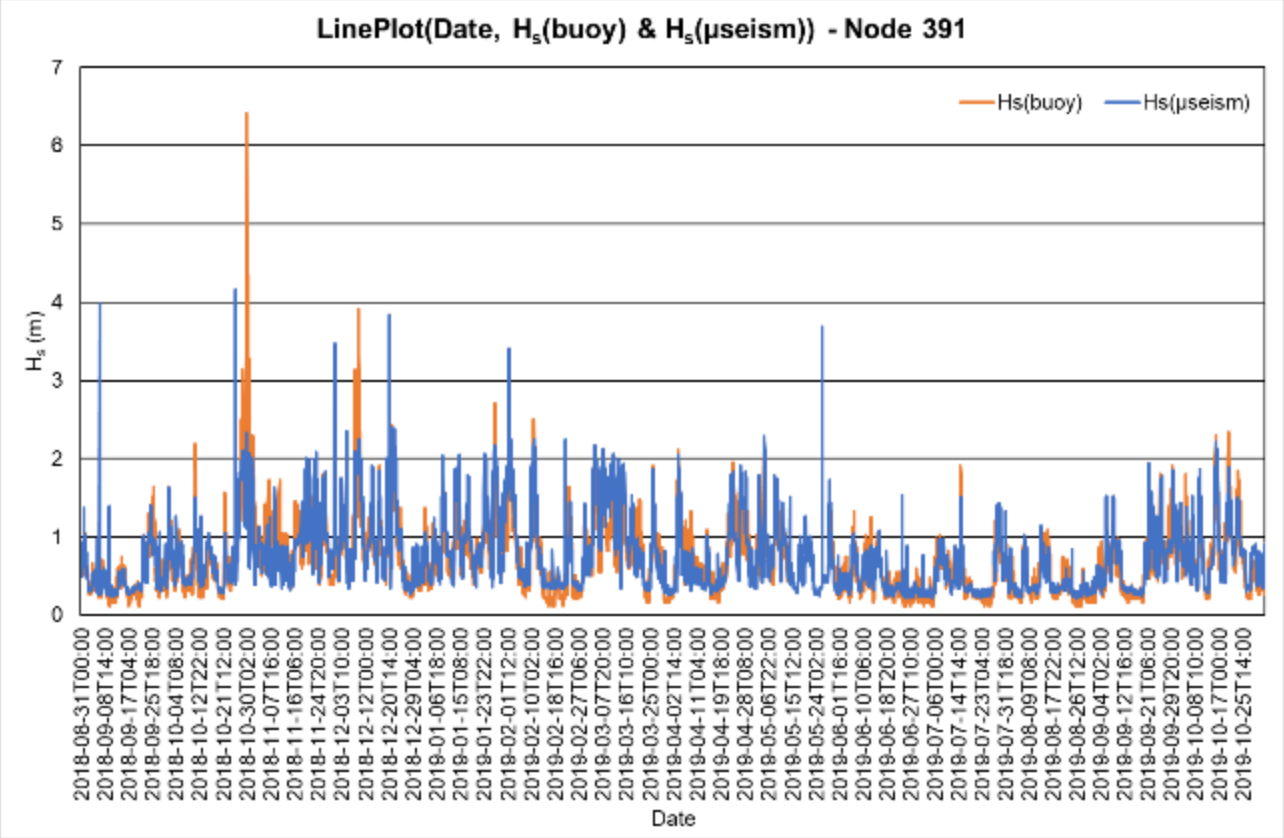

Fig. 8.5. Temporal distribution of H_s(buoy) and H_s(μseism).

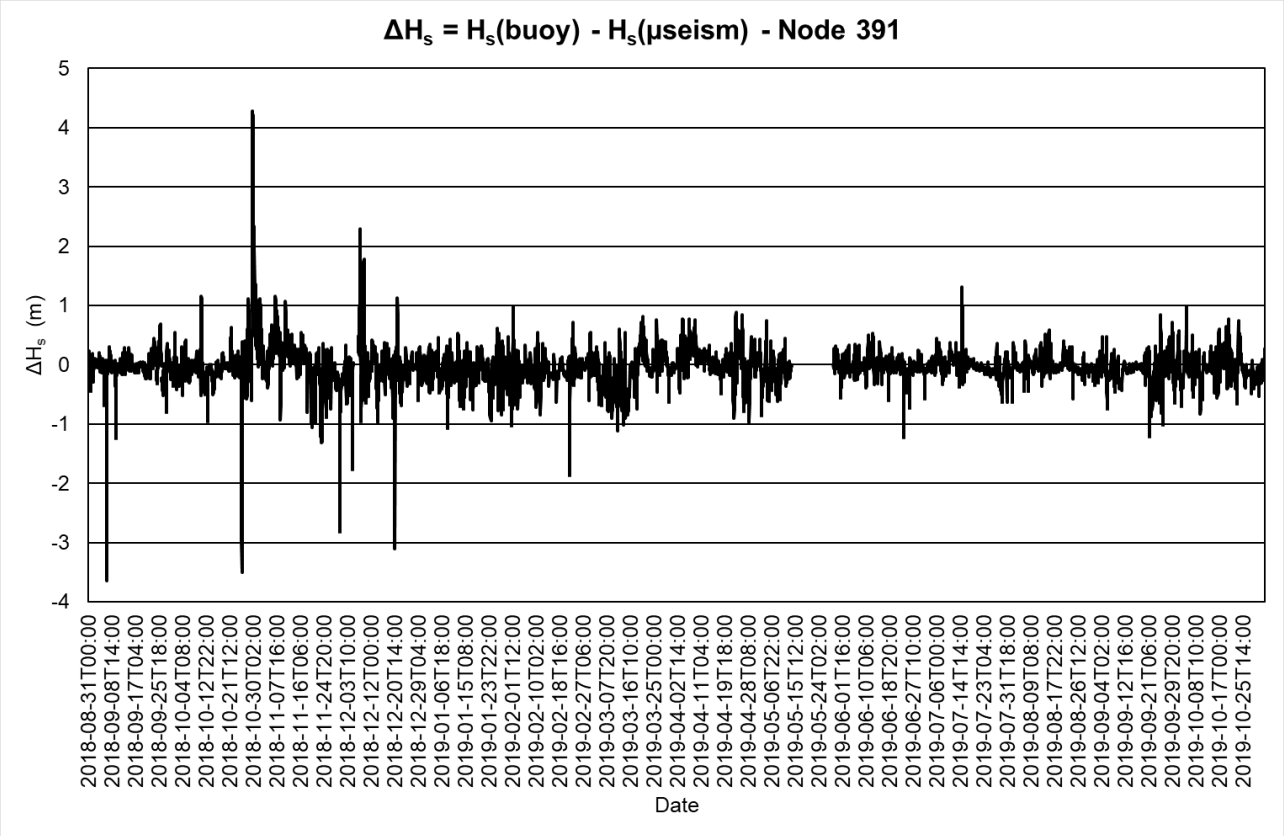

Fig. 8.6. Temporal distribution of ΔH_s between H_s(buoy) and H_s(μseism).

The relationship between H_s(buoy) and H_s(μseism) is low (R^2=0.6351; Fig. 8.7-top). By relating the H_s(μseism) to the ΔH_s deviation (Fig. 8.7-middle), and the H_s(buoy) to the ΔH_s (Fig. 8.7-bottom), there is no relationship.

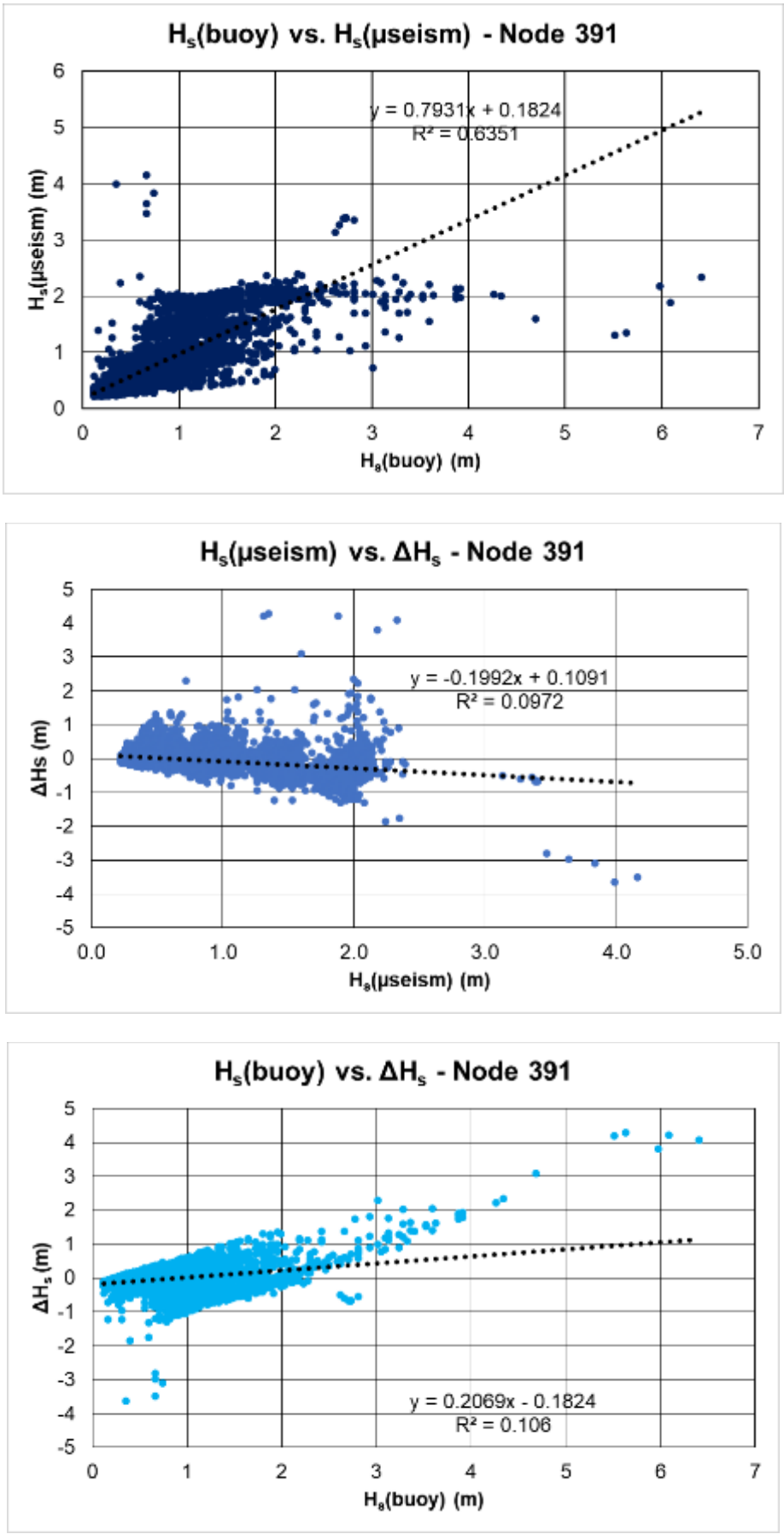

Fig. 8.7. Scatter plots between H_s(buoy) and H_s(μseism) (top), H_s(μseism) and ΔH_s (middle), and H_s(buoy) and ΔH_s (bottom).

Not considering the Adrian Storm in the dataset, i.e. removing the period between 00:00 on 28/10/2018 and 23:00 on 30/10/2018, the mean deviation drops to -0.05 m ± 0.27 m, with a range between -3.64 and 2.29 m (Table 8.4). The relationship between H_s(buoy) and ΔH_s remains very low (Fig. 8.8).

Table 8.4. Number and percentage of cases that fall in the different ΔH_sAbs ranges.

ΔH_sAbs range (m)	**Number without the Adrian Storm**	**Percentage without the Adrian Storm**
0.00	215	2.21
0.01-0.49	8825	90.71
0.50-0.99	632	6.50
1.00-1.99	51	0.52
>2.00	6	0.06
Total	9729	100.00

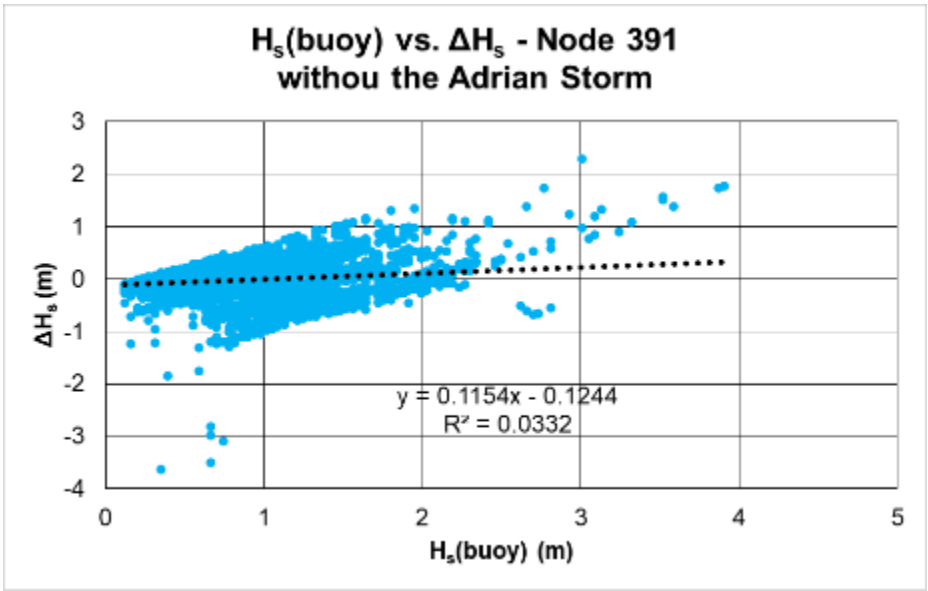

Fig. 8.8. Scatter plot between H_s(buoy) and ΔH_s without data of the Adrian Storm.

The same analysis was carried out with the hindcast data on the node 391 in the same period. The ΔH_s average is 0.16 m ± 0.38 m, with a minimum of -3.72 m and a maximum of 3.70 m during the Adrian Storm. Considering the absolute value of ΔH_s (ΔH_sAbs; Table 8.5), most of the data falls within the range 0.01-0.49 m (79%) and the 17% in the range 0.50-0.99 m. Only a minimal part of the data (<3%) exceeds 1 m of ΔH_s. The profiles of the H_s(hindcast) and H_s(μseism), and the profile of the ΔH_s deviation are shown below (Fig. 8.9 and Fig. 8.10).

Table 8.5. Number and percentage of cases that fall in the different ΔH_sAbs ranges.

ΔH_sAbs range (m)	**Case number**	**Percentage**
0.00	150	1.46
0.01-0.49	8100	78.99
0.50-0.99	1724	16.81
1.00-1.99	261	2.55
>2.00	20	0.20
Total	10255	100.00

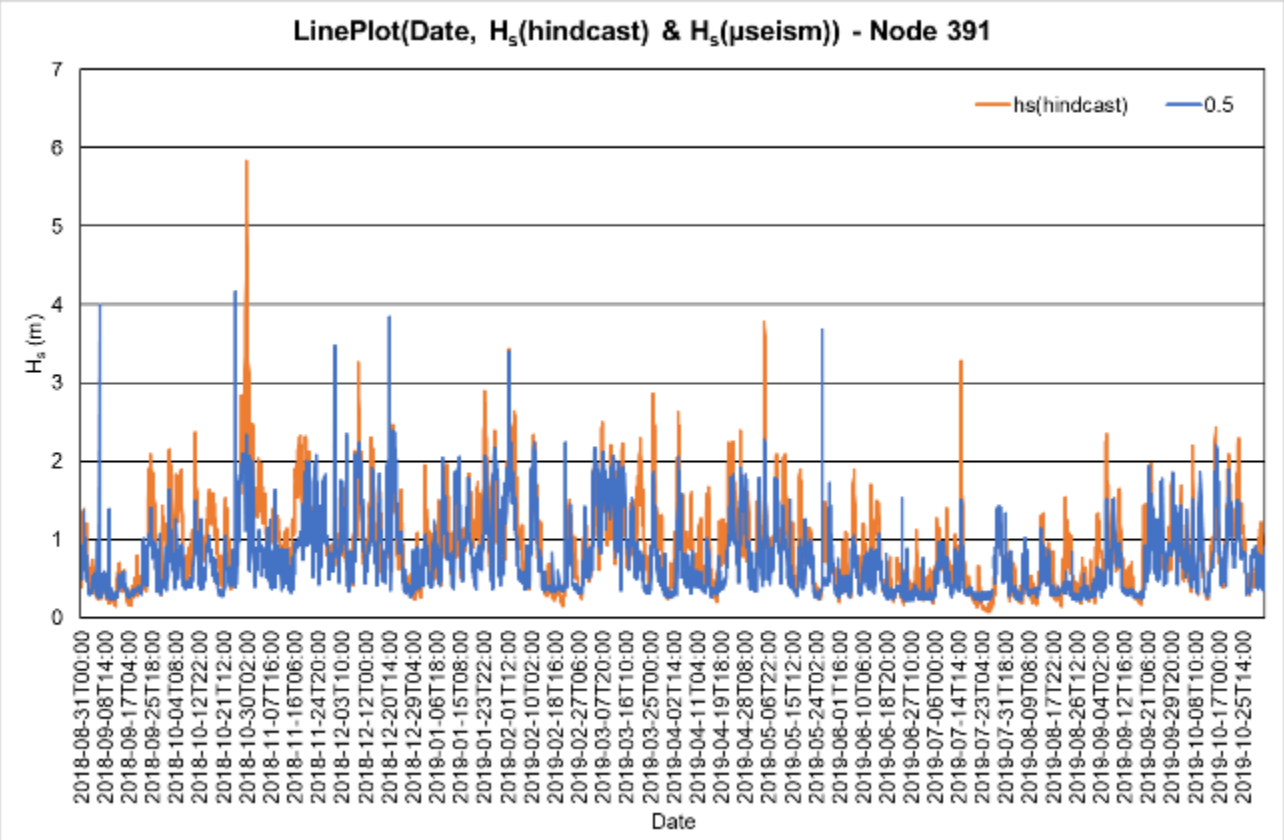

Fig. 8.9. Temporal distribution of H_s(buoy) and H_s(µseism).

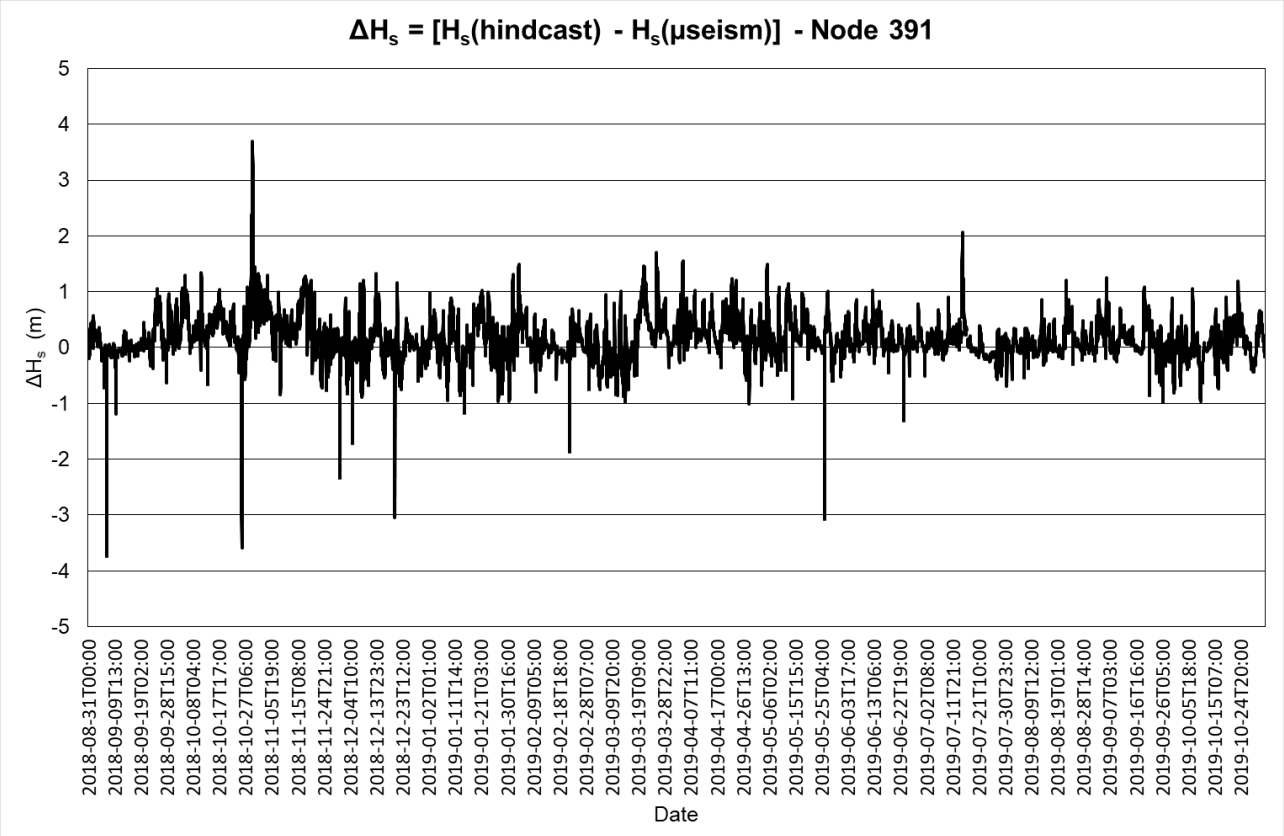

Fig. 8.10. Temporal distribution of ΔH_s between H_s(buoy) and H_s(μseism).

By relating the H_s(hindcast) to the ΔH_s (Fig. 8.11), there is no relationship (R^2=0.3148), but a certain degree of linearity is visible in the distribution of the data.

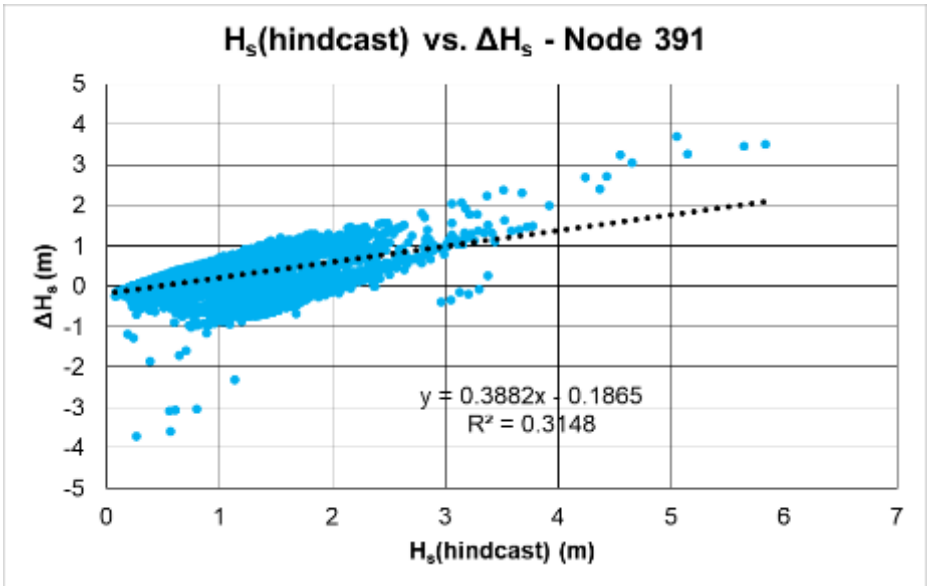

Fig. 8.11. Scatter plot between H_s(hindcast) and ΔH_s.

As a result of this evidence, a modification to the functional is deemed necessary. Some tests for modifying the procedure have been carried out and are reported in the following section.

Phase III: Proposal of amendment to the mathematical procedure

Here, the results obtained by the two tests carried out to correct the H_s estimation procedure on node 319 in the 2013-2014 period are presented. In test 1, the coefficients f_{min} e f_{max} were fixed to 0.2 Hz and 0.9 Hz, respectively. These values were chosen because they determined the frequency range of typical microseism in the Ligurian Sea, as indicated by Ferretti et al. (2013).

Table 8.6 reports the new coefficients calculated fixing f_{min} and f_{max} for all the seismic stations considered in Ferretti et al. (2018). Table 8.7 shows the mean, minimum and maximum values of ΔH_s and ΔH_sAbs derived from the original model, test 1 and test 2. Fig. 8.12-8.14 show the temporal distributions of H_s(hindcast) and H_s(μseism) in the original format, and from test 1 and test 2. Fig. 8.15 report the scatter plots between H_s(hindcast) and ΔH_s for node 319 obtained by the original model, test 1 and test 2.

Table 8.6. New coefficients *a* and *b* of each functional obtained by fixing f_{min} and f_{max}.

Station	Coefficient *a*	Coefficient *b*	f_{min}	f_{max}	Station	Coefficient *a*	Coefficient *b*	f_{min}	f_{max}
GBOS	**1**				**GORR**	**5**			
F_{tot}	0.55	7.73	0.2	0.9	F_{tot}	0.55	7.53	0.2	0.9
$F_{\geq 1.0}$	0.16	2.69	0.2	0.9	$F_{\geq 1.0}$	0.14	2.33	0.2	0.9
$F_{\geq 1.5}$	0.14	2.64	0.2	0.9	$F_{\geq 1.5}$	0.12	2.34	0.2	0.9
$F_{\geq 2.0}$	0.19	3.49	0.2	0.9	$F_{\geq 2.0}$	0.14	2.75	0.2	0.9
$F_{\geq 3.0}$	0.00	0.00	0.2	0.9	$F_{\geq 3.0}$	0.00	0.00	0.2	0.9
IMI	**2**				**MSSA**	**6**			
F_{tot}	0.53	6.66	0.2	0.9	F_{tot}	0.57	8.53	0.2	0.9
$F_{\geq 1.0}$	0.18	2.64	0.2	0.9	$F_{\geq 1.0}$	0.17	2.87	0.2	0.9
$F_{\geq 1.5}$	0.20	3.15	0.2	0.9	$F_{\geq 1.5}$	0.14	2.79	0.2	0.9
$F_{\geq 2.0}$	0.20	3.42	0.2	0.9	$F_{\geq 2.0}$	0.17	3.35	0.2	0.9
$F_{\geq 3.0}$	0.00	0.00	0.2	0.9	$F_{\geq 3.0}$	0.00	0.00	0.2	0.9
QLNO	**3**				**PCP**	**7**			
F_{tot}	0.56	7.18	0.2	0.9	F_{tot}	0.54	7.49	0.2	0.9
$F_{\geq 1.0}$	0.16	2.46	0.2	0.9	$F_{\geq 1.0}$	0.16	2.70	0.2	0.9
$F_{\geq 1.5}$	0.16	2.77	0.2	0.9	$F_{\geq 1.5}$	0.14	2.56	0.2	0.9
$F_{\geq 2.0}$	0.13	2.47	0.2	0.9	$F_{\geq 2.0}$	0.22	3.97	0.2	0.9
$F_{\geq 3.0}$	0.00	0.00	0.2	0.9	$F_{\geq 3.0}$	0.00	0.00	0.2	0.9
RORO	**4**				**PLMA**	**8**			
F_{tot}	0.51	6.47	0.2	0.9	F_{tot}	0.53	7.74	0.2	0.9
$F_{\geq 1.0}$	0.17	2.60	0.2	0.9	$F_{\geq 1.0}$	0.16	2.75	0.2	0.9
$F_{\geq 1.5}$	0.12	2.08	0.2	0.9	$F_{\geq 1.5}$	0.20	3.70	0.2	0.9
$F_{\geq 2.0}$	0.16	2.91	0.2	0.9	$F_{\geq 2.0}$	0.22	4.10	0.2	0.9
$F_{\geq 3.0}$	0.00	0.00	0.2	0.9	$F_{\geq 3.0}$	0.00	0.00	0.2	0.9

Table 8.7. Mean, standard deviation (SD), minimum (Min) and maximum (Max) values of ΔH_s and $\Delta H_s Abs$ derived from the original model, test 1 and test 2.

	ΔH_s(original)	**ΔH_sAbs(original)**	**ΔH_s(test1)**	**ΔH_sAbs(test1)**	**ΔH_s(test2)**	**ΔH_sAbs(test2)**
Mean	-0.02	0.22	-0.10	0.29	-0.34	0.43
SD	0.31	0.22	0.39	0.27	0.47	0.40
Min	-5.48	0.00	-2.27	0.00	-2.40	0.00
Max	1.83	5.48	1.82	2.27	1.67	2.40

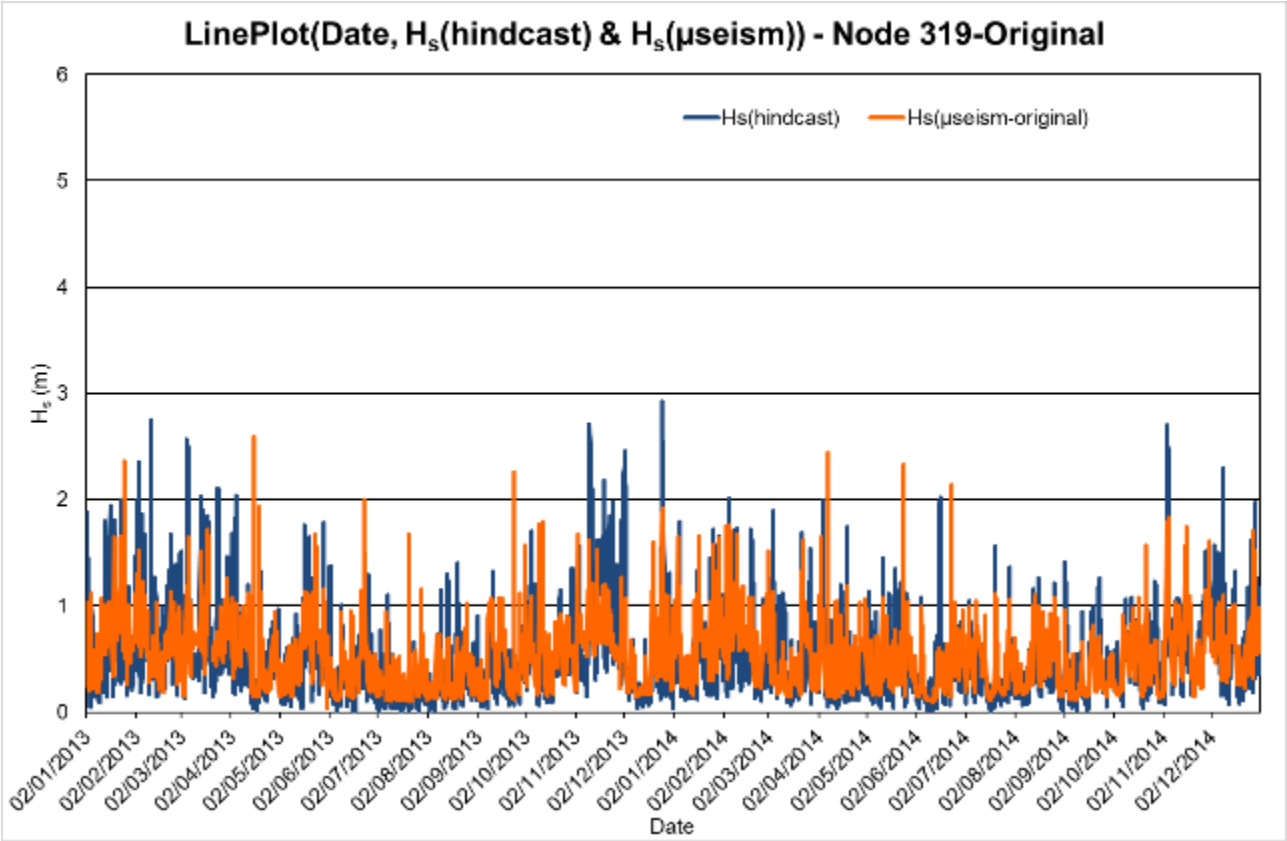

Fig. 8.12. Temporal distribution of H_s(hindcast) and H_s(μseism) in the original format from Ferretti et al. (2018).

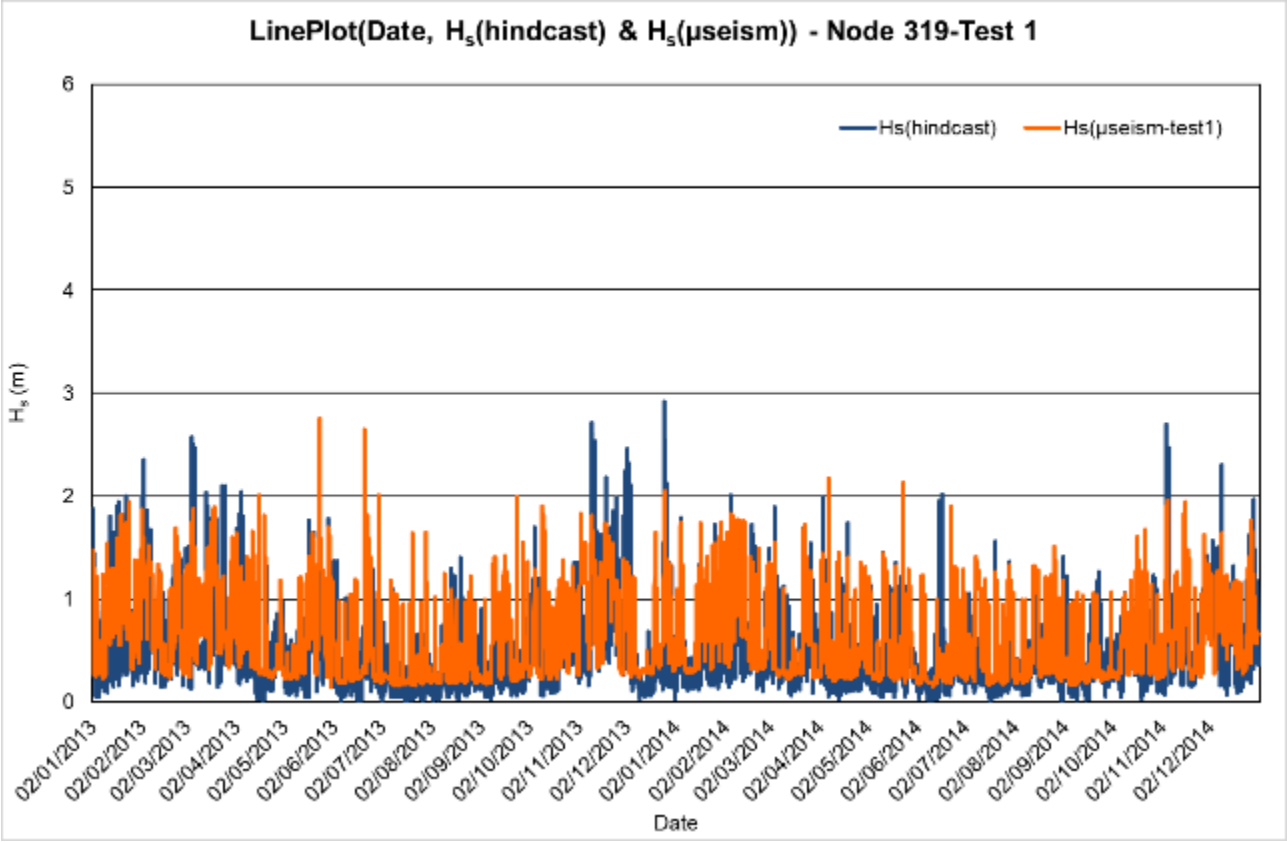

Fig. 8.13. Temporal distribution of H_s(buoy) and H_s(μseism) derived from test 1.

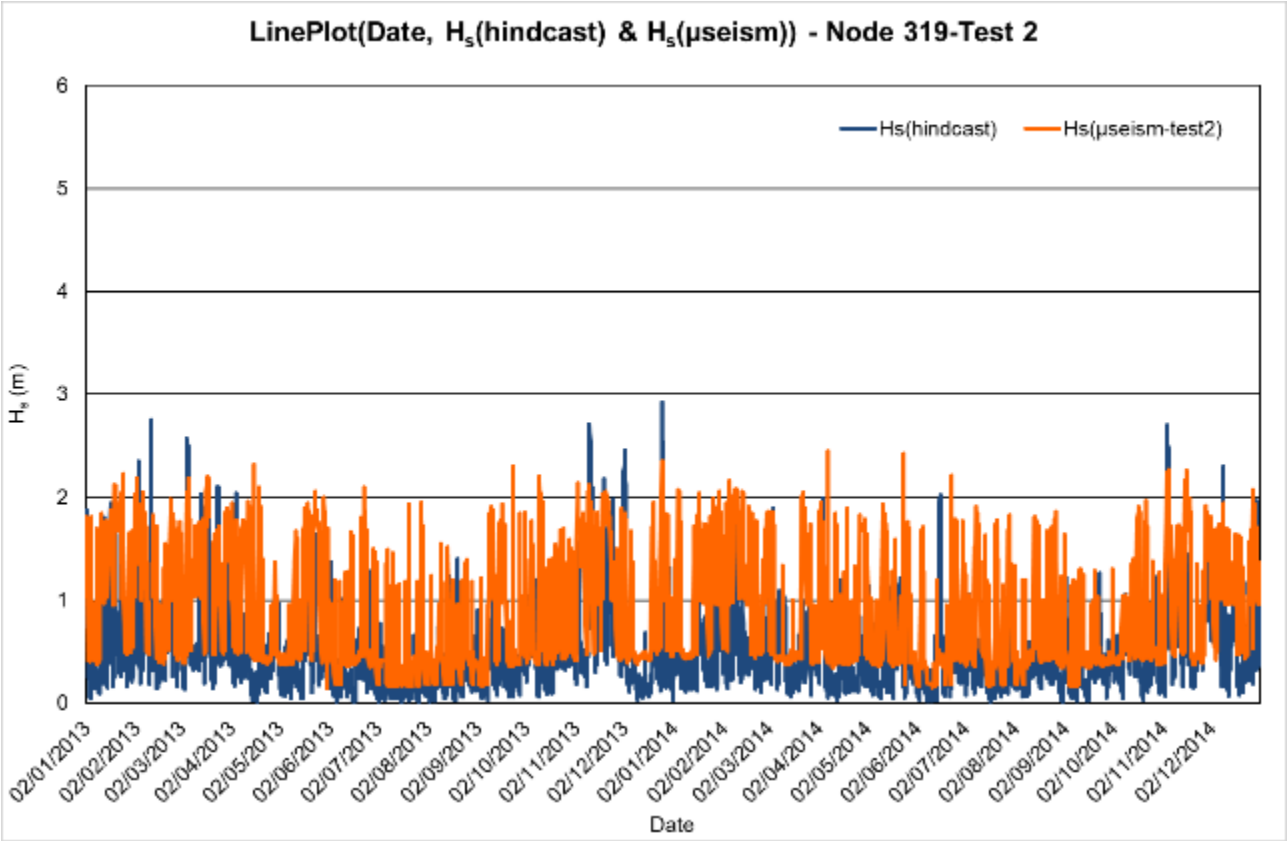

Fig. 8.14. Temporal distribution of H_s(buoy) and H_s(μseism) derived from test 2.

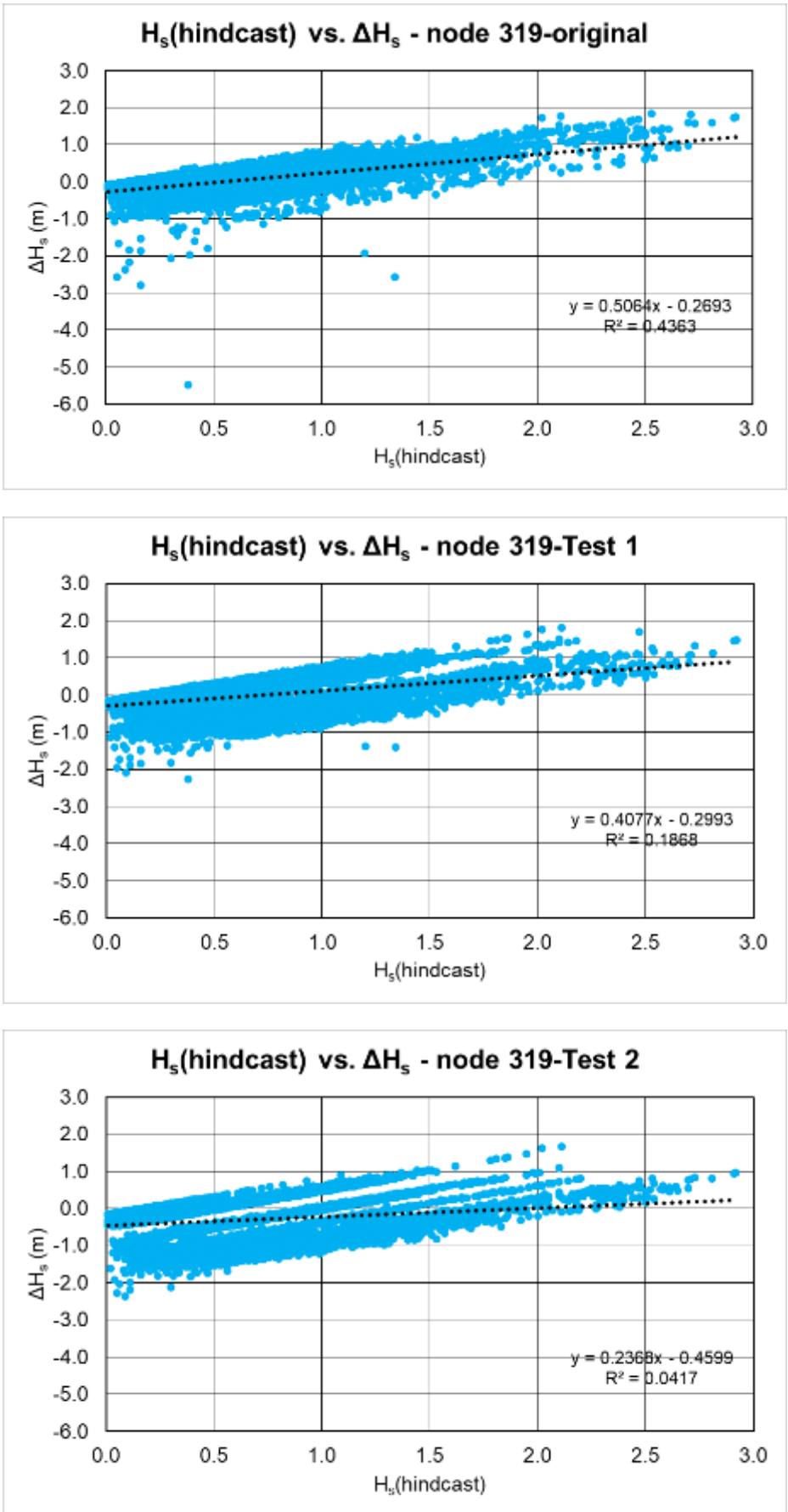

Fig. 8.15. Scatter plots between H_s(hindcast) and ΔH_s for node 319 with the original model (top), with the test-1 model (middle), and with the test-2 model (bottom).

After this, verification of the modified procedure with test 2 was applied at the node 319 on the 2018-2019 period. Fig. 8.16 compares the distributions of H_s(hindcast), H_s(μseism-original) and H_s(μseism-test 2). It is evident that in the case of H_s>1 m the H_s(μseism-test 2) fits better the hindcast data, but there are also two negative evidences: when H_s is very low (<0.5 m), H_s(μseism-test 2) is generally overestimated; moreover, when H_s(hindcast) is between 0.5 and 1, it is very overestimated by test 2. Comparison between ΔH_s in the original format and with test 2 application is summarised in Fig. 8.17.

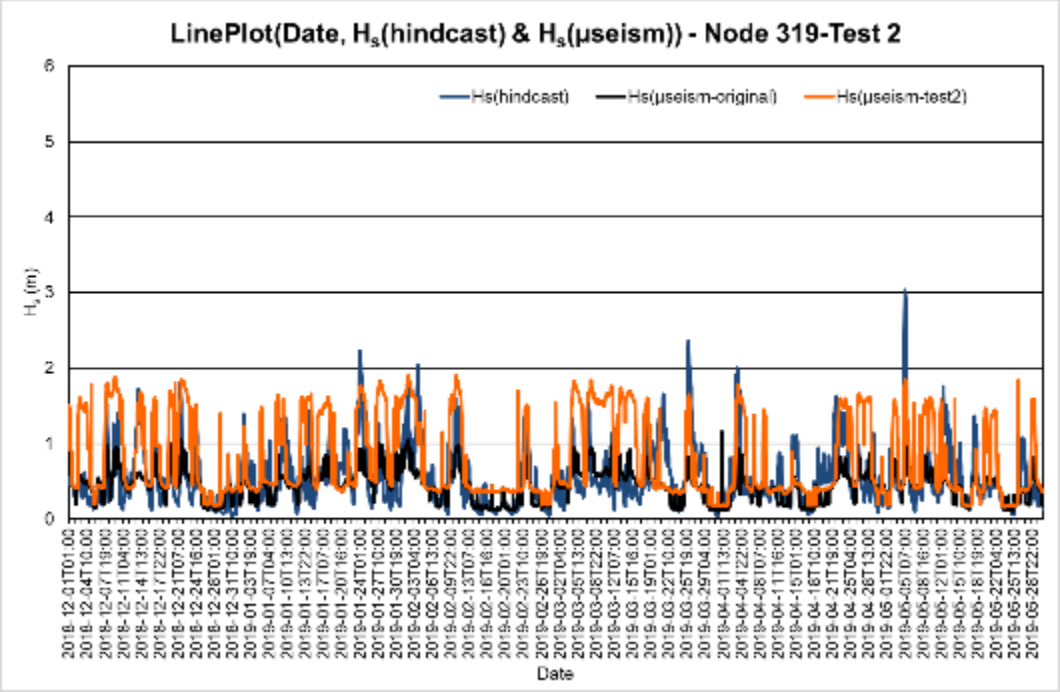

Fig. 8.16. Temporal distribution of H_s(hindcast), H_s(μseism-original) and H_s(μseism-test 2) for node 319 in the 2018-2019 period.

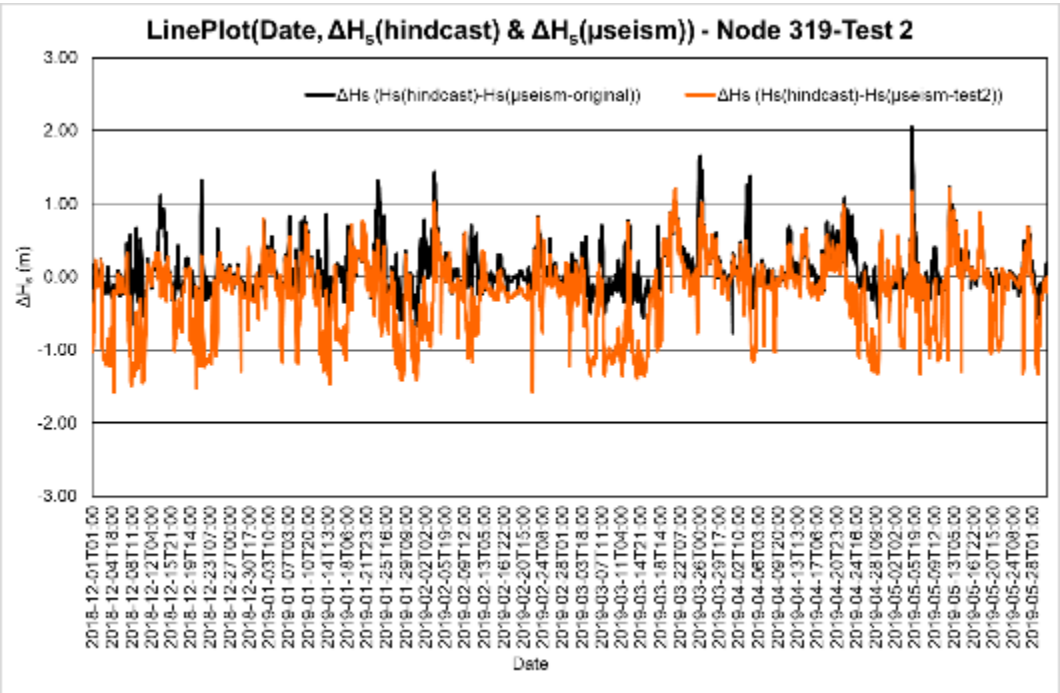

Fig. 8.17. Temporal distribution of ΔH_s between H_s(hindcast) and H_s(μseism) in the original format from Ferretti et al. (2018) and with test 2 for node 319 in the 2018-2019 period.

Similar results are obtained by applying test 2 to node 391 for both 2013-2014 and 2018-2019 periods (Fig. 8.18-8.20).

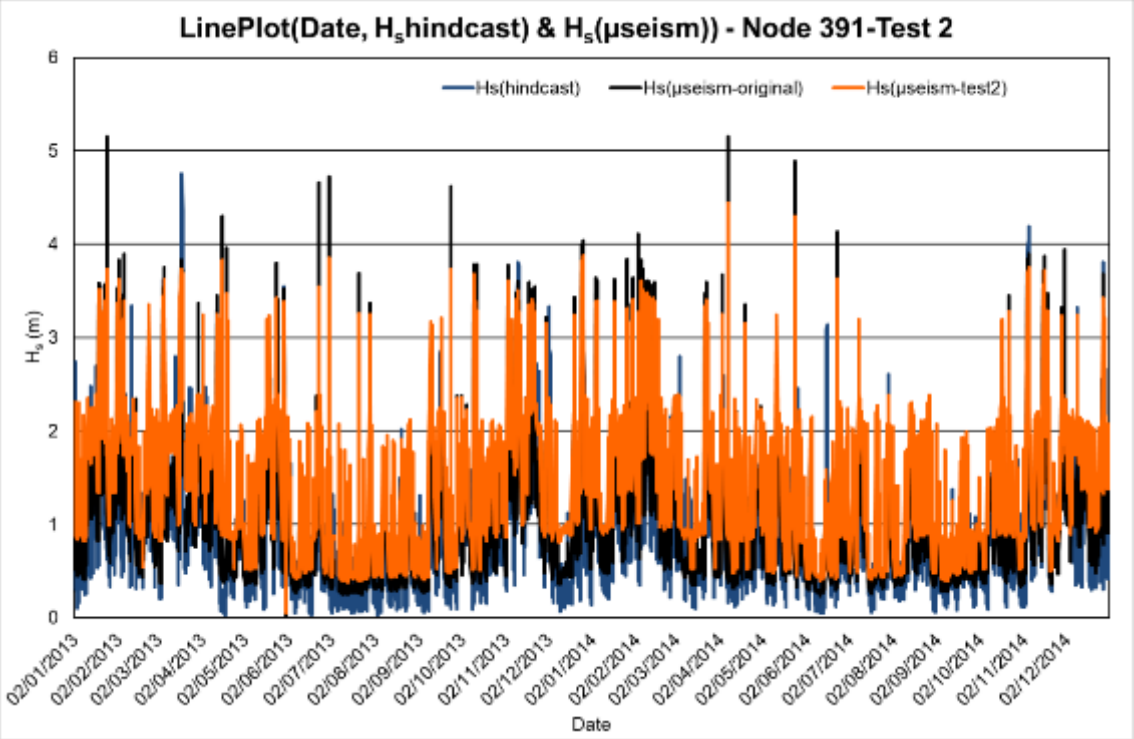

Fig. 8.18. Temporal distribution of H_s(hindcast), H_s(μseism-original) and H_s(μseism-test 2) for node 391 in the 2013-2014 period.

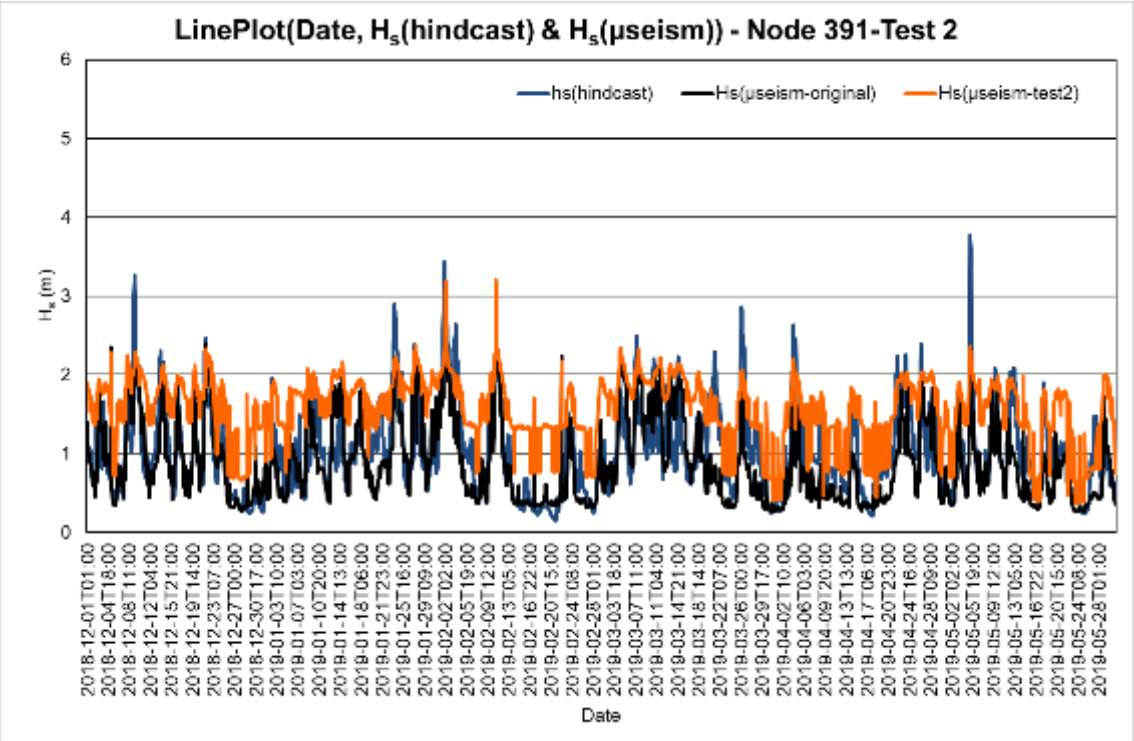

Fig. 8.19. Temporal distribution of H_s(hindcast), H_s(μseism-original) and H_s(μseism-test 2) for node 391 in the 2018-2019 period.

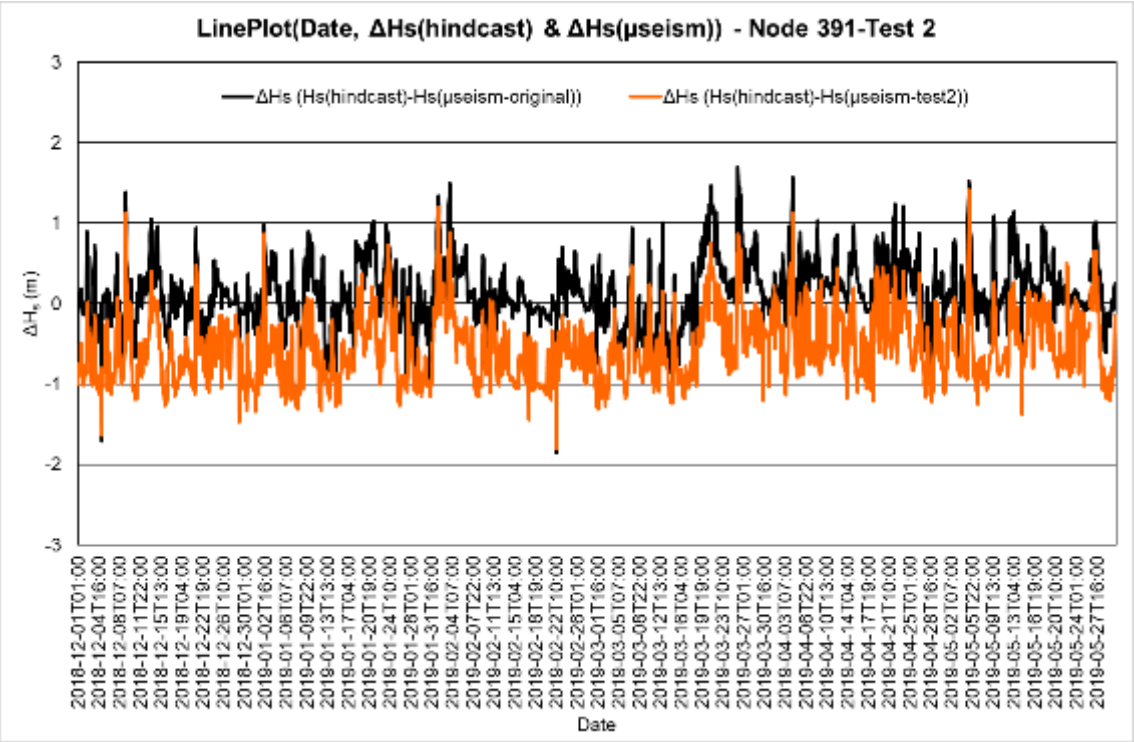

Fig. 8.20. Temporal distribution of ΔH_s between H_s(hindcast) and H_s(μseism) in the original format from Ferretti et al. (2018) and with test 2 for node 391 in the 2018-2019 period.

8.4 Conclusions

The monitoring of the reliability of the H_s data obtained starting from microseisms has allowed to highlight how the original model of Ferretti et al. (2018) tends to underestimate H_s>1 m. Subsequent recalibration tests have been carried out in order to provide an alternative H_s estimatioin by the original model only for H_s>1 m. Thanks to these tests, it was possible to obtain a new way of displaying the estimated H_s, with which, in addition to the curves currently displayed in the Seism4sea webpage (Fig. 6.3), a possible better estimate of H_s>1 m can also be displayed to the end user. Below is an example of the graphical restitution of the new visualisation obtained thanks to the tests.

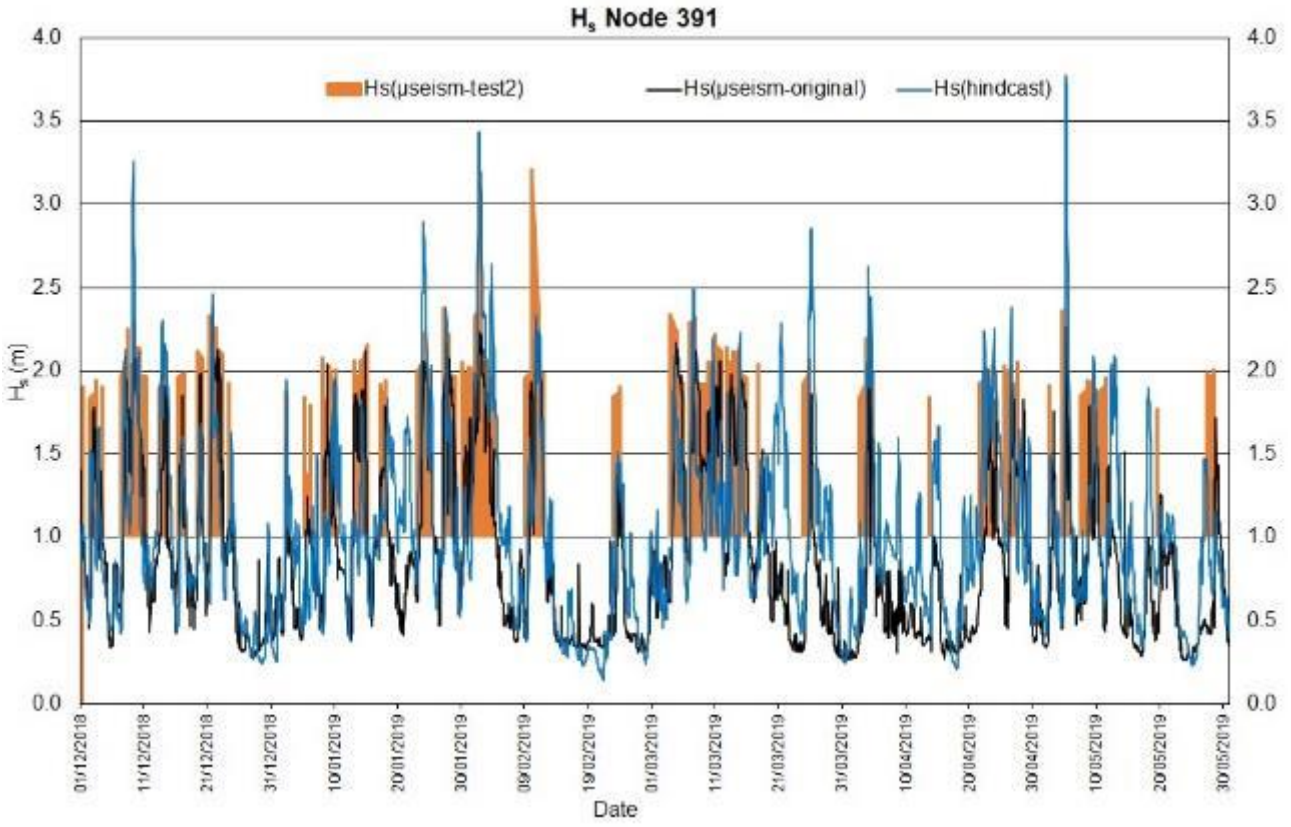

The study for the improvement of the model of Ferretti et al. (2018) (model that for now remains the most reliable one because it generates the best residuals compared to those obtained with the recalibration tests) needs to be further deepened to solve the problem of the underestimation of H_s, using for the recalibration longer datasets that include a larger number of values with H_s>1 m. For this purpose, a suitable database is being collected and therefore, the recalibration phase, depending on the amount of data with H_s>1 that can be collected, will take a long time. For this reason, the research activity will continue beyond the *Ph.D.* and will include studying and monitoring the reliability of the data over the long term.

8.5 References

Ferretti G., Barani S., Scafidi D., Capello M., Cutroneo L., Vagge G., Besio G. (2018). Near real-time monitoring of significant sea wave height through microseism recordings: An application in the Ligurian Sea (Italy). Ocean and Coastal Management 165: 185-194. https://doi.org/10.1016/j.ocecoaman.2018.08.023

Ferretti G., Zunino A., Scafidi D., Barani S., Spallarossa D. (2013). On microseisms recorded near the Ligurian coast (Italy) and their relationship with sea wave height. Geophysical Journal International 194: 524–533. https://doi.org/10.1093/gji/ggt114

9 The SINAPSI Project and future developments

The SINAPSI Project has been financed by the Interreg Italy-France Maritime 2014-2020 Programme (http://interreg-maritime.eu/), started on April 2019, and has a duration of three years. The project aims to improve navigation risk prevention by optimising existing technologies to provide port operators with real-time data on weather and sea conditions. In order to support ships and vessels during port approaches and manoeuvres within port basins, and thus reducing the risks for crews, passengers and shore-based operators, the SINAPSI Project envisages the installation of instruments and systems for real-time or near-real-time

monitoring of weather and sea conditions, such as waves and currents, inside and outside different ports distributed along the coastline of the Maritime Programme area (Fig. 9.1).

Fig. 9.1. In blue, the Maritime Programme area; in red, the port involved in the project.

SINAPSI is the result of an initiative coordinated by two Departments of the University of Genoa (DISTAV and DICCA), with the participation of the following Partners: the Marine Science Institute of the National Research Council, the Université of Toulon, the Port Authority of the North Tyrrhenian Sea, the Laboratory of Environmental Monitoring and Modelling for Sustainable Development Consortium, the European Research Institute Onlus, and the Chamber of Commerce and Industry of Var.

SINAPSI was contemporary with the *Ph.D.* project and had the same duration (3 years). For the realisation of the *Ph.D.* activities carried out in the framework of the SINAPSI project, it was necessary to get acquainted with the Maritime Programme rules and apply good practices of European project management.

The project was structured into four different components: the project management component (M), which deals with both the financial side and the monitoring of the progress of the activities; two project implementation components (T1 “Monitoring” and T2 “Simulation”), which include all the practical activities implemented by the project in order to achieve the set objectives; the communication component (C), which includes all the dissemination actions of the project activities and results to public, agencies, and the scientific community. In addition, a key part of SINAPSI Project is the Investment component (I), which includes the installation of measuring instruments and systems in the project area.

9.1 Project management

Following indications of Kinser (2008) on project management, a basic strategy of project management was chosen. Project management requires planning and organising the activities involved in a project, setting up a realistic project schedule and keeping a continuous control on the progress of activities, managing the risks into which the project may fall and ensuring quality control, and coordinating Partners. Therefore, it was

necessary to set up a strategy (planning) with the different actions (execution) to carry out the project properly. A tool was developed for planning the activities and monitoring the progress of the SINAPSI Project, i.e., a timetable of activities with all the planned products for each project component and their respective delivery deadlines. The schedule was kept up-to-date as the project progressed.

9.2 Project implementation

Within the implementation components, the weather and sea monitoring part of the SINAPSI Project included in its first phase the study and implementation of a monitoring plan. As regards sea wave and current monitoring in the Genoa area, this phase involved the project Partners UNIGE for sea currents and CNR-ISMAR for sea waves, and the project stakeholders. Several meetings between partners and with stakeholders were held, allowing to define the monitoring plan by the identification of the most suitable sites for the installation of the instruments and the type and frequency of data needed by the stakeholders. In the case of the Port of Genoa, the stakeholders involved in the monitoring process design were the Port Authority, Coast Guard, Pilots and vessel captains. The final version of the monitoring plan (product "T1.1.1 - Progettazione monitoraggio") is available on the website of the project, in the page "Che cosa realizza?" (What does it achieve?) dedicated to the dissemination of the products (http://interreg-maritime.eu/documents/1232077/1800432/T1.1.1+Progettazione+monitoraggio/0ad6f85c-bde6-47b2-9060-6fa684176ee1).

9.3 Project dissemination

The main communication tools of the Maritime Programme, which are to be considered, are the corporate image (logos and graphics), the website, newsletters and social networks (Facebook, Twitter, and YouTube). These tools were then prepared and shared with partners at the beginning of the project and managed during the project progress (http://interreg-maritime.eu/web/sinapsi; https://www.facebook.com/SinapsiMarittimo/).

As required by the Maritime Programme, all products in SINAPSI were realised in Italian and French and were complied with specific communication rules imposed by the European Union and the Maritime Programme (Interreg Maritime, 2019, 2020). Moreover, each communication product must be validated by the Managing Authority and all contacts with the Managing Authority must be maintained by a person designated as the project Communication Manager. Therefore, as Communication Manager, all communication products and all the contacts with the Managing Authority were revised and held, respectively, by me.

9.4 Future developments

Given the importance of real-time data on weather and sea conditions for both coastal protection and safe navigation, the study of the relationship between sea waves and microseism in the Ligurian Sea will continue after the end of this *Ph.D* project. In particular, the activity of monitoring and improving the reliability of the data produced by the procedure applied to microseisms will be continued on long term.

In the framework of the SINAPSI Project, that involves the installation of a radar antenna system to monitor the surface waves off the port of Genoa, the data from the radar system will be used in the development of the *Ph.D.* project for intercalibration with microseism data. The aim will be to increase the coverage of the area of the Ligurian Sea monitored by real-time measurements and improve the reliability of the procedure that uses microseism data to provide the significant height of the sea wave.

9.4 References

Kinser J. (2008). The top 10 laws of project management. Paper presented at PMI® Global Congress 2008—North America, Denver, CO. Newtown Square, PA: Project Management Institute.

Interreg Maritime (2019). Manuale di immagine coordinata del Programma Interreg Italia-Francia Marittimo 2014-2020. pp. 38. http://interreg-maritime.eu/documents/197474/1146029/Manuale+Immagine_IT-DEF_Feb2019.pdf/93836774-9516-440d-9a8d-0b3d7666545e

Interreg Maritime (2020). Siti dei progetti - Manuale di utilizzo. pp. 31. http://interreg-maritime.eu/documents/197474/437264/202001_Manuale+siti_versione+2_IT/5eef2ead-7367-4ae1-a4f2-6b25a3909231